

DIPOLE TRAPPING AND MANIPULATION OF ULTRA-COLD ATOMS

Andrian Harsono

A thesis submitted in partial fulfilment of
the requirements for the degree of
Doctor of Philosophy at the University of Oxford



Merton College
University of Oxford
Trinity Term 2006

ABSTRACT

Dipole trapping and manipulation of ultra-cold atoms

Andrian Harsono, Merton College, Oxford University
DPhil Thesis, Trinity Term 2006

A large part of this thesis describes the construction of a new Bose-Einstein Condensation (BEC) experiment starting in October 2003. The magnetic trap setup that was used was a baseball trap accompanied by two pairs of compensation coils (primary and secondary). This setup is capable of producing a magnetic trap of radial trapping frequency of 178.6 Hz and an axial trapping frequency of 5.7 Hz. After an evaporative cooling sequence lasting 85 seconds, we observed phase transition to BEC at 6.5×10^5 atoms at temperature of 320 nK and when the thermal component of our cloud of atoms almost vanished completely, we had 1.5×10^5 atoms at BEC with our thermal component at a temperature of 120 nK.

The objective of all subsequent experiments beyond BEC was to investigate and understand the manipulation of ultra-cold atoms in dipole traps. An Acousto-Optic Deflector (AOD) capable of light diffraction in the X and Y axes was used to manipulate our dipole trap and it has been demonstrated that this experiment could split a dipole trap into two separate traps the separation between which could be varied by varying the frequency of the signal input into the AOD. When atoms in a single dipole trap were first observed, there were about 7000 atoms in the trap and at this moment the experiment is capable of producing this number of atoms in our dipole trap quite reproducibly. Then, the thesis describes a successful basic demonstration of the generation of a simple 2×2 array of 2-dimensional optical lattice. When such an array was first produced, the separation between neighbouring lattice sites was $30 \mu\text{m}$.

In addition, the thesis describes an investigation into the fluorescence imaging setup used to observe the above phenomena. The magnification of such a system was estimated to be 24. A probing sequence was then decided which would produce as much signal as possible from the atoms without heating them by too great an amount. With this probing sequence, an experiment was carried out to gauge how small an atom number this imaging system could detect and this number was around 500 atoms. With further improvements, we hope for the fluorescence imaging system to detect single atoms.

ACKNOWLEDGEMENTS

Building this experiment had not been an easy task, but there are those who worked with me who made the experience somewhat less painful and this section is dedicated to them without whom this thesis would never happen.

I want to thank my supervisor Prof. Christopher Foot for his guidance, support and encouragement along the way. I also want to thank the two post-docs in my life, Simon Cornish and Gerald Hechenblaikner who helped shape me to be the scientist that I am.

My eternal gratitude goes to the people in -111 who helped me set up the experiment as it stands: Martin Shotter, Ben Fletcher, Min Sung Yoon, C M Chandrashekar, James Zacks, Peter Baranowski and Gerald Hechenblaikner. Their contribution towards the experiment had been vital and absolutely priceless. My thanks also to other members of the group who had helped me out in one way or another whenever I was in serious trouble: Rachel Godun, Giuseppe Smirne, Ma Zhao Yuan, William Heathcote, Eileen Nugent, , Benjamin Sheard, Amita Deb and Vincent Boyer.

And what about other members of staff? I want to say a big thank you as well to the technicians I have worked with: Graham Quelch, George Matthews and the champion of them all, Rob Harris. There were also other people outside physics who have helped me overcome the occasional stress and gave me the best years of my life at Oxford, my friends at Merton College and in London and overseas.

Finally, to my parents and brothers for their love and support, who stood by my decision to do physics despite being born in a family of businessmen. My mother may not know this, but I do get homesick even though I rarely call home...

CONTENTS

1	Introduction	1
1.1	Bose-Einstein Condensation	1
1.2	Quantum computation with ions and neutral atoms	1
1.3	Quantum bit register	3
1.4	Experimental proposal	3
1.5	Abbreviations used in thesis	4
2	Theory of BEC and experimental techniques	6
2.1	Experimental aspects of BEC	6
2.1.1	Atomic properties of Rubidium-87	6
2.1.2	The ideal Bose gas	8
2.2	Laser cooling	15
2.2.1	Doppler cooling	16
2.2.2	Sub-Doppler cooling	17
2.3	Magneto-optical traps	21
2.3.1	Six-beam MOT	22
2.3.2	Pyramidal MOT	23
2.4	Magnetic trapping of neutral atoms	23
2.4.1	Zeeman effect on the hyperfine ground states	25
2.4.2	The Ioffe-Pritchard trap	27
2.5	Evaporative cooling	29
2.5.1	Evaporative cooling	30
2.5.2	RF-evaporative cooling	32
2.6	Sub-shot noise measurements of atom number	33
2.6.1	Dipole trapping of neutral atoms	33
2.6.2	The Mott Insulator State	37
3	The Experimental Apparatus	40
3.1	The BEC Apparatus	40

3.1.1	Lasers	40
3.1.2	The optical table	41
3.1.3	Frequency stabilization	45
3.1.4	Vacuum system	49
3.1.5	Pyramidal MOT	50
3.1.6	2nd MOT - experimental MOT	53
3.1.7	Magnetic trap	56
3.1.8	Evaporation	63
3.2	Dipole trap apparatus	63
3.2.1	Lasers	64
3.2.2	Acousto-Optic Deflector	65
3.2.3	CCD Camera	69
3.2.4	Four-lens objective	70
3.3	Diagnostics	72
3.3.1	Recapture method	72
3.3.2	Absorption imaging	73
3.3.3	Image analysis	79
4	Producing BEC	82
4.1	Loading the magnetic trap	82
4.1.1	Pyramidal MOT	84
4.1.2	Experimental MOT	84
4.1.3	Compressed MOT and optical molasses	87
4.1.4	Optical pumping	91
4.2	Magnetic trapping	92
4.2.1	Measurement of trapping frequencies	92
4.2.2	Adiabatic compression and the tight Ioffe trap	94
4.3	Evaporative cooling	96
4.3.1	Evaporation stages	96
4.3.2	Observation of Bose-Einstein Condensation	99
5	Dipole trapping and manipulation of ultra-cold atoms	102
5.1	Characterisation of the fluorescence imaging system	102
5.1.1	Initial dipole trapping	102
5.1.2	Positioning the four-lens objective	107
5.1.3	Some estimates of fluorescence imaging parameters	109
5.1.4	Generation and manipulation of multiple spots	109
5.2	Characterisation of the dipole traps	110
5.2.1	Beam waist measurement	110

5.2.2	Loss rate of atoms in the dipole trap	113
5.2.3	Probing sequence	115
5.2.4	Low atom number detection	117
5.2.5	Generation and manipulation of multiple dipole traps	119
6	Conclusion and future work	123
6.1	Achievements so far	123
6.2	Future work	124
6.2.1	Adiabatic loading of BEC	124
6.2.2	Imaging and single atom detection	125
6.2.3	2D optical lattice and the Mott Insulator state	125
	Appendices	127
A	Rubidium-87 data	127
B	Beam waist measurement	128
C	Calculating atom number from a Magneto-Optical trap	130
D	Signal to noise ratio between absorption and fluorescence imaging	132
E	Control	135

Introduction

1.1 Bose-Einstein Condensation

The first experimental observation of Bose-Einstein Condensation (BEC) in 1995 [1] in bosonic alkali atoms brought new prospects to the field of atomic physics and quantum state engineering. The atoms in a BEC have identical quantum mechanical properties and therefore can be thought of as one ‘super entity’ where the atoms show collective behaviour. A condensate can be imaged without being destroyed because its interaction with laser light is much stronger than that of a single particle and a BEC is a lot less fragile than one might expect. Experimentally observed lifetimes are usually of the order of a few seconds and BECs can be rotated, shaken and moved around without losing their quantum properties. Thus BEC provides the ideal test sample for fundamental quantum physics, quantum state engineering techniques and general investigations of atomic properties [2]. The achievement of BEC and the early studies of their properties led to the Nobel Prize in Physics in 2001 for E. A. Cornell, W. Ketterle and C. E. Wieman.

1.2 Quantum computation with ions and neutral atoms

Quantum computation offers a potential revolution in computation. The vast Hilbert space offered by a quantum computer would enable calculations to be done much more quickly. For example, Shor’s algorithm could factorise numbers that would be too large for classical computers. This would enable breaking of public key encryption protocols, such as those currently used for internet banking transactions. It has now become a real technical challenge to build a system with

extremely good isolation against environmental decoherence and where interactions between quantum bits can be turned on and off on demand.

Enormous progress has been made in atomic, molecular and optical physics in controlling the quantum states of atoms and photons and suppressing decoherence due to unwanted interactions with the environment. Nowadays it is possible to engineer quantum states and also create and manipulate entanglement between atoms as a resource as suggested by quantum information theory. Once control techniques over atoms, photons and ions are mastered, the next milestone would be to bring together these fundamental elements and use them to build more complex systems with applications in quantum information processing.

Two systems that have made large steps towards quantum computation are trapped ions [3] [4] [5] and cold atoms in optical lattices [6] [7] [8]. Experiments with trapped ions have focused on control at the single ion level. These setups are used for the creation of entanglement, precision measurements and small-scale quantum computations and are currently the most promising candidate for quantum computing. On the other hand, experiments with neutral atoms provide us with systems with a large number of subsystems, particles or quantum bits (qubits). In addition, an advantage that neutral atoms have over ions in quantum computation experiments is scalability. Atomic qubits have properties similar to ionic qubits, but whereas the position and state of one ionic qubit can affect all qubits due to the long-range Coulomb interaction, atomic qubits are uncoupled from each other unless in direct contact. At close proximity, the short-range collisional interactions may be used to entangle atomic qubits. Two other types of experiments where quantum gates have been implemented but suffer from potential scalability problems are NMR [9] and within a quantum dot [10].

There is potential for cold atoms in optical lattices to perform quantum gates in a parallel way and cold atoms are also suited for other applications such as quantum simulation of systems in condensed matter physics and the creation of entangled states of many particles. Currently, these experiments typically lack addressability i.e. it is difficult to prepare the basic unit, the atomic qubit, which is defined as a single atom in the ground state of a single well which can be manipulated. What has been demonstrated so far is many atoms in the ground state of many wells [8] with about one atom per well but not individual addressability, and a single atom in a single well, but not in the ground state of this well [11].

A useful review article discussing current progress in quantum information processing with ions and cold atoms can be found in [12].

1.3 Quantum bit register

An integral part of quantum computation is the ability to create a qubit register. A possible physical system that serves this purpose is an array of microtraps for cold atoms in the form of an optical lattice. As first proposed [6] [7], a large number of ultra-cold atoms can be loaded from a BEC into an optical lattice which is nothing more than a standing wave of light that confines the atoms at points of either the maxima or the minima of light intensities. In very strong confinement, the system behaves as a Mott Insulator where it consists of one atom per lattice site. When the internal states of these atoms are used as qubits, they can be entangled in a parallel operation with spin-dependent confinement [13]. This thesis describes work aiming to establish such a register where qubit operations can be carried out and the next section will describe how this particular experiment is different from most other experiments involving optical lattices.

1.4 Experimental proposal

This section describes the proposed experiments in Oxford. The first stage has been to achieve BEC by standard techniques that have been understood, studied and perfected over the years such as magnetic trapping of neutral atoms with a Ioffe-Pritchard trap, laser-cooling with a Magneto-Optical Trap (MOT), evaporative cooling and absorption imaging.

The next stage is dipole trapping. We have loaded atoms from our cloud of ultra-cold atoms into a red-detuned dipole trap and we wish to manipulate the atoms in the dipole trap with the help of an acousto-optic deflector (AOD). Sending multiple frequency inputs into the AOD generates multiple laser beam spots and therefore multiple dipole traps. These traps can be manipulated and moved independently and in real-time to provide the addressability of the atoms missing in other ultra-cold matter experiments with optical lattices. We have also built a fluorescence imaging setup with a diffraction limited objective lens that should be capable of single-atom detection although this has not yet been demonstrated. A large step forward would then be to establish a number-squeezed state of the atom cloud that we have. This is achieved by suppressing the tunnelling of atoms between lattice sites either by raising the potential barrier between the sites [8] or by moving the sites further apart.

This highly-entangled system would provide the foundation for qubit operations. Initially, the experiment must be capable of the deterministic preparation of atomic qubits. This means preparing a single atom on demand in the lowest energy state

of an energy well. If we could control the number of atoms in the mini-lattice of laser beam spots, we could also control the average occupancy of each well. To evenly distribute the atom number over the lattice we could enter the Mott regime by adiabatically increasing the distance between each well, and this should produce a lattice with the majority of the sites having one atom per well. In the near future, we may try encoding single qubits, for example with schemes involving hyperfine levels or in the spatially delocalised qubit scheme [14] which involves bringing wells together, and apart, adiabatically and reproducibly. Also, we could try 2 qubit operations, the simplest of which would be cold controlled collisions between two atoms [7].

1.5 Abbreviations used in thesis

Many abbreviations will be used throughout the thesis. The first time these are used, they will be accompanied by their full name. However, for completeness sake Table 1.1 lists all the abbreviations that will be used.

3D	- Three-dimensional
AOD	- Acousto-optic deflector
AOM	- Acousto-optic modulator
AWG	- Arbitrary Waveform Generator
BEC	- Bose-Einstein Condensation
CCD	- Charged-coupled device
CMOT	- Compressed magneto-optical trap
ECDL	- External cavity diode laser
FET	- Field-effect transistor
GPIB	- General purpose interface bus
IP	- Ioffe-Pritchard
MOSFET	- Metal-Oxide Semiconductor Field-Effect Transistor
MOT	- Magneto-optical trap
NEG	- non-evaporable getter
OD	- Optical depth
OP	- Optical pumping
PCI	- Peripheral component interconnect
PSD	- Phase-space density
PZT	- Piezo-electric transducer
RF	- Radio frequency
TOF	- Time of flight

Table 1.1: Abbreviations used in thesis

Theory of BEC and experimental techniques

This chapter describes the principles behind the experiment and is divided into two sections. The first section deals with the pathway to BEC including a description of the alkali metal we used for this experiment, its atomic properties and how they were exploited for trapping and cooling. The section then proceeds to describe the process in which Bose-Einstein Condensation is achieved. The second section mainly talks about the theory behind sub-shot noise measurements which form the planned experiments beyond BEC.

2.1 Experimental aspects of BEC

2.1.1 Atomic properties of Rubidium-87

Alkali metals

One of the chief reasons why alkali metals are popularly used in laser cooling experiments is that they contain closed cycling transitions. These cycling transitions are beneficial because laser cooling processes require the atom to scatter many photons. The laser frequencies associated with the cooling transitions in or very close to the visible region of the electromagnetic spectrum are also very easy to generate nowadays. In addition, it is experimentally straightforward to produce a vapour or an atomic beam of these alkali metals.

The alkali metals have a simple electronic configuration: a closed shell and a valence electron. For example, the electronic configuration of the element that we are using, rubidium-87, is [Kr]5s. As a result, the total orbital angular momentum L and total intrinsic spin angular momentum S arise purely from this valence electron. The total angular momentum quantum number J is given by

$$|L - S| \leq J \leq L + S \quad (2.1)$$

The first excited level (P) for rubidium is split into $5P_{\frac{1}{2}}$ and $5P_{\frac{3}{2}}$. The difference in energy between the two is given by the spin-orbit interaction $V_{SO} = \beta \vec{L} \cdot \vec{S}$. This interaction is the origin of the fine structure of the atom.

Hyperfine structure arises from the interaction between the nuclear magnetic moment which is proportional to its spin \vec{I} and the internal magnetic field arising from the electrons which is proportional to the total electronic angular momentum \vec{J} . The magnetic-dipole hyperfine interaction has the form $A \vec{I} \cdot \vec{J}$ [15] and the appropriate eigenstates are those of the total angular momentum of the atom \vec{F} given by $\vec{F} = \vec{I} + \vec{J}$. The hyperfine interaction leads to a separation into the F levels. The Zeeman sublevels that make up the F levels are degenerate but the application of an external magnetic field lifts this degeneracy splitting each F level further into m_F states. Each F level splits into $(2F + 1)$ Zeeman sublevels.

Cooling transitions

The allowed electric dipole transitions from the ground state of rubidium are shown in Figure 2.1. Laser cooling and detection is carried out using the transition from the $5S_{1/2}, F = 2$ ground state to the $5P_{3/2}, F = 3$ excited level which is a component of the D2 line at wavelength $\lambda = 780$ nm. In the laser cooling process, the light excites the atoms to the upper $F = 3$ level, but there is a finite probability of non-resonant excitation to the upper $F = 2$ level from which they may decay to the $F = 1$ level in the ground configuration. Atoms in this lower hyperfine level no longer participate in the cooling cycle. To bring them back to the cooling cycle, additional laser light is required which drives the transition from the $5S_{1/2}, F = 1$

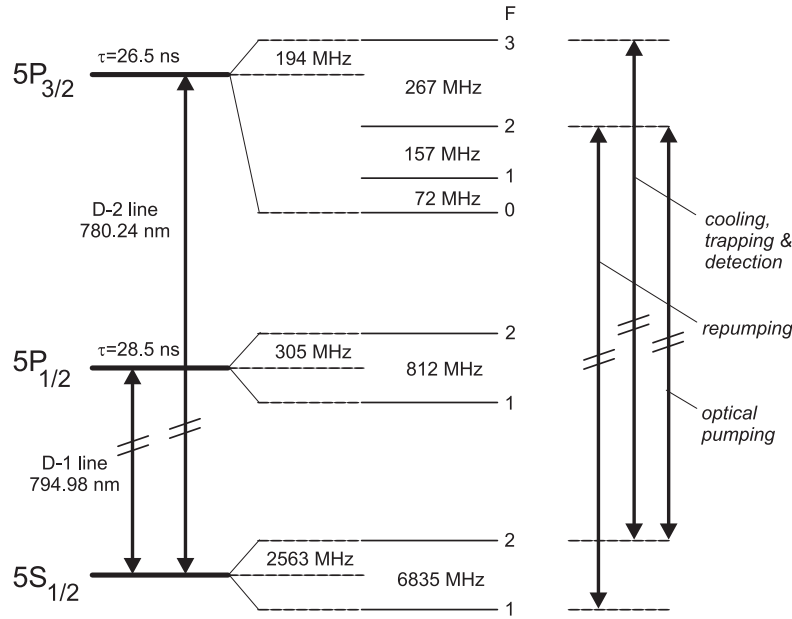


Figure 2.1: The hyperfine structure in the ground and first excited state configurations of Rb-87. Also shown are transitions used for laser cooling, repumping, optical pumping and detection. Data taken from [16].

level to the $5P_{3/2}$ $F = 2$ level. This is called the repumping light. The saturation intensity for the cooling transition is 1.67 mW/cm^2 . For detection of atoms in the $F = 1$ ground state, the atoms are firstly exposed to repumping light to bring them to the $F = 2$ level of the ground state before cooling light on resonance with the $5S_{1/2}, F = 2 \rightarrow 5P_{3/2}, F = 3$ is applied for probing.

2.1.2 The ideal Bose gas

Bose distribution function and Bose-Einstein Condensation

This section gives an overview of the theory which describes trapped Bose gases. More details can be found in [17] and [18]. We begin by considering atoms trapped in an external potential $U(\mathbf{r})$ and occupying single-particle states of the trap with the eigenenergies ϵ_k . At high temperatures where quantum effects have negligible influence, the Bose-distribution of mean occupation number reduces to a Boltzmann distribution

$$\langle n_k \rangle = \frac{1}{e^{(\epsilon_k - \mu)/k_B T} - 1} \approx e^{-(\epsilon_k - \mu)/k_B T} \quad (2.2)$$

For a given temperature, the chemical potential μ is fixed by the condition for conservation of the total number of atoms

$$N = \sum_k \langle n_k \rangle \quad (2.3)$$

At high temperatures, μ is large and negative. As the gas temperature falls, μ approaches the ground state energy ϵ_0 from the negative side until a critical temperature T_c where $\mu = \epsilon_0$. At this critical temperature T_c , the occupation number of the ground state N_0 becomes a macroscopic fraction of the total number of atoms in the system N and as $T \rightarrow 0$, all atoms will end up in the ground level and this phenomenon is called Bose-Einstein Condensation (BEC). In typical BEC experiments, the number of atoms is large and the temperature of the initially non-Bose condensed gas is much larger than the energy spacing ($k_B T \gg \hbar\omega$). The total number of atoms in the excited states is then given as

$$N - N_0 = \int_0^\infty d\epsilon \rho(\epsilon) \frac{1}{e^{(\epsilon_k - \mu)/k_B T} - 1} \quad (2.4)$$

where N_0 is the number of atoms in the ground state and $\rho(\epsilon)$ is the density of states for a gas trapped in some external potential $U(r)$ which is given by

$$\rho(\epsilon) = \frac{2\pi(2m)^{\frac{3}{2}}}{(2\pi\hbar)^3} \int_{U < \epsilon} dr \sqrt{\epsilon - U(r)} \quad (2.5)$$

From equation 2.3, we can assume the ground state energy $\epsilon_0 = 0$ when we change the summation sign to an integral sign. From the above the density distribution $n(r)$ of the cloud can be found using the normalisation condition $N = \int dr n(r)$ and equations 2.4 and 2.5 as

$$n(r) = \frac{1}{\Lambda_T^{\frac{3}{2}}} g_{\frac{3}{2}}(\tilde{z} e^{-U(r)/k_B T}) \quad (2.6)$$

where the fugacity is $\tilde{z} = e^{\mu/k_B T}$ and the poly-logarithm function is $g_\alpha(x) = \sum_{k=1}^\infty \frac{x^k}{k^\alpha}$. The thermal de Broglie wavelength is given as

$$\Lambda_T = \sqrt{\frac{2\pi\hbar^2}{mk_B T}} \quad (2.7)$$

Regardless of the trap geometry, phase transition for BEC occurs when at the centre of the trap, the degeneracy parameter $n(0)\Lambda_T^3$ reaches a critical value ($\mu = 0$)

$$n(0)\Lambda_T^3 = g_{\frac{3}{2}}(1) = 2.612\dots \quad (2.8)$$

Note that $g_n(1) = \zeta(n)$ where $\zeta(n)$ is Riemann's ζ -function. Equation 2.8 illustrates the fundamental feature that at phase transition to BEC, the thermal de Broglie wavelength is comparable to the separation between the atoms. For a harmonic potential as in the case for most BEC experiments, the density of states is given as

$$\rho_{ho}(\epsilon) = \frac{1}{2} \frac{\epsilon^2}{\hbar\bar{\omega}} \quad (2.9)$$

where the geometric mean of the trap frequency $\bar{\omega}$ is given as

$$\bar{\omega} = (\omega_x\omega_y\omega_z)^{\frac{1}{3}} \quad (2.10)$$

The number of atoms in the excited state is determined by substituting 2.9 into 2.4 which gives

$$N - N_0 = g_3(1) \left(\frac{k_B T}{\hbar\bar{\omega}} \right)^3 \quad (2.11)$$

At the phase transition $N_0 = 0$ and hence the critical temperature is given by

$$T_c = \frac{\hbar\bar{\omega}}{k_B} \left(\frac{N}{g_3(1)} \right)^{\frac{1}{3}} \approx 0.94 \frac{\hbar\bar{\omega}}{k_B} N^{\frac{1}{3}} \quad (2.12)$$

The trapped gas in the classical regime

In the classical regime where the chemical potential $\mu < 0$ and $|\mu| \gg k_B T$, the fugacity $\tilde{z} \ll 1$ and using equation 2.5, we find that the density at the centre of the trap is given as

$$n(0) = \frac{1}{\Lambda_T^3} g_{\frac{3}{2}}(\tilde{z}) \approx \frac{1}{\Lambda_T^3} \tilde{z} \quad (2.13)$$

In this case the thermal de Broglie wavelength would be much smaller than the separation between the atoms. So from equations 2.4, 2.5 and 2.6, we see that the number of atoms N can be written as

$$N = n(0)\Lambda_T^3 Z_1 \quad (2.14)$$

where the classical canonical partition function for a single atom is given as

$$Z_1 = \frac{1}{(2\pi\hbar)^3} \int \int_{-\infty}^{\infty} dp dr e^{-(U(r)+p^2/2m)/k_B T} \quad (2.15)$$

If we define the reference volume of the gas as $V_e = N/n(0)$, we find that

$$V_e = \Lambda_T^3 Z_1 \quad (2.16)$$

and that the degeneracy parameter is given as

$$n(0)\Lambda_T^3 = \frac{N}{Z_1} \quad (2.17)$$

In most cases, magnetic trapping potentials fall under the class of power-law potentials which are in the form of $U(x, y, z) \propto |x|^{\frac{1}{\delta_1}} + |y|^{\frac{1}{\delta_2}} + |z|^{\frac{1}{\delta_3}}$ with $\delta = \sum_i \delta_i$ [17]. $\delta_1 = \delta_2 = \delta_3$ gives $\delta = \frac{3}{2}$ corresponding to an harmonic trap and $\delta = \frac{5}{2}$ corresponds to a spherical-quadrupole geometry. For power-law potentials a simple form of the single atom partition function can be derived as

$$Z_1^\delta = A_{PL}^\delta (k_B T)^{\delta + \frac{3}{2}} \Gamma\left(\frac{3}{2} + \delta\right) \quad (2.18)$$

where A_{PL}^δ is a constant depending on the strength of the potential. $\Gamma(x) = \int_0^\infty dt t^{(x-1)} e^{-t}$ is the Euler gamma function. In the general Ioffe-Pritchard trap case where the potential is approximate harmonic near the trap bottom but linear higher up, the single atom partition function needs to be expressed as the sum of two power-law contributions [19] [20] [21]

$$\begin{aligned}
Z_1^{IQ} &= Z_1^{\delta=\frac{3}{2}} + Z_1^{\delta=\frac{5}{2}} \\
&= 6A_{IQ}(k_B T)^4 \left(1 + \frac{2U_0}{3k_B T}\right)
\end{aligned} \tag{2.19}$$

where $U_0 = m_F g_F \mu_B B_0$, and the trap-dependent constant A_{IQ} is given by

$$A_{IQ} = \frac{(2\pi^2 m)^{\frac{3}{2}}}{(2\pi\hbar)^3 2(m_F g_F \mu_B \alpha)^2 \sqrt{m_F g_F \mu_B \beta / 2}} \tag{2.20}$$

Here α and β are parameters describing the strength of the above-mentioned Ioffe-Pritchard trap such that the expression describes the potential energy felt by neutral atoms in such a trap is given by

$$U(r) = \sqrt{\alpha^2(x^2 + y^2)^2 + (U_0 + \beta z^2)^2} \tag{2.21}$$

For a harmonic trap in the classical regime it follows from equations 2.5 and 2.17 - 2.20 that the density distribution takes on a Gaussian form

$$n(r) = \frac{N}{\pi^{\frac{3}{2}} \prod_i r_{0,i}} e^{-\sum_i \left(\frac{r_i}{r_{0,i}}\right)^2} \tag{2.22}$$

with the $1/e$ radius of the cloud in the i -direction given as

$$r_{0,i} = \frac{1}{\omega_i} \sqrt{\frac{2k_B T}{m}} \tag{2.23}$$

This is inversely proportional to the trapping frequency ω_i .

The weakly interacting Bose gas

In ultra-cold and dilute alkali gases, elastic interactions between atoms play a very large role. The density distribution $n_c(r)$ of a condensate deviates from the Gaussian form because of these interactions. At low energies elastic collisions occur in the s-wave scattering limit and this scattering can be described by the use of the pseudo potential [18]

$$V(r - r') = \frac{4\pi\hbar^2 a}{m} \delta(r - r') \tag{2.24}$$

In the case of rubidium this interaction is repulsive and the positive value of the triplet scattering length is $a = (106 \pm 4) \times a_0 = 57.7 \times 10^{-10}$ m [22] [23] with Bohr's radius $a_0 = 0.529 \times 10^{-10}$ m. The use of the s-wave approximation is acceptable as long as $|R_0/\Lambda_T| \ll 1$ where $R_0 = (C_6 m / (2\hbar^2))^{1/4}$ is the effective range of the potential. For rubidium-87, the van der Waals coefficient is $C_6 = 4.3 \times 10^{-76}$ Jm⁶ [22]. This gives $R_0 = 73 \times 10^{-10}$ m and so s-wave scattering can be assumed for temperatures lower than 1 mK. At temperatures around 400 μ K the elastic collisional cross-section of rubidium-87 is enhanced by the presence of d-wave scattering [24]. At densities of 10^{15} cm⁻³, the gas parameter is small $na^3 \ll 1$ and only binary elastic collisions need to be considered. If correlations between atoms manifest themselves only over a short range (much smaller than the size of the gas cloud), the gas can be described in terms of a mean field theory [25]. At $T < T_c$, the macroscopic wave function $\phi(r)$ of the condensate component of the trapped gas in equilibrium obeys the time-independent Gross-Pitaevskii Equation (GPE)

$$\left\{ -\frac{\hbar^2 \nabla^2}{2m} + U(r) + g|\phi(r)|^2 \right\} \phi(r) = \mu \phi(r) \quad (2.25)$$

where $g = \frac{4\pi\hbar^2 a}{m}$ is the interaction parameter. The density of the condensate is $n_c(r) = |\phi(r)|^2$ and we consider repulsive interaction ($a > 0$). At high densities, the mean field interaction $gn_c(r)$ dominates the kinetic energy term which is of the order of $\hbar\omega_r$ so that the kinetic term in the GPE can be ignored; this is known as the Thomas-Fermi approximation. The GPE is then easy to solve:

$$n_c(r) = \frac{1}{g} [\mu - U(r)] \quad (2.26)$$

The condensate density $n_c(r)$ is dependent on the balance between the external potential and the repulsive mean field interaction. In the case of a trapped gas in a harmonic potential with trapping frequencies ω_i , the condensate density profile takes on the form of an inverse parabola. From equation 2.26 we can see that the density vanishes when the external potential exceeds the chemical potential. This condition determines the Thomas-fermi radius R_i given as

$$R_i = \frac{1}{\omega_i} \sqrt{\frac{2\mu}{m}} \quad (2.27)$$

Integration over the density distribution of the condensate component gives the number of condensed atoms as

$$N_0 = \int dr n_c(r) = \left(\frac{2\mu}{\hbar\bar{\omega}}\right)^{\frac{5}{2}} \frac{a_{ho}}{15a} \quad (2.28)$$

where $a_{ho} = \sqrt{\hbar/m\bar{\omega}}$ is the harmonic oscillator length.

Adiabatic compression

Thermodynamic properties of the gas can be evaluated from statistical properties. The relation between the canonical partition function Z , the single particle partition function Z_1 and the free energy $F = E - TS$

$$Z = \frac{Z_1^N}{N!} = e^{-F/k_B T} \quad (2.29)$$

The internal energy E is then given as

$$E = Nk_B T \left(\frac{3}{2} + \gamma\right) \quad (2.30)$$

where

$$\gamma = \frac{T}{V_e} \frac{\partial V_e}{\partial T} \quad (2.31)$$

The first term in equation 2.30 represents the kinetic energy and the second term which is proportional to γ describes the contribution of the potential energy. Starting from equations 2.29, 2.17 and 2.30 and also using Stirling's formula $\ln(N!) \approx N \ln(N) - N$ we find that the degeneracy parameter can also be written as [20]

$$n(0)\Lambda_T^3 = e^{\frac{5}{2} + \gamma + \frac{S}{Nk_B}} \quad (2.32)$$

For power-law traps in the classical regime $\gamma = \delta$ holds true. For a Ioffe trap γ can be found by evaluating equations 2.15, 2.16 and 2.19 to give

$$\gamma_{IQ} = \frac{\frac{3}{2} + \frac{T}{T_0} \frac{5}{2}}{1 + \frac{T}{T_0}} \quad (2.33)$$

where $T_0 = U_0/3k_B$. During an adiabatic change of the trapping potential where the entropy S and the atom number N are conserved, temperature and density change. The degeneracy parameter stays constant unless γ is varied by changing the trap geometry. The reversible change of the degeneracy parameter by changing the potential shape was first experimentally demonstrated for magnetically trapped hydrogen [20]. Adiabatic compression of a gas in a Ioffe trap will result in a change of the temperature as well as the degeneracy parameter of the gas. From equation 2.32 it follows that for the compression from some initial (index i) to final (index f) trapping parameters, the initial and final degeneracy parameters follow the relation

$$\frac{n_f(0)\Lambda_{T,f}^3}{n_i(0)\Lambda_{T,i}^3} = \frac{e^{\gamma_f^{IQ}}}{e^{\gamma_i^{IQ}}} \quad (2.34)$$

The final temperature and density would have to be obtained by solving equation 2.34 numerically. For the simpler case of adiabatic compression of a gas in a harmonic trap, we obtain the simple relation

$$T_f = T_i \frac{\bar{\omega}_f}{\bar{\omega}_i} \quad (2.35)$$

As long as the compression is adiabatic, equations 2.34 and 2.35 will always hold true. During the compression of a gas in a harmonic trap, the density of states remains unchanged, giving the adiabaticity condition

$$\frac{d\omega}{dt} \ll \omega^2 \quad (2.36)$$

A more detailed discussion of the adiabaticity condition can be found in [26].

2.2 Laser cooling

Laser cooling was first proposed in 1975 [27], but not experimentally realised until 1985 [28]. The first neutral atom element to be cooled and trapped using laser

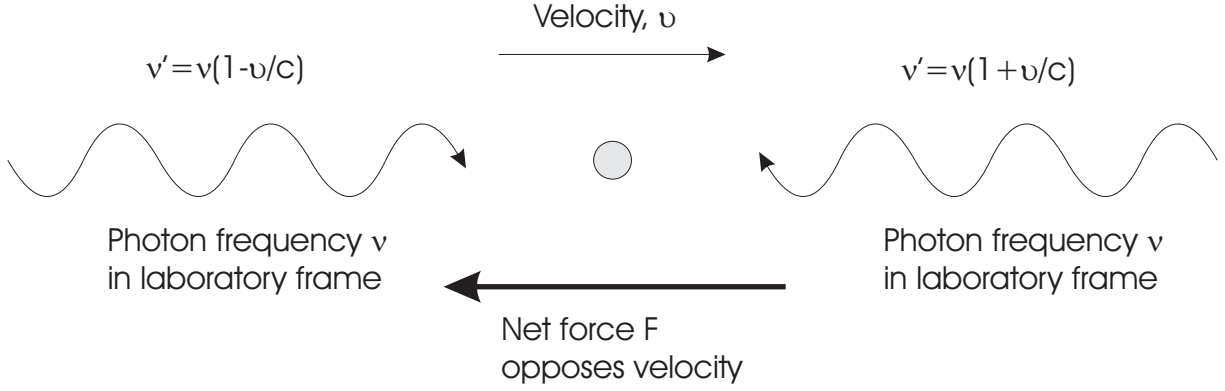


Figure 2.2: An illustration of the principles of Doppler cooling.

radiation was sodium, but the other alkali metal atoms soon followed. In 1997, Steven Chu, Claude Cohen-Tannoudji, and William D. Phillips were awarded The Nobel Prize in Physics ‘for the development of methods to cool and trap atoms with laser light’. Laser cooling was a major discovery in the 20th century and was the last piece in the jigsaw of the quest to create a Bose-Einstein Condensate.

2.2.1 Doppler cooling

Photons have energy $E = \hbar\omega$ and momentum vector $\vec{p} = \hbar\vec{k}$. The absorption of a photon puts the atom into an excited state with a recoil from the light source with momentum $-\hbar\vec{k}$. The absorption is directional but the spontaneous emission is purely isotropic and therefore contributes no net momentum on the atom. The scattering force involves absorption and afterwards spontaneous emission and this scattering force F is dependent upon the scattering rate and the recoil momentum: $F = R\hbar\vec{k}$ where scattering rate R is given as

$$R = \frac{\Gamma}{2} \frac{\frac{I}{I_s}}{1 + \frac{I}{I_s} + \left(\frac{2(\delta - \vec{k} \cdot \vec{v})}{\Gamma}\right)^2} \quad (2.37)$$

where Γ is the natural width of the transition, δ is the laser detuning from the resonance ($\omega_0 - \omega_L$), and $-\vec{k} \cdot \vec{v}$ is the Doppler shift as seen by the moving atoms. $\frac{I}{I_s} = \frac{2\Omega^2}{\Gamma^2}$ is the ratio between laser intensity and the saturation intensity where Ω is the Rabi frequency.

Consider atoms illuminated by two counter-propagating light beams of identical intensity, polarisation and frequency. If the laser detuning is negative with respect to the atomic resonance (‘red-detuned’), the frequency of the light of the beam opposing the atom’s motion is Doppler shifted towards the blue in the atomic rest frame and is therefore closer to resonance. Thus the atom absorbs photons preferentially from the beam that opposes its motion. Hence the atoms experience a viscous force opposing their motion and this force is proportional to their velocity. The same principle can be extended to three dimensions using three pairs of counter-propagating light beams in orthogonal directions (optical molasses).

As the atoms are cooled their Doppler frequency changes. Once the velocity change is large enough the laser radiation is no longer in resonance with the atoms and cooling stops. There are two possible methods of compensating for the changing Doppler shift as the atoms decelerate: changing the laser frequency [29] [30] [31], or spatially varying the atomic resonance frequency using a magnetic field [32] [33].

The heating associated with spontaneous emission leads to a limit on the temperature that can be reached using Doppler cooling. Even though the average momentum from spontaneous emission is zero, the root-mean-square (rms) value of the momentum is non-zero. This leads to a Brownian motion-like behaviour by the atoms. The Doppler limit [34] is given by $T_D = \frac{\hbar\Gamma}{2k_B}$ and for Rubidium this is $146 \mu K$.

2.2.2 Sub-Doppler cooling

Doppler cooling theory assumes a basic two-level system. However, alkali atoms have hyperfine structure and Zeeman sublevels, so they can be cooled to temperatures much lower than the Doppler limit via more sophisticated processes. Sub-Doppler cooling depends on multiple (normally degenerate) ground states, ‘light shifts’ of ground states, optical pumping among ground states and polarization gradients in the light field. The viscous damping experienced by the atoms in sub-Doppler cooling is much greater than that in Doppler cooling. However, the

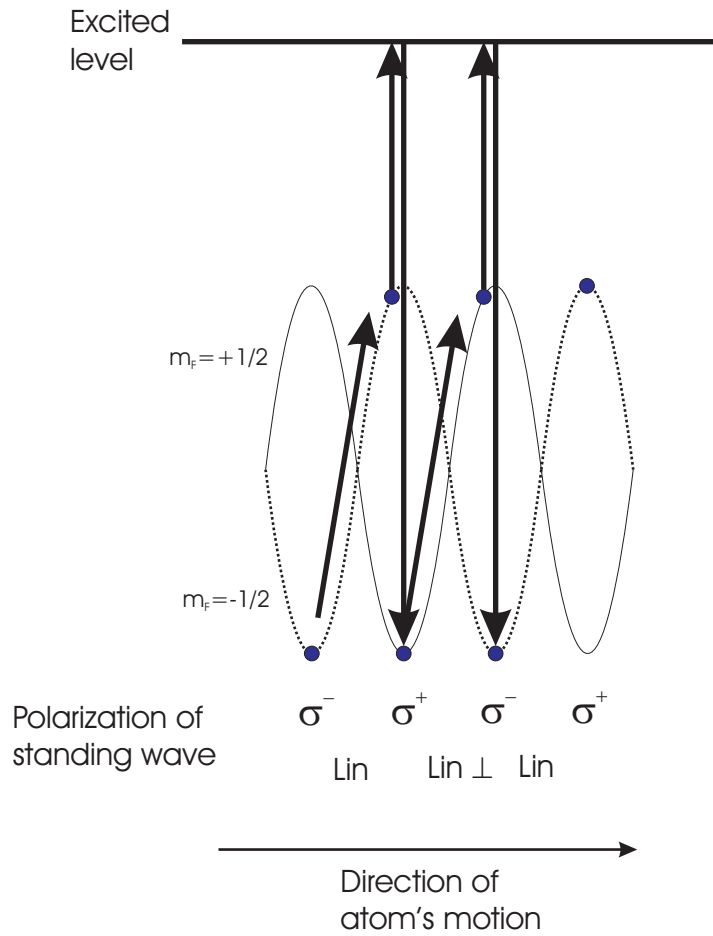


Figure 2.3: An illustration of the principles of Sisyphus cooling. As the atoms climb the potential hill their kinetic energy is reduced. When they reach the top of the hill they are optically pumped to the valley. Thus atoms are continually losing kinetic energy which translates to a systematic reduction of temperature.

cooling capture range is small so atoms must be initially Doppler cooled before sub-Doppler cooling can occur.

When a laser beam is incident on an atom, the energy levels are perturbed by the light field. Light shifts cause a splitting of the ground state energy. For $J = 1/2$, the ground state is split into two levels $m_J = +1/2$ and $m_J = -1/2$. However, because of the standing wave formed by two counter-propagating beams the energy levels will vary periodically across the wavelength of the standing wave (see Figure 2.3). Another notable difference is that when the orientation of the atom (its m_F state) is taken into account, atomic interaction with the light field depends upon the polarisation of the radiation. Different states in multilevel atoms are coupled differently to the light field depending on the polarization, e.g. σ^+ polarization drives $\Delta m_F = +1$ transitions and σ^- polarization drives $\Delta m_F = -1$ transitions. The two important polarization cases in sub-Doppler cooling are the linear \perp linear configuration and the $\sigma^+ - \sigma^-$ configuration. They both lead to temperatures below the Doppler limit but by different mechanisms. A full treatment of sub-Doppler cooling is given in [35].

For linear \perp linear polarisation gradient cooling, the two linearly polarized counter-propagating beams of the same frequency interfere and create a strong polarization gradient. The polarization changes from linear to σ^+ in $\lambda/4$ (see Figure 2.3). When the atom absorbs a photon and is excited there are two possible outcomes: the atom decays to the original level, or it decays to a different magnetic sublevel. For the former case the atom receives a random momentum kick and its energy does not change. For the latter case, the spontaneously emitted photon is of a higher frequency than the one that was absorbed (Figure 2.3). This means that overall, the atom loses energy, leading to a reduction in its velocity and therefore temperature. Careful selection of the laser radiation detuning makes it more probable for an atom to absorb a photon at the top of the potential ‘hill’ than at the bottom. This leads to a reduction in the energy of the atoms i.e. cooling. Figure 2.3 illustrates the principles of linear \perp linear polarization gradient cooling.

Linear \perp linear polarization gradient cooling is also called Sisyphus cooling after the Greek mythological character Sisyphus. He was doomed by the Greek gods to forever roll a large boulder to the top of a hill.

For $\sigma^+ - \sigma^-$ polarization gradient cooling, two counter-propagating light beams with opposite circular polarisation create a light field where the polarization remains linear but rotates in direction about the beam's axis. When the atoms travel along the axis of the beams the light shifts of the ground state sublevels remain constant and therefore Sisyphus cooling does not occur in this case. For a stationary atom the population distribution is symmetric across the magnetic sublevels and therefore the atom absorbs photons from both beams equally resulting in no net force on the atom. When the atoms are moving through a polarization gradient, there is a difference in the scattering rate between the two counter-propagating beams. Since the transition rate between different pairs of magnetic sublevels of excited and ground states (Clebsch-Gordon coefficients) depends on the orientation of the electron spin and the polarization of the radiation driving the transition, the atom will preferentially absorb photons from the laser beam which opposes its motion. The distribution across the magnetic substates is then no longer symmetric and creates an imbalance in the absorption rate of photons from the two beams, giving a net force that opposes the atom's motion.

While the sub-Doppler viscous damping is much larger than that of the Doppler cooling mechanism, the resultant temperature is still limited by the heating caused by spontaneous emission. Temperatures of about one order of magnitude above the recoil limit can be attained. The recoil temperature is given by $T_r = (\hbar k)^2 / mk_B$ and for rubidium this is $T_r = 361.96$ nK. While nowadays evaporative cooling is the most widely-used technique to achieve cloud temperatures in the nK regime, there are other laser cooling techniques used to achieve those temperatures. Two of them are Velocity-Selective Coherent Population Trapping (VSCPT) [36] and Raman cooling [37]. Neither Doppler nor sub-Doppler cooling contain a dependence on position so optical molasses does not localise the atoms. In order to trap atoms,

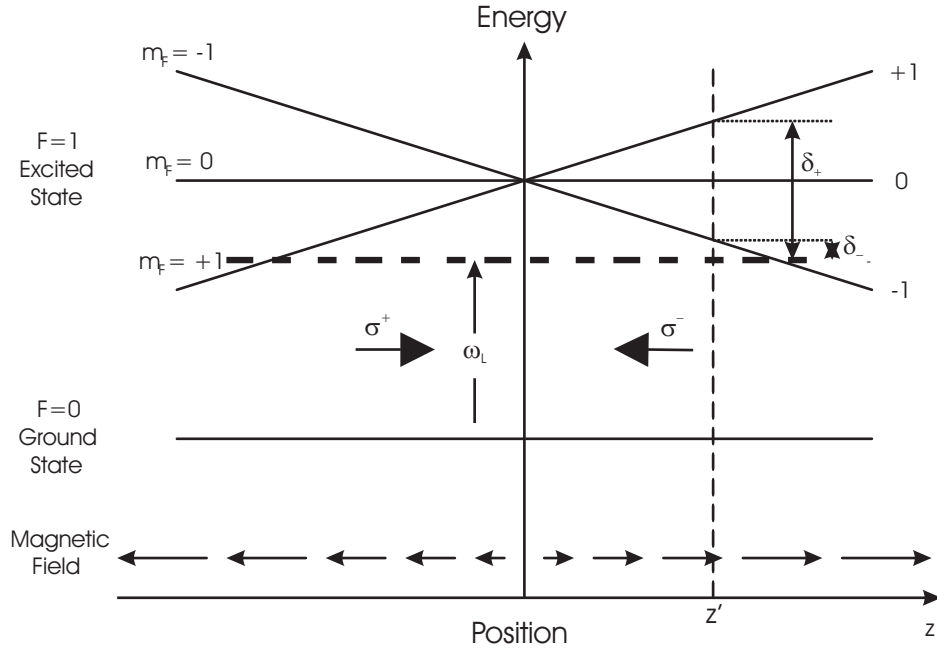


Figure 2.4: Arrangement for a MOT in one-dimension. At point $z = z'$ the atoms are closer to resonance with the σ^- beam. Therefore the atom is driven towards the centre of the trap. Even though the scheme is described for $F = 0 \rightarrow F' = 1$ transition, it works well for any $F \rightarrow F' = F + 1$ transition.

magneto-optical traps were developed.

2.3 Magneto-optical traps

Most of the cooling in a typical BEC experiment occurs in the magneto-optical trapping (MOT) stage. Such traps use light and magnetic fields to confine large numbers of atoms and cool them to temperatures much less than $30 \mu K$. The first demonstration of a MOT was in 1987 [38] and since then there has been extensive treatment of MOTs in the literature [39], [40], [41], [42]. The various possible MOT orientations include the four-beam MOT [43], the pyramidal MOT [44] and the surface MOT [45].

A magnetic field needs to be present to localize the atoms in space and is normally generated by a pair of anti-Helmholtz coils. The ground state and the excited magnetic states are shifted in energy by the Zeeman effect. The excited state has three Zeeman components (for a $F = 1$ state) and the transition frequencies

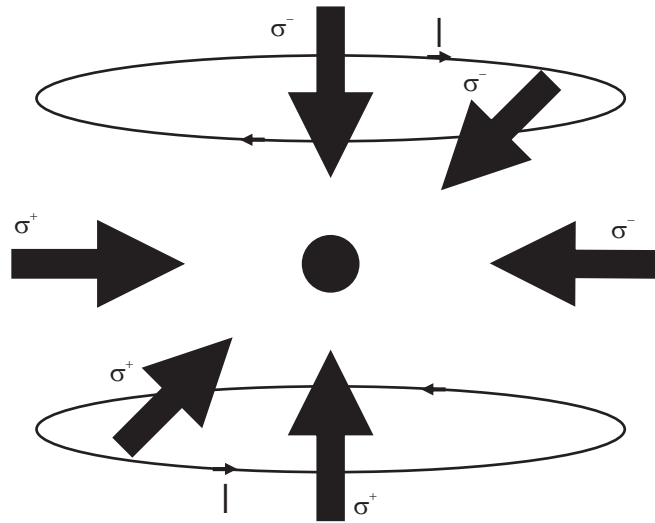


Figure 2.5: Direction and polarization configuration of a six beam MOT.

of these states vary with magnetic field and therefore position. The atoms are illuminated by two red-detuned ($\delta < 0$) counter-propagating beams of opposite circular polarization. The imbalance in the forces experienced by the atoms by the two beams leads to a resultant force on the atoms. A schematic of the principles of a MOT is given in Figure 2.4.

2.3.1 Six-beam MOT

Figure 2.4 illustrated the principles of a MOT in one dimension. To extend the principle to three dimensions two further pairs of counter-propagating beams of opposite circular polarization are added in orthogonal directions to the original beams. This is illustrated in Figure 2.5.

The polarization configuration in a MOT seems to imply that only $\sigma^+ - \sigma^-$ polarization gradient cooling occurs. This would be true if the atoms moved only along the axis of the beams. However, in practice atoms move in random directions and therefore at intermediate points between the axes the polarization is not well defined. At these points, both types of sub-Doppler cooling occur.

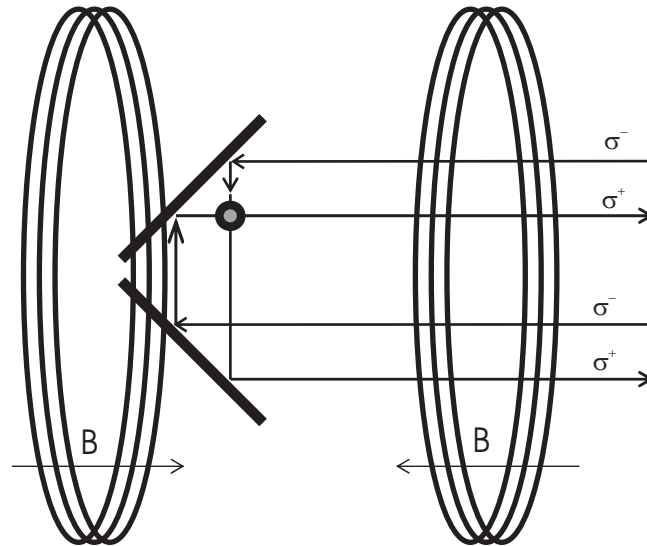


Figure 2.6: Cross-section of the pyramidal MOT and the resulting polarization configuration.

2.3.2 Pyramidal MOT

The pyramidal MOT is a way of generating the same radiation field as in a six-beam MOT, except a pyramidal MOT only requires one input beam to produce the same configuration of light polarizations as a standard six-beam MOT. The original pyramidal MOT consisted of a large beam of σ^- polarized light incident on a conical hollow mirror [44]. This was then modified to include a small aperture at the vertex in order to not only confine atoms but enable transfer of atoms into the experimental MOT [46]. The first reflection on the mirror produces a pair of counter-propagating beams with opposite polarization. The second reflection produces a σ^+ retro-reflected beam. This occurs in all three dimensions creating the required polarization configuration. Figure 2.6 illustrates the setup of a pyramidal MOT.

2.4 Magnetic trapping of neutral atoms

In most BEC experiments magnetic traps are used to confine laser cooled atoms and compress the atomic cloud in order to achieve the high collision rates needed for efficient evaporative cooling. We shall firstly describe the atomic properties

that enable magnetic trapping of neutral atoms and how they are exploited for that purpose. Then we shall describe a general class of magnetostatic traps that confine these atoms. Magnetic trapping of neutral atoms was first observed in 1985 [47]. Shortly afterwards, orders of magnitude improvements in density and number of trapped atoms were achieved at MIT and in Amsterdam using superconducting traps and different loading schemes [48] [49] [50]. Magnetic forces are strong for atoms with unpaired electrons, such as the alkali metals, resulting in atomic magnetic moments μ of the order of a Bohr magneton. The interaction energy between a magnetic dipole and an external magnetic field \vec{B} is given by $-\vec{\mu} \cdot \vec{B} = \mu B \cos\theta$. In a classical picture, the angle θ between the magnetic moment and the magnetic field is constant due to the rapid precession of $\vec{\mu}$ around the magnetic field axis. For weak magnetic fields, the energy levels of the atom in a magnetic field is $E(m_F) \approx m_F g_F \mu_B B$ where g_F is the g-factor and m_F is the quantum number related to the z-component of the total angular momentum F. The term $\cos\theta$ is replaced by m_F/F since in the classical picture, a constant angle θ is equivalent to the system remaining in the same m_F state. Magnetic trapping of atoms requires a local minimum in the magnetic potential energy $E(m_F) < 0$. High-field seeking states cannot be trapped because Maxwell's equations do not allow a magnetic field maximum in free space [51], therefore this automatically requires we must have our atoms in the 'weak-field seeking states' ($m_F g_F > 0$) for them to be able to be trapped magnetically.

Weak-field seeking states are not the states of lowest energy thus since those magnetic traps only confine weak-field seeking states, atoms can be lost from the trap by transitions to strong-field seeking states. Such transitions can be induced by the motion in the trap because an atom sees a field in its moving frame which is changing in magnitude and direction. The trap is only stable if the atom's magnetic moment adiabatically follows the direction of the magnetic field. This requires that the rate of change of the field direction be slower than the precession of the magnetic moment:

$$\frac{d\theta}{dt} < \frac{\mu|B|}{\hbar} \quad (2.38)$$

where θ is the orientation angle defined above. The upper bound for this rate of change would be the trapping frequency. This adiabatic condition is violated in regions of very small magnetic fields leading to trap loss by spin flips to untrapped states. These flips are called Majorana flops [52].

2.4.1 Zeeman effect on the hyperfine ground states

Under the influence of a static magnetic field B , the Zeeman energy of the two hyperfine levels of the ground configuration is given by the Breit-Rabi formula [53] [54]. For the case of vanishing orbital angular momentum, this Zeeman energy is given as

$$E_{F,m_F}(B) = (-1)^F \frac{1}{2} \hbar \omega_{hf} \sqrt{1 + \frac{4m_F}{2I+1}x + x^2} + const. \quad (2.39)$$

where x is given as

$$x = \frac{(g_I + g_S)\mu_B B}{\hbar \omega_{hf}} \quad (2.40)$$

The numerator is the Zeeman energy and it is divided by the hyperfine splitting $E_{hf} = \hbar \omega_{hf}$ of the ground state. Figure 2.7 shows the Zeeman effect on the hyperfine ground state. In this graph, y is given as $E_{F,m_F}(B)/\hbar \omega_{hf}$ in equation 2.39 chosen so that for $x=0$ the energies are $E/\hbar \omega_{hf} = \pm 1/2$ and x is given as equation 2.40. The small contribution from the nuclear moment is usually neglected as $g_I \ll g_S$.

In most static magnetic traps the magnetic fields give lower Zeeman energy than the hyperfine splitting of the ground state. Under conditions where $x \ll 1$, equation 2.39 can be approximated as

$$\frac{E_{F,m_F}(B)}{\hbar \omega_{hf}} = (-1)^F \left[\frac{1}{2} + \frac{(-1)^F}{2I+2}x + \frac{4 - m_F^2}{16}x^2 \right] \quad (2.41)$$

where

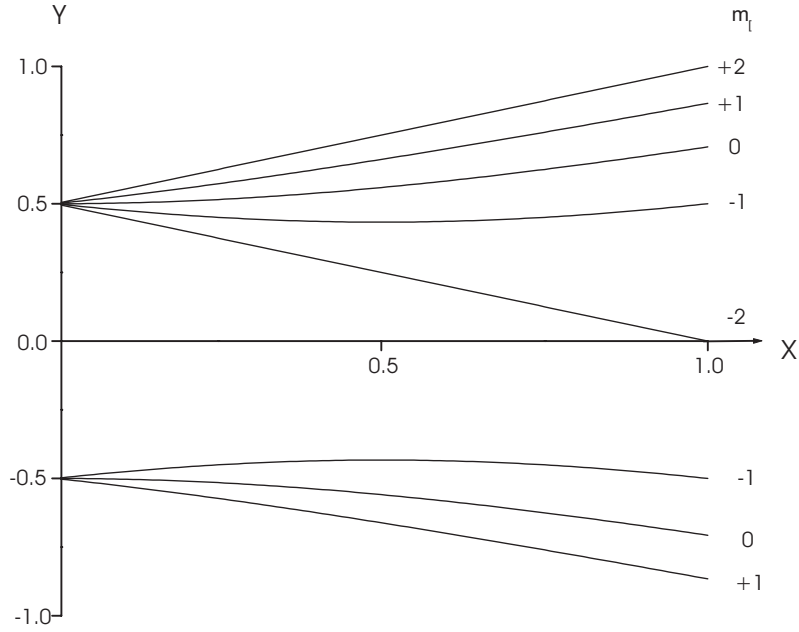


Figure 2.7: Zeeman-effect in the hyperfine levels of the ground state in rubidium-87. The energies of the magnetic sublevels m_F are shown as function of parameter defined in equation 2.40. $I = \frac{3}{2}$, the nucleus g-factor is $g_I = 0.995 \cdot 10^{-3}$, electron g-factor is $g_S = 2.0023$ and the hyperfine splitting is $\omega_{hf} = 2\pi \cdot 6.8346826128(5)$ GHz. For our magnetic trap, the cloud of atoms at the centre experience a magnetic field of $B=100$ Gauss (or 0.01 Tesla) maximum. This would correspond to $x \approx 0.041$.

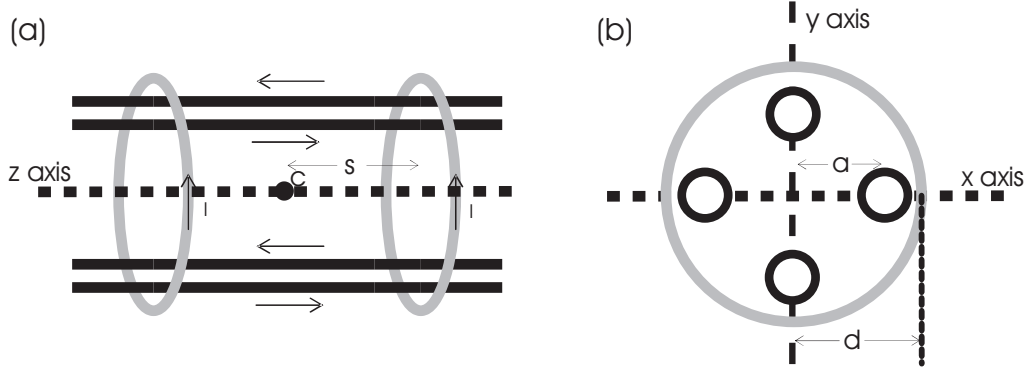


Figure 2.8: A schematic of a Ioffe-Pritchard trap: (a) illustrates the physical arrangement of the bars and pinch coils and the directions of the currents. Point c is the centre of the magnetic trap where $x = y = z = 0$, (b) illustrates the direction of the currents in the Ioffe bars.

$$g_F = (-1)^F \frac{1}{I+1} \frac{g_S}{2} \quad (2.42)$$

The first term gives the hyperfine splitting of the ground state when magnetic field $B = 0$. The second term is the linear Zeeman effect. The third term is the quadratic Zeeman effect which is generally not very important for the strengths of the magnetic fields near the centre of most magnetic traps. It is the dominant linear Zeeman effect that determines the magnetic trapping properties. From figure 2.7, it can be seen that there are certain m_F states in which atoms seek low magnetic fields to be in the low-energy region. There are a total of two of such low-field seeking states, $|F = 2, m_F = 2, 1 \rangle$ arising from the upper hyperfine level and finally $|F = 1, m_F = -1 \rangle$ in the lower hyperfine level. The last of these is the state used in this experiment.

2.4.2 The Ioffe-Pritchard trap

A Ioffe-Pritchard (I-P) trap is formed by a linear quadrupole field and an axial field. The linear quadrupole field is produced by 4 straight wires (Ioffe bars) parallel to the z -axis (Figure 2.8 (a)), each carrying an equal magnitude of current but opposite in direction to its nearest neighbours (Figure 2.8 (b)). The magnetic field along the z -axis is therefore zero. The axial field is provided by two end coils

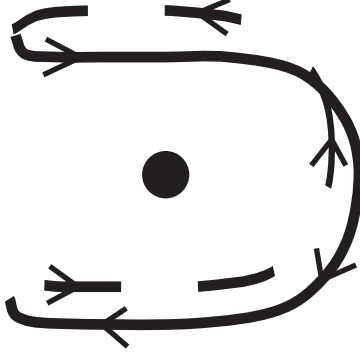


Figure 2.9: Schematic of a baseball coil. The black circle denotes the position of the minimum of the magnetic field where atoms are trapped while the arrows denote the direction of the current.

(pinch coils) with current flowing in the same direction and with equal magnitude in both coils. This is illustrated in Figure 2.8 (a). The pinch coils therefore add an axial magnetic field to the magnetic field produced by the Ioffe bars. The field along the z -axis is no longer zero and therefore there is negligible probability of an atom undergoing Majorana flopping. To provide the local minimum in the B -field, it is required that the two pinch coils have a separation larger than that for a Helmholtz configuration. Our magnetic trap also falls in this class because while the geometry is different from that given in Figure 2.8, the magnetic field it generates around our trapping region of interest is similar to that of the IP trap. Since the coil winding is such that it resembles the seam of a baseball, it is referred to as a baseball trap as shown in Figure 2.9.

The configuration shown in Figure 2.8 produces a small axial bias field throughout while the pinch coils produce a field given as $B_1 = B_0 + \frac{B''}{2}(z^2 - \frac{r^2}{2})$ where B'' is the position-dependent magnetic field differentiated twice, z is the axial distance from the centre of the trap, r is the radial distance from the centre of the trap and B_0 is the bias field at the centre of the trap. In the meantime, the Ioffe bars produce an axially symmetric magnetic field given as $B_2 = \beta r$ where β is the magnetic gradient generated by the Ioffe bars. The total field of the configuration is simply $B = \sqrt{B_1^2 + B_2^2}$. Applying Maxwell's equations (and assuming axial symmetry), we get the following profile for the magnitude of the field $|\vec{B}|$

$$|\vec{\mathbf{B}}| \approx B'' z^2 + \left(\frac{\beta^2}{B_0} - \frac{B''}{2} \right) r^2 \quad (2.43)$$

for very small clouds where the trapping potential can be well-approximated by an anisotropic harmonic potential.

The Ioffe-Pritchard trap has two different regimes. For temperature $k_B T < \mu B_0$, the cloud experiences the potential of a 3D anisotropic harmonic oscillator. For $k_B T > \mu B_0$, the potential is linear along the radial direction and harmonic along the axial direction.

From equation 2.43, it can be seen immediately that we can tighten the radial trapping frequency by lowering B_0 whilst keeping β constant. Experimentally, this is usually carried out using a pair of compensation coils (bias coils) whose field is set to null the magnetic field at the centre of the original Ioffe trap. The overall field at the centre of the trap must remain high enough to suppress Majorana flops, i.e. about 1 G. To fine-tune the remaining field after cancellation, we have another pair of coils called the secondary bias coils. Low-fields can be achieved with the combination of the bias coils and the baseball trap. Implementation of current control will be described in the next chapter.

2.5 Evaporative cooling

Unlike standard laser cooling, evaporative cooling can go below the recoil limit. This method is analogous to evaporation of a cup of coffee. The energetic particles escape the cup and then the remaining particles rethermalise to a new thermal equilibrium at a temperature lower than that initially because the average energy of the system has fallen. For atoms in magnetic traps, the hotter atoms are removed by inducing RF transitions. This cooling method clears the final hurdle before Bose-Einstein Condensation and to date, some form of evaporative cooling has been used in all experiments where condensates are formed. This technique is a very useful cooling method that does not suffer from the limitations which exist

with optical cooling method like the Doppler-limit and the recoil limit. The idea of evaporative cooling was first introduced for trapped atomic hydrogen [49]. A review on evaporative cooling is given by [55] and [56].

2.5.1 Evaporative cooling

Here we briefly sketch the principles of evaporative cooling. The description is based on the model of evaporative cooling as introduced by [19] and [56]. Evaporative cooling is based on the preferential removal of atoms with energy above a certain truncation energy ϵ_t from the trap and subsequent thermalization by elastic collisions. For a constant truncation barrier ϵ_t (plain evaporation) elastic collisions between atoms in a trap produce atoms of energies higher than ϵ_t which are removed (or 'evaporated') from the trap. The evaporation rate per atom is given as

$$\tau_{ev}^{-1} = \frac{\dot{N}_{ev}}{N} = n(0)v_T\sigma e^{-\eta} \frac{V_{ev}}{V_e} \quad (2.44)$$

where $\sigma=8\pi a^2=7.9 \times 10^{-16} \text{ m}^2$ is the elastic collision cross section, and the truncation parameter η is given by

$$\eta = \frac{\epsilon_t}{k_B T} \quad (2.45)$$

assuming that $V_{ev} = V_e$ is the effective volume for evaporation [56]. As hotter atoms are ejected from the trap, the average energy of the cloud falls. As the temperature has been reduced, η becomes larger and the evaporation rate is exponentially suppressed. For a continuous cooling process, the truncation energy ϵ_t is reduced such that η remains constant (forced evaporative cooling). For forced evaporative cooling at constant η ,

$$T \propto N^{\alpha_{ev}} \quad (2.46)$$

where the efficiency parameter

$$\alpha_{ev} = \frac{d \ln(T)}{d \ln(N)} \quad (2.47)$$

depends only on the truncation parameter η . During evaporative cooling, the effective volume also decreases and this can be expressed as

$$V_e \approx T^\delta \quad (2.48)$$

where $\delta = 5/3$ for a Ioffe trap at high temperatures (the linear limit) and $\delta = 3/2$ for a Ioffe trap at low temperatures (harmonic limit). Combining equations 2.46 and 2.48 and the definition $V_e \approx N/n(0)$ shows that despite significant loss of atoms during the evaporation process, the peak cloud density at the centre of the trap can remain constant or even increase provided that $\alpha_{ev} \geq 1/\delta$. Given that the elastic collision rate is $\tau_{el}^{-1} \propto n(0)T^{1/2}$, even though temperature decreases, the increase in density can be large enough that the ‘runaway’ evaporative cooling condition remains fulfilled, namely

$$\frac{d \ln(n\sqrt{T})}{d \ln(N)} = 1 - 2\alpha_{ev} < 0 \quad (2.49)$$

In practice, evaporative cooling is limited by various loss processes like background collisions where atoms collide with particles in the vacuum background and for very high densities, two-body and three-body inelastic collisions. In general, the atomic loss rate τ_i^{-1} for i-body collisions is expressed by the rate constant G_i given as

$$\tau_i^{-1} \equiv \frac{\dot{N}_i}{N} = -G_i n(0)^{(i-1)} \frac{V_{ie}}{V_e} \quad (2.50)$$

where the reference volumes for i-body collisions are defined as

$$V_{ie} \equiv \int dr \left(\frac{n(r)}{n(0)} \right)^i \quad (2.51)$$

For two and three-body inelastic collisions, these reference volumes can be calculated numerically while for background collisions this reference volume is simply the one introduced in equation 2.16. Evaporative cooling is most efficient for large ratio R_i which is the ratio between the elastic collision rate and the rate of the

various loss processes. This ratio is also sometimes called ‘ratio of good to bad collisions’ given by

$$R_i \equiv \frac{\dot{N}_{ev}}{\dot{N}_i} = \frac{n(0)v_T\sigma\frac{V_{ev}}{V_e}e^{-\eta}}{n^{-1}(0)G_i\frac{V_{ie}}{V_e}} \equiv \frac{1}{\lambda_i}\frac{V_{ev}}{V_e}e^{-\eta} \quad (2.52)$$

In this case,

$$\lambda_1 = \frac{\tau_i^{-1}}{\tau_{el}^{-1}} = \frac{n^{(i-2)}(0)G_i}{v_T\sigma}\frac{V_{ie}}{V_e} \quad (2.53)$$

and where the elastic collision rate is given as

$$\tau_{el}^{-1} = n(0)\sigma v_T \quad (2.54)$$

In typical BEC experiments, in the earlier stages of evaporative cooling the peak density for most initial clouds is low enough that only background collisions need to be considered.

2.5.2 RF-evaporative cooling

As mentioned above, evaporative cooling is performed by selectively removing the hotter atoms from the trap so that the gas cloud then cools down. The energy selective removal of the atoms from the trap is achieved by driving atomic transitions from trapped states to untrapped Zeeman states with an oscillating magnetic field of angular frequency ω_{rf} . The atoms undergo the transitions only at positions where the resonance condition

$$\hbar\omega_{rf} = g_F\mu_B|B(r)| \quad (2.55)$$

is achieved. So the truncation energy ϵ_t at which atoms in the state m_F are ejected from the trap is related by the interaction energy of an atom with an external magnetic field $E = -\mu \cdot B$ and the radio frequency ω_{rf} by

$$\epsilon_t = m_F\hbar(\omega_{rf} - \omega_0) \quad (2.56)$$

where $\omega_0 = g_F \mu_B |B(0)|/\hbar$ is the resonance radio frequency at the centre of the trap. Experimentally, evaporative cooling is performed by lowering the radio frequency from a starting value towards the resonance frequency in specific stages where each stage is optimised by measuring the resulting phase space density.

2.6 Sub-shot noise measurements of atom number

In this section, we give a theoretical introduction to the project that we want to implement after obtaining BEC, in particular dipole trapping and aspects of this technique relevant to the experiments we wish to do. The next part then talks about the Mott Insulator State which we want to achieve as a preliminary to quantum information processing.

2.6.1 Dipole trapping of neutral atoms

This subsection is divided into two parts. Firstly, we obtain the two important properties of dipole traps, the dipole potential and the scattering rate. Then we discuss red-detuned dipole trapping which is more relevant to us. A more formal treatment of dipole trapping can be found in [57].

The dipole potential

When an atom is illuminated by laser light, the electric field \vec{E} induces an atomic dipole moment \vec{p} which oscillates with a frequency equal to its driving frequency ω . The amplitude \tilde{p} is related to the electric field amplitude \tilde{E} by the relation $\tilde{p} = \alpha \tilde{E}$ where α is the complex polarisability of the atom dependent upon ω .

The electric field and the induced dipole moment are given in their usual complex notations $\vec{E}(r, t) = \hat{e} \tilde{E}(r) \exp(-i\omega t) + c.c$ and $\vec{p}(r, t) = \hat{e} \tilde{p}(r) \exp(-i\omega t) + c.c$ where \hat{e} is the unit polarisation vector. Given these, the interaction potential between the electric field and the induced dipole moment is given as

$$U_{dip} = -\frac{1}{2} \langle \vec{p} \vec{E} \rangle = -\frac{1}{2\epsilon_0 c} \text{Re}(\alpha) I \quad (2.57)$$

where I is the field intensity $I = 2\epsilon_0 c |\tilde{E}|^2$, ϵ_0 is the electric constant and c is the speed of light in vacuo. The power absorbed by the atom in the oscillator model and re-emitted as dipole radiation is given by

$$P_{abs} = \langle \dot{p} \vec{E} \rangle = \frac{\omega}{\epsilon_0 c} \text{Im}(\alpha) I \quad (2.58)$$

Now if we consider the light as a stream of photons each with energy $\hbar\omega$, this absorption can be interpreted as scattering with cycles of absorption and reemission. The scattering rate is then given by

$$\Gamma_{sc}(r) = \frac{P_{abs}}{\hbar\omega} = \frac{1}{\hbar\epsilon_0 c} \text{Im}(\alpha) I(r) \quad (2.59)$$

Note that now we have expressed field intensity as a position-dependent variable which is a more realistic view of beam intensities. These expressions are valid for any polarisable neutral particle in some oscillating electric field.

To calculate the polarisability term α , we first consider the atom in Lorentz's model of a classical oscillator and view the electron of mass m_e and charge e as bound elastically to the core with an oscillation frequency ω_0 corresponding to the optical transition frequency. We then calculate the polarisability by integration of the electron's equation of motion $\ddot{x} + \Gamma_\omega \dot{x} + \omega_0^2 x = -\frac{eE(t)}{m}$ with the result

$$\alpha = \frac{e^2}{m_e} \frac{1}{\omega_0^2 - \omega^2 - i\omega\Gamma_\omega} \quad (2.60)$$

where

$$\Gamma_\omega = \frac{e^2 \omega^2}{6\pi\epsilon_0 m_e c^3} \quad (2.61)$$

Introducing the on-resonance damping rate $\Gamma = (\omega_0/\omega)^2 \Gamma_\omega$, equation 2.60 becomes

$$\alpha = 6\pi\epsilon_0 m_e c^3 \frac{\Gamma/\omega_0^2}{\omega_0^2 - \omega^2 - i\omega^3/\omega_0^2 \Gamma} \quad (2.62)$$

In the semiclassical approach, the atom must be treated as a two-level quantum system interacting with a radiation field. The damping rate (or scattering rate now) is determined by the dipole matrix element between the ground state and the excited state. However, for the D lines of alkali atoms such as Na, K, Rb and Cs, the classical result agrees with the true spontaneous decay rate of the excited state to within a few percent. In fact, for many atoms with a strong dipole-allowed transition from the ground state, the classical formula provides a very good approximation to its true decay rate.

So given the expression for polarisability and also for low saturation and large detunings, the dipole potential and scattering rate are given as

$$U_{dip}(r) = -\frac{3\pi c^2}{2\omega_0^3} \left(\frac{\Gamma}{\omega_0 - \omega} + \frac{\Gamma}{\omega_0 + \omega} \right) I(r) \quad (2.63)$$

$$\Gamma_{sc}(r) = \frac{3\pi c^2}{2\hbar\omega_0^3} \left(\frac{\omega}{\omega_0} \right)^3 \left(\frac{\Gamma}{\omega_0 - \omega} + \frac{\Gamma}{\omega_0 + \omega} \right)^2 I(r) \quad (2.64)$$

In most experiments, the laser frequency is sufficiently close to the transition frequency such that the detuning $\Delta = \omega - \omega_0$ fulfills the inequality $|\Delta| \ll \omega_0$. In this case, we can apply the rotating-wave approximation [58] and set $\omega/\omega_0 \approx 1$. The general case for optical potentials and scattering rate then simplifies to

$$U_{dip}(r) = \frac{3\pi c^2}{2\omega_0^3} \frac{\Gamma}{\Delta} I(r) \quad (2.65)$$

$$\Gamma_{sc}(r) = \frac{3\pi c^2}{2\hbar\omega_0^3} \left(\frac{\Gamma}{\Delta} \right)^2 I(r) \quad (2.66)$$

These expressions tell us two important features of dipole trapping. The first is the interaction with respect to the sign of the detuning. For red-detuned dipole traps which we will be working with, $\Delta < 0$ and this tells us that the atoms tend to move towards regions of high field intensity where there is a potential minima. However, for blue detuning $\Delta > 0$, atoms stay away from regions of high intensity. The second is the scaling with intensity and detuning. While the dipole potential is inversely proportional to Δ , scattering rate is inversely proportional

to Δ^2 . Therefore, for a certain potential depth, it would be useful to have dipole traps with large detunings and high intensities.

The focused beam trap

There are three types of red-detuned dipole traps. They are the focused beam trap, the standing wave trap and the crossed-beam trap. We shall concentrate on the focused beam trap because this trap type is the one we shall be using in our experiment.

The focused beam trap is the simplest type of dipole trap that provides three-dimensional confinement of atoms and is formed by nothing more than one beam which focuses via some lens onto a spot of high light intensity. The spatial intensity distribution of a focused Gaussian beam (FB) with power P propagating along the z -axis is given by

$$I_{FB}(r, z) = \frac{2P}{\pi w^2(z)} \exp\left(-2\frac{r^2}{w^2(z)}\right) \quad (2.67)$$

where r is the radial coordinate. The $1/e^2$ radius of the beam $w(z)$ depends on the axial coordinate z via

$$w(z) = w_0 \sqrt{1 + \left(\frac{z}{z_R}\right)^2} \quad (2.68)$$

where Rayleigh length is $z_R = \pi w_0^2/\lambda$. The trap depth is given by $\tilde{U} = U_{dip}(r = z = 0)$. If the thermal energy $k_B T$ is much smaller than the trap depth \tilde{U} , then the dipole potential can be approximated by an harmonic oscillator:

$$U(r) \approx -\tilde{U} \left[1 - 2\left(\frac{r}{w_0}\right)^2 - \left(\frac{z}{z_R}\right)^2 \right] \quad (2.69)$$

and the oscillation frequencies are given by $\omega_r = \sqrt{4\tilde{U}/mw_0^2}$ and $\omega_z = \sqrt{2\tilde{U}/mz_R^2}$. Automatically, the radial frequency frequency is always tighter than the axial frequency by a factor of $\omega_r/\omega_z = \sqrt{\frac{2\pi^2}{\lambda^2} \omega_0^2}$.

2.6.2 The Mott Insulator State

With the theory of dipole trapping established, experimental realisation of such traps was the next step towards quantum computation with neutral atoms. We begin with the 1D optical lattice where one pair of counter-propagating laser beams interfere and gives a trap potential in 1D while the atoms are weakly trapped by a magnetic field in the other two dimensions. Loading of BEC into a 1D dipole trap was first achieved by Stamper-Kurn et al [59] and this 1D version could theoretically be extended to the 3D version with three pairs of counter-propagating laser beams instead of one. There are many novel features of a BEC loaded into a 3D lattice and one of them is the demonstration of the transition between the superfluid state and the Mott Insulator state [8]. We wish to reproduce the Mott insulator state of our atom cloud before moving on to qubit operations with neutral atoms. This section gives an introduction to the dynamics of a BEC in an optical lattice (or arrays of dipole traps in general) brought about by interatomic interactions.

We start by writing the Hamiltonian operator for bosonic atoms in some external trapping potential

$$H = \int d^3x \psi^\dagger(r) \left(-\frac{\hbar^2}{2m} \nabla^2 + V(r) + V_T(r) \right) \psi(r) + \frac{1}{2} \frac{4\pi a_s \hbar^2}{m} \int d^3x \psi^\dagger(r) \psi^\dagger(r) \psi(r) \psi(r) \quad (2.70)$$

with $\psi(r)$ being a boson field operator for atoms in some given state, $V(r)$ being the potential related to an optical lattice or an array of dipole traps and $V_T(r)$ being an additional slow-varying external trapping potential like a magnetic trapping potential. The interaction between the atoms is approximated by a short-range pseudopotential with a_s being the s-wave scattering length and m being the mass of the atoms. For single atoms the eigenstates are Bloch wavefunctions and the superposition of these wavefunctions provide a set of Wannier functions well localised on individual lattice sites. We assume the energy of the atoms is much less than the excitation energy to the second Bloch band. If we were to expand

the field operators in the Wannier basis and keep only the lowest vibrational levels $\psi(r) = \sum_i b_i w(r - r_i)$, equation 2.70 reduces to the Bose-Hubbard Hamiltonian (BHM)

$$H = -J \sum_{i,j} b_i^\dagger b_j + \sum_i \epsilon_i \hat{n}_i + \frac{1}{2} U \sum_i \hat{n}_i (\hat{n}_i - 1) \quad (2.71)$$

where $\hat{n}_i = b_i^\dagger b_i$ count the number of atoms at lattice site i and where the annihilation and creation operators b_i and b_i^\dagger obey the commutation relations $[b_i, b_j^\dagger] = \delta_{ij}$. $U = 4\pi a_s \hbar^2 \int d^3x |w(r)|^4 / m$ corresponds to the interaction strength of on site repulsion between two atoms on site i , $J = \int d^3x w^*(r - r_i) [-\frac{\hbar^2}{2m} \nabla^2 + V(r)] w(r - r_j)$ is the hopping matrix element between adjacent sites i, j and $\epsilon_i = \int d^3x V_T(r) |w(r - r_i)|^2 \approx V_T(r_i)$ describes the energy offset of each site provided by the slowly varying external potential.

The BHM predicts that there will be a phase transition between the superfluid (SF) state and the Mott insulator (MI) state at low temperatures and when the on site interaction energy U is much larger than the tunneling matrix element J [60]. In an optical lattice the interaction energy U can be increased by increasing the laser intensity to make the atomic wave function more and more localised while the tunneling matrix element is reduced. According to mean-field theory [60], the critical value of the MI-SF transition for the $n = 1$ phase is at $U/zJ \approx 5.8$ with $z = 2d$ being the number of nearest neighbours. The dipole trap depth required for this transition is typically in the few tens of recoil energies. At MI stage the occupation number per site is pinned at integer $n = 1, 2, \dots$ and this corresponds to a commensurate filling of the optical lattice. This system therefore represents an optical crystal. Another way of looking at this phase transition is in terms of the Heisenberg uncertainty relation involving the uncertainty in the number of atoms in the system and the uncertainty in the phase of the macroscopic wave function $\Delta N \cdot \Delta \phi \geq \frac{\hbar}{2}$. In the MI stage the uncertainty in the number of atoms reduces to that below the Standard Quantum Limit (SQL) while phase definition suffers. When this phase transition was first observed [8], the creation of the MI state was

inferred by the gradual blurring of interference patterns caused by the increase in phase fluctuations between atoms at various lattice sites as the laser intensity was increased. Alternatively, this state can be observed by direct atom-number counting [61].

The Experimental Apparatus

This chapter records details of the experimental apparatus largely rebuilt at the end of the previous caesium experiment. This setup is different from other rubidium BEC experiments in the groups and these methods are therefore not described elsewhere.

3.1 The BEC Apparatus

3.1.1 Lasers

We have two external cavity diode lasers (Toptica DL100) operating at the D2 line of rubidium at wavelength of $\lambda = 780$ nm. The first, referred to as the Master laser, supplies the light we need for the cooling transitions in the pyramidal and science MOTs and for the probe and optical pumping light. The second laser generates the repumping light for both MOTs. The operation of a laser diode for spectroscopic applications demands a highly stable current control and an active control of the laser diode temperature (both at about $21.5^{\circ}C$). We use commercial plug-in control modules for the current (Toptica DCC 110) and for the temperature (Toptica DTC 110). In our lasers, the external cavity is formed by a reflection grating and the rear facet of the diode. The grating is mounted in the Littrow configuration, i.e. the first diffraction order of the grating is reflected back towards the diode. A diffraction-limited lens between the grating and the diode collimates

the light emitted from the front facet of the diode and focusses the back reflected first order light into the diode resonator. The zeroth-order reflection serves as the output beam providing around 50 mW of output power. In such a configuration the feedback of the grating is highly frequency-selective, hence it provides a convenient way to adjust the wavelength. The lasers have a line width of less than 1 MHz, which is several orders of magnitude smaller than that of a free-running laser diode. There is a piezo actuator integrated in the grating holder which allows changing the cavity length and hence tuning of the laser frequency over a range of a few GHz. We use the piezo actuator together with the current control to lock the lasers to the required frequencies.

Aim	Transition	Detuning (MHz)	Duration
Laser Cooling	$F=2 \longrightarrow F'=3$	-10	Until CMOT stage
Repumping	$F=1 \longrightarrow F'=2$	0	Throughout cooling processes
CMOT	$F=2 \longrightarrow F'=3$	0	2 ms
Molasses	$F=2 \longrightarrow F'=3$	-30	10 ms
Optical pumping	$F=2 \longrightarrow F'=2$	0	0.9 ms
Probing	$F=2 \longrightarrow F'=3$	0	0.2 ms

3.1.2 The optical table

The main optical table is divided into two sections: the lasers section and then the magnetic trap section. The laser section contains all the optics required to produce the light required for cooling, repumping, optical pumping and probing as shown in Figure 3.1. There are two other lasers on the bench to amplify frequency-stabilised light. They are the pyramid slave laser and the experimental MOT slave laser.

The shape of the output laser beams from both master and the repumper lasers are firstly changed from an elliptical shape to a circular shape using anamorphic prism pairs. These laser beams then travel through an optical isolator which prevents optical feedback back towards the lasers which would ruin their frequency stability. A small portion of the beam (typically much less than 1 mW) is then picked off to a saturated absorption spectroscopy setup for frequency locking the mechanism for which will be described in the next section. Using a half-wave plate and a

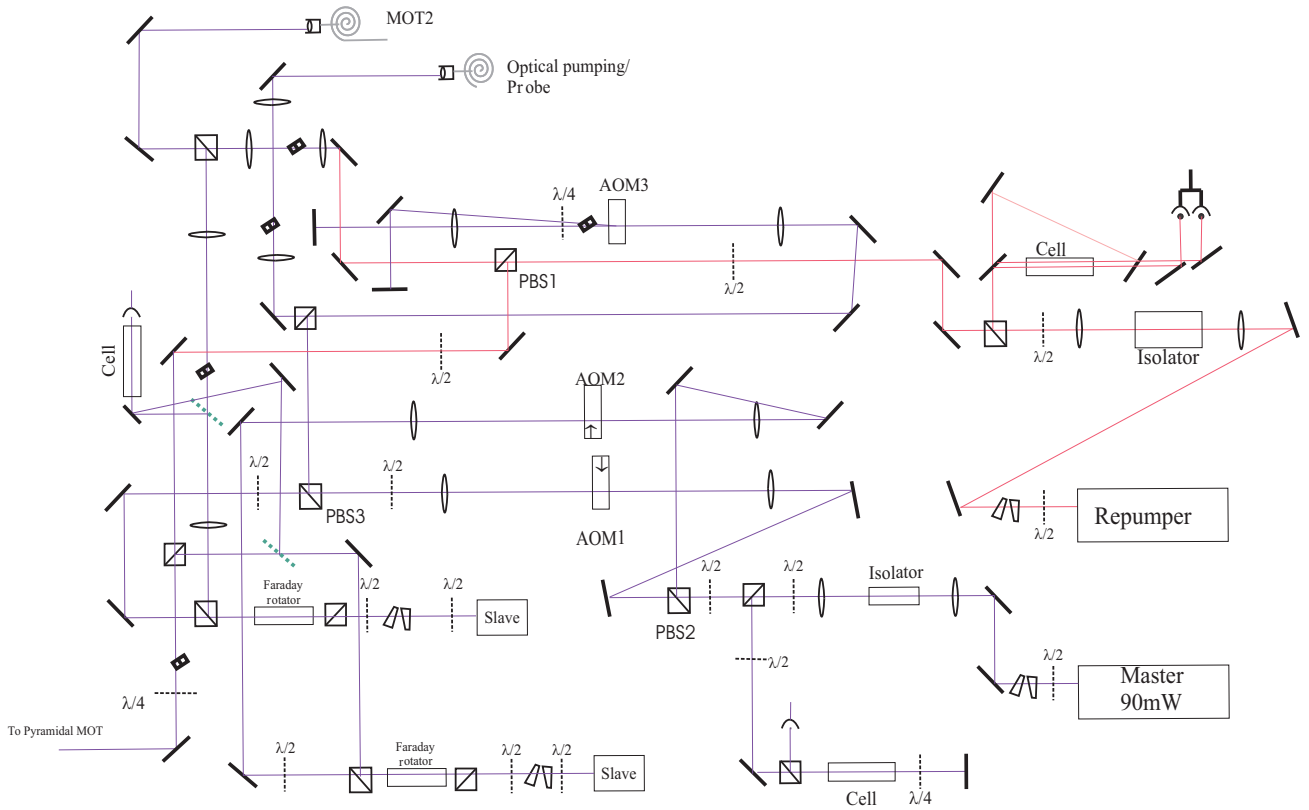


Figure 3.1: A plan of the laser section. This shows how the optics are laid out on the optical bench.

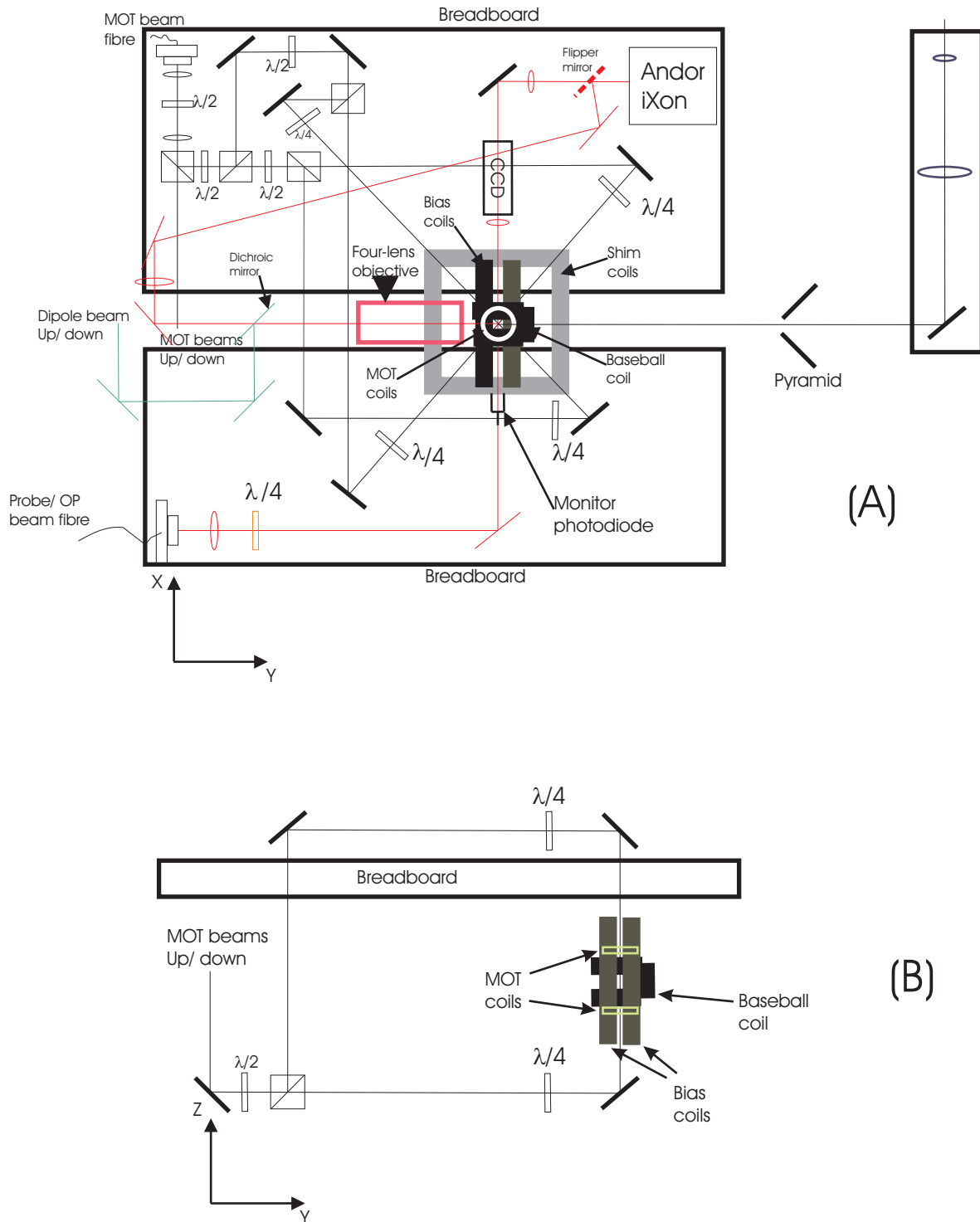


Figure 3.2: A schematic of the optics around the magnetic trap section. (A) view from above, (B) view from the side

polarising beamsplitter (PBS) cube, the beam is split into two different paths and the power of each beam is adjustable by rotating the half-wave plate. For the repumper laser, the beam is split at PBS1 (refer to Figure 3.1); one portion goes directly to the optical fibre for the experimental MOT while the other portion goes to the pyramidal MOT. For the light from the master laser however, the setup is slightly more complicated; the beam is split in two at PBS2 and both of these beams first pass through Acousto-Optic Modulators (AOMs) AOM1 and AOM2 which alter the frequency of the beams by an amount equal to the driving rf which we control externally with the help of a Voltage-Controlled Oscillator (VCO). The VCO control boxes output RF signals with frequencies with a range of 80-125 MHz. The frequency of these signals can be controlled by varying the analogue dc voltage input. These RF signals are then amplified via a 2 W amplifier (MINI-CIRCUITS ZHL-1-2W) before they pass onto the AOMs. The beam that passes through AOM2 injects the pyramid slave laser. The beam that passes AOM1 is further split at PBS3. One of these beams proceeds to inject the experimental MOT slave laser. The other goes to AOM3; the zeroth order beam out of this AOM (whose frequency is not shifted) is used for probing and the -1^{st} order beam is reflected back to the AOM to have its frequency altered a second time by the same amount i.e. a ‘double-pass’ configuration. The beam from this double-pass is sent into an optical fibre for probing and optical pumping where this beam overlaps with the probing beam. To monitor the injection of the slave lasers, we place flipping mirrors to pick off a small portion of the slave laser beams which travels through a Rb cell and then onto a photodiode. In this way, one can confirm injection by seeing that the absorption spectrum obtained with light from the injected lasers is similar to the original absorption spectrum obtained with light from the master laser.

The experiment is enclosed in a light-tight box to prevent room light from reaching the atoms. The arrangement of the optics around the magnetic trap is illustrated in Figure 3.2 and is quite a busy one. For convenience the description of this setup is divided into five sections: laser cooling, absorption imaging, fluorescence

imaging, dipole trapping and monitoring. For the laser cooling section, the cooling beam from the experimental MOT slave and the repumper laser begin at the optical fibre labelled ‘MOT beam fibre’. As required for laser cooling, the beam is initially magnified in size by a pair of lenses (telescope) after which it is split into six separate beams with polarising beam splitter cubes, half-wave plates and quarter-wave plates.

The absorption imaging system starts with the probe/ optical pumping optical fibre. The laser beam that exits this optical fibre travels directly through the cell and proceeds to the Andor iXon camera via a series of lenses for absorption imaging. There is also an arrangement for fluorescence imaging. The probing beam used for fluorescence imaging is the same as that used in absorption imaging but the setup also has a four-lens objective that serves the dual purpose of collecting light from the cloud for fluorescence imaging and also focusing the dipole trapping beam onto the cloud of atoms. Note that the fluorescence imaging axis is perpendicular to the absorption imaging axis. The fluorescence light is then focussed to the Andor camera with a lens of 1 metre focal length. The dipole trapping beam is also focussed via the four-lens objective and is reflected to the objective with a dichroic mirror which is highly reflective (given the right polarisation of the incoming beam) for our dipole trapping beam of $\lambda = 830$ nm and highly transmitting for $\lambda = 780$ nm. Finally, to monitor the cloud, we have a CCD camera (PULNiX video standard, monochrome) and a battery-operated photodiode (DET110). By checking the fluorescence signal every morning and also keeping an eye on the monitor screen linked to the CCD camera, any unusual features with the MOT loading rate or cloud shape will be noticed immediately.

3.1.3 Frequency stabilization

We use Doppler-free saturation spectroscopy to provide a reference frequency for locking the lasers. The frequency stabilization is performed by a fast feedback loop on the diode current, and a slow feedback loop on the voltage applied to the piezoelectric crystal (PZT). The voltage applied to the PZT is scanned to produce

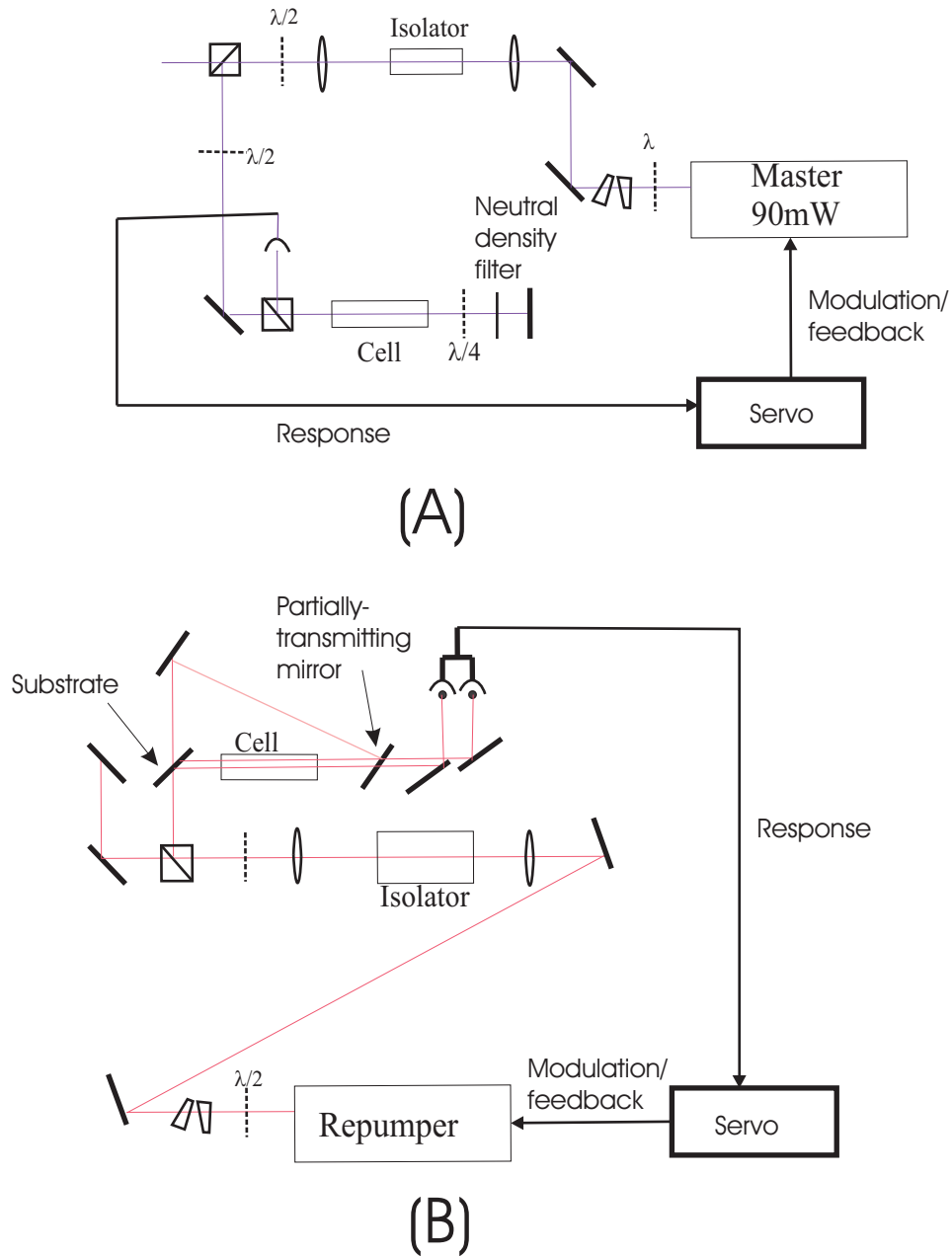


Figure 3.3: The optical arrangements for saturated absorption spectroscopy that are used for (A) Master laser and (B) Repumper laser.

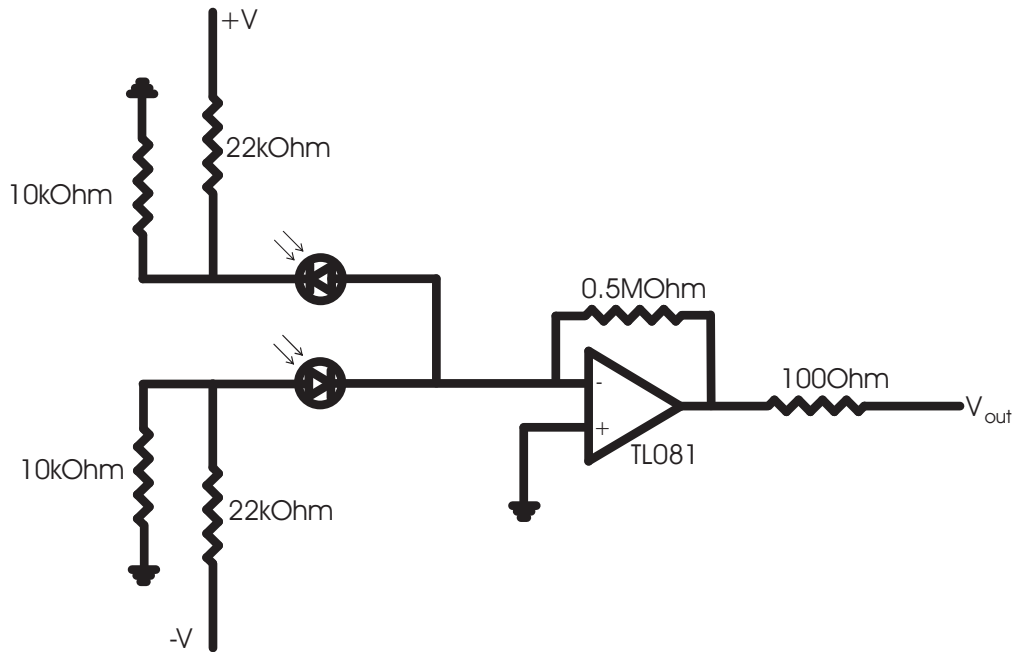


Figure 3.4: Diagram of the double photodiode (BPX65) circuit. The basic circuit is a current-to-voltage converter. The difference in the two photocurrents is converted into a voltage by the operational amplifier (TL081).

an absorption spectrum where we can see the atomic transitions. Figure 3.3 shows the layout for the absorption spectrum of both the master laser and the repumper laser and their frequency-lock setups.

In the absorption spectrum scheme for the master laser, a filter is attached to the quarter-wave plate to attenuate the power of the pump beam twice. This twice-attenuated beam then acts as the probe beam in the usual saturation absorption spectroscopy scheme.

The repumper transition is a rather weak one and therefore to obtain good signals, we used the arrangement as shown in 3.3 (B) where an initial beam passes through a substrate (uncoated mirror). About 90% power is transmitted and the remaining 10% is shared between two reflected beams from the front and back surface of the substrate. One of these reflected beams acts as a probe beam counter-propagating with the pump beam and the other as a reference beam. The beam that overlaps the pump beam will show the saturated absorption feature while the other has

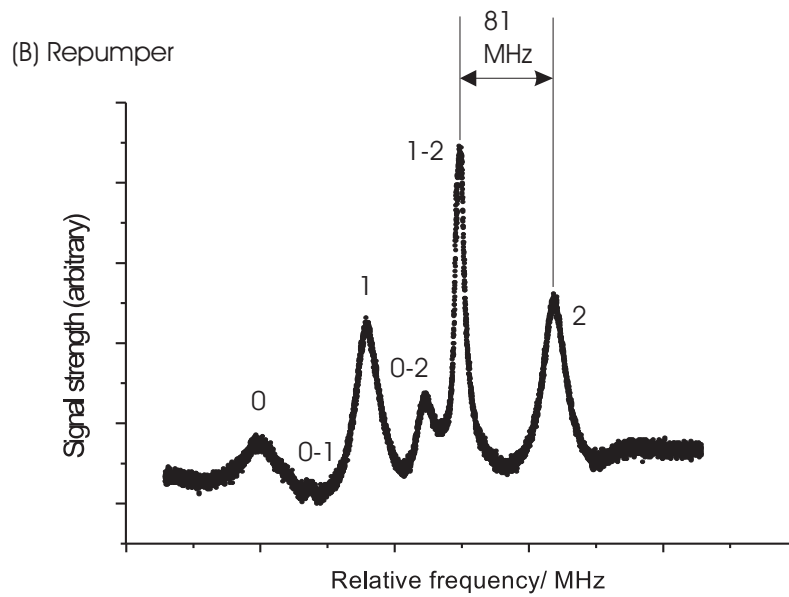
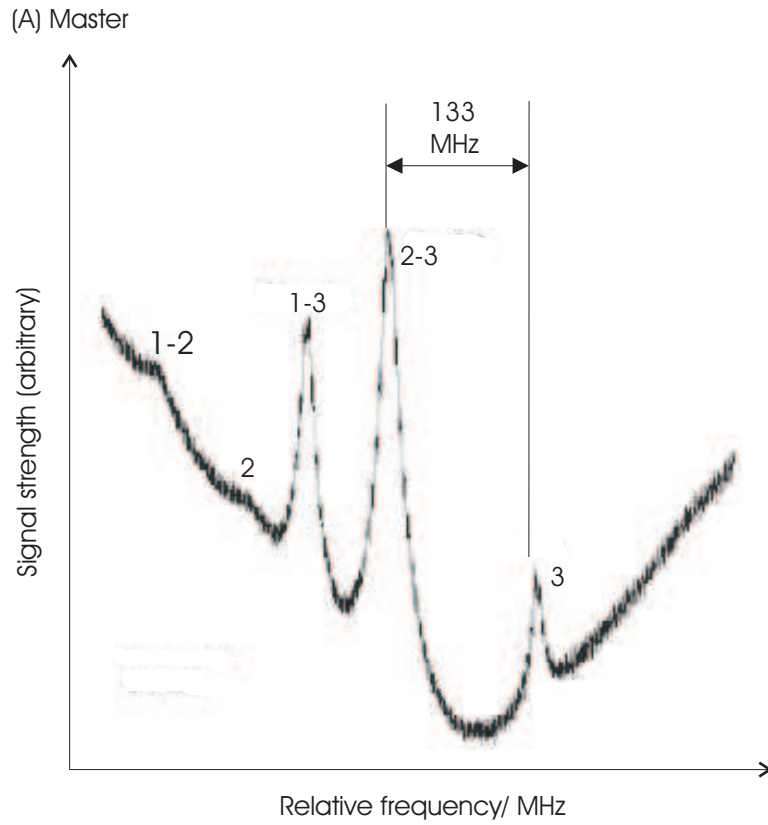


Figure 3.5: Doppler-free absorption spectroscopy. (A) Master laser, transitions start from $F=2$ ground state. "1-2" means the $F'=1$, $F'=2$ crossover. (B) Repumper laser, transitions start from $F=1$ ground state.

the Doppler-broadened profile. These beams pass through a partially-transmitting mirror to fall onto the double-photodiode in which the two photodiode signals are subtracted to remove the Doppler background resulting in only the transition peaks (Figure 3.5(B)). The layout of the double-photodiode circuit is shown in Figure 3.4. In addition to subtracting the Doppler profile to make the transitions more visible, we also heat the cell to about 37°C to increase the vapour pressure of rubidium.

We dither the current driving the diode lasers with a small amplitude to produce a small frequency modulation at 100 kHz. When the frequency of the laser is resonant with one of the absorption peaks, the frequency modulation produces an amplitude modulation on the photodiode signal. The servo electronics is used to generate an error signal from this modulation which is integrated and used as feedback for the diode current and the amplifier for the PZT. In the absence of external mechanical noise on the optical table, we can keep the lasers locked for an entire day at a time. The staff of the Electronics Workshop of the Physics Department designed and built both the lock-in electronics (EW 1225) and the piezo driver (EW 1145).

3.1.4 Vacuum system

The vacuum system shown in Figure 3.6 has two differential pumping stages.

In the first section of the vacuum system there is pyramidal MOT. It has a pressure of approximately 10^{-9} mbar maintained by a 40 l/s ion pump (Varian VacIon Plus 40). The rubidium source is several dispensers (SAES Getters) connected in series located just above the pyramid mirrors. A current is passed through the dispensers to heat them and the resulting chemical reaction releases the rubidium atoms. The dispenser is continuously operated at 3.2 A to provide ample Rb pressure in the pyramidal region.

Differential pumping is achieved by a hole (5mm diameter, 17mm long) in the back port of the pyramid chamber. The distance between the pyramidal MOT

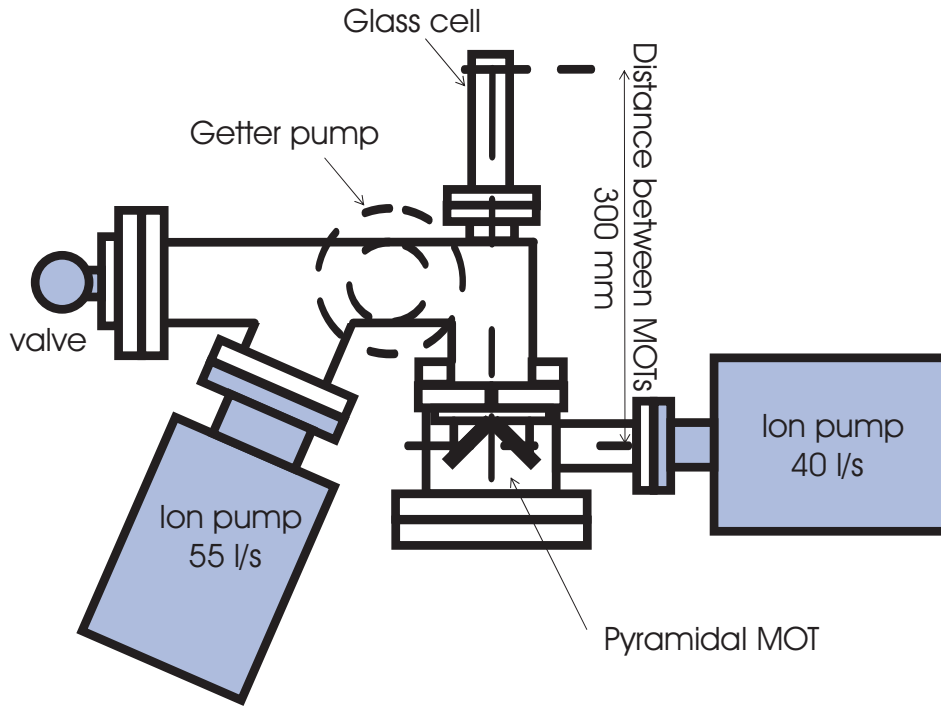


Figure 3.6: The vacuum system.

and the experimental MOT is 30 cm. This distance is short in order to reduce atom loss due to divergence of the atomic beam from the pyramidal MOT to the experimental MOT.

The ultra-high vacuum part of the vacuum system contains a rectangular quartz cell of dimensions $28 \times 28 \times 80\text{mm}^3$ (2mm wall thickness). Pressure in this region is maintained by a 55 l/s ion pump (Varian VacIon Plus 55) and a non-evaporable getter (NEG) pump (SAES CapaciTorr-CF35, Cartridge C-400-DSK-St172). The NEG pump establishes ultra-high vacuum by pumping away hydrogen which is the dominant residual gas in a clean vacuum system.

3.1.5 Pyramidal MOT

The purpose of the pyramidal MOT [62] is to collect atoms from a vapour of rubidium. The atoms are transferred continuously through the differential pumping hole into an ultra-high vacuum region, where our final experiments are performed. Our pyramid (Figure 3.7) is larger than the one described in [63]. This is an im-

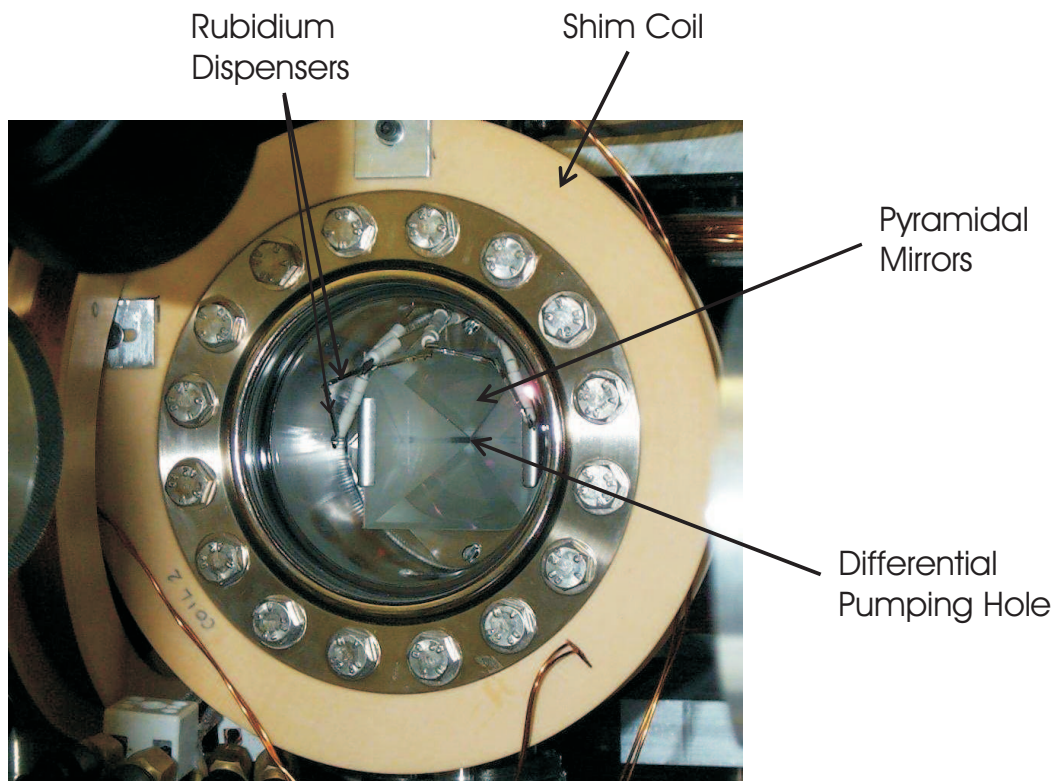


Figure 3.7: A photo of the pyramid.

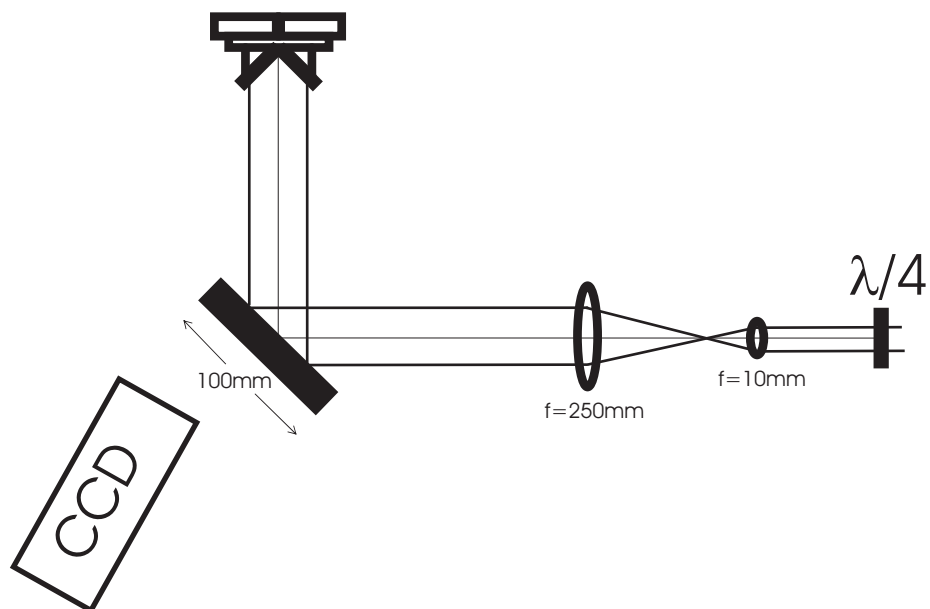


Figure 3.8: A diagram of the optical setup of the pyramidal MOT.

provement as an increase in the size of the pyramidal mirrors increases the volume of the collection region, which results in a higher flux atomic beam.

The optical setup for the pyramidal MOT apparatus is shown in Figure 3.8. The large mirror (diameter = 100mm) and the pyramidal mirrors (base length = 60mm) are coated by Mr C. Goodwin in the Oxford Physics Department. The mirror and pyramid optics are coated to achieve the same reflectivity for s- and p-polarization. (Non-equal reflectivity of s- and p-polarised light would cause a phase shift between the two polarizations and therefore the light would no longer be circularly polarized after reflection.)

The laser beams travelling towards the pyramidal setup consist of the cooling beam from the pyramid slave laser and some beam coming from the repumper laser. For the cooling beam, we begin with a measured beam waist of about $440 \mu\text{m}$ ($\frac{1}{e}$ half-width). With a combination of lenses with focal lengths $f=10 \text{ mm}$ and $f=250 \text{ mm}$, the beam is magnified and collimated after which it travels to the pyramidal mirrors. The large beam has a waist size of 11.8 mm ($\frac{1}{e}$ half-width) and contain 44 mW of cooling beam power and 6 mW of repumper beam power. We do not use an optical fibre for this setup but this did cause some inconvenience; due to the long path length from the laser to the pyramidal mirror, any slight changes in the angle of the grating of the ECDL causes a deviation in the incident position of the beam on the pyramidal mirrors. This led to a change in the loading performance of the pyramid and meant that it was necessary to adjust the large pyramid mirror occasionally. Fortunately, these changes are minor. It is useful to monitor the pyramidal MOT using an infrared CCD camera.

Two sets of coils are required for generation of the magnetic fields required: a pair of anti-Helmholtz quadrupole coils (pyramid coils), and three shim coils (pyramid shim coils) positioned in orthogonal directions. The anti-Helmholtz coils provide the field gradient required for trapping of the atoms. They have 15 turns of 3mm outer diameter 22 swg (corresponding to an inner diameter of approximately 1.5mm) annealed copper tubing. Water is passed through the copper tubing to

provide cooling. The radius of the coils is 56mm and their separation is 50 mm. To load the atoms 28A is run through the coils producing an axial field gradient of 14 G/cm. The total resistance of the pyramid quadrupole coils (in series) and the connecting cables is approximately 0.08Ω .

The shim coils are circular coils, inner diameter of approximately 150 mm, wound with 100 turns of 1 mm enamelled copper wire. These shim coils serve two purposes: firstly to counteract any ambient magnetic fields (e.g. earth's magnetic field), and secondly to move the centre of the magnetic field produced by the quadrupole coils for diagnostic purposes. At optimal loading rate of atoms in the second MOT, the centre of the pyramidal MOT is normally directly over the pyramid hole and therefore no (or very little) fluorescence is observed. To accurately determine the number of atoms in the pyramid it is necessary to move the centre of the MOT to a position where the fluorescence light can be measured. The shim coils were used only initially to measure fluorescence signal. These shim coils have not been used since.

3.1.6 2nd MOT - experimental MOT

For this experiment our 2nd MOT is a conventional six-beam MOT [28]. The MOT pair of anti-Helmholtz coils (quadrupole coils) are circular coils of diameter 42mm separated by a distance of 78 mm. Each coil is made out of 130 turns of 0.7 mm enamelled copper wire. The MOT coils are wound around a copper mount which has a gap in it to suppress eddy currents. The MOT coils are also water-cooled via a single turn of copper pipe soldered to the copper mount. The coils are positioned as close as possible to the trapping region to maximise the magnetic field gradient for a given current. During loading of the experimental MOT a current of 2 A runs through the quadrupole coils, generating an axial field gradient of 10 Gcm^{-1} . The current through the coils is controlled by a circuit that uses Field-Effect Transistors (FETs). Varying the gate voltage input into the FET circuit controls the amount of current through the coils. The voltage applied to the gate of the FETs comes from the output of a multiplexer unit which requires

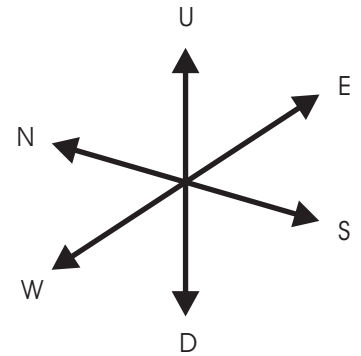
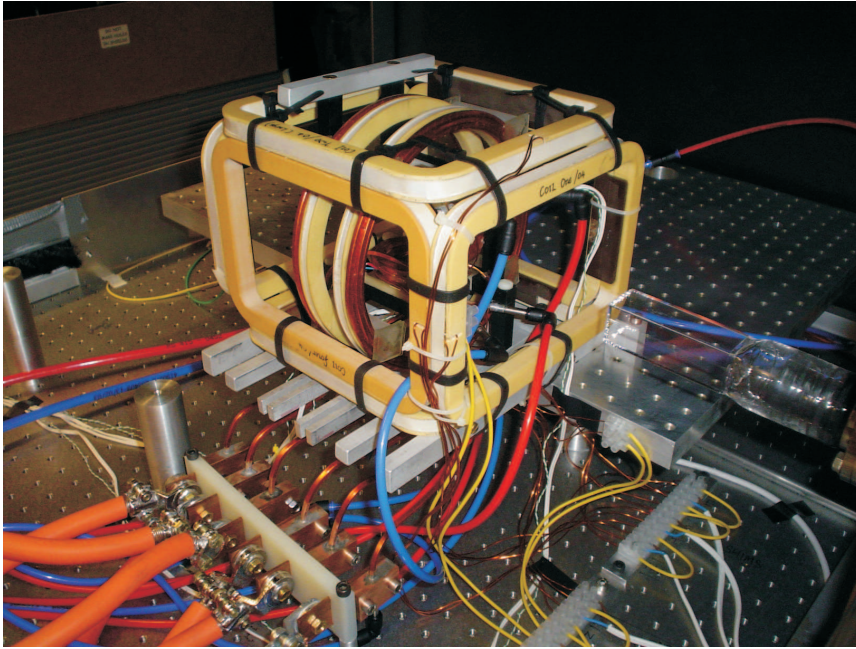


Figure 3.9: A picture of the experimental MOT and the magnetic trap together with the pipes required for water cooling of the coils. All components of the trap in this picture were mounted by Martin Shotter. The baseball and bias coils terminate in a series of copper blocks which are mounted with a Teflon support under the main optical breadboard. This enables both the current and water to be fed through the coils in a convenient way. Rubber-coated welding cable is used to connect the coils to the MOSFET banks and supplies.

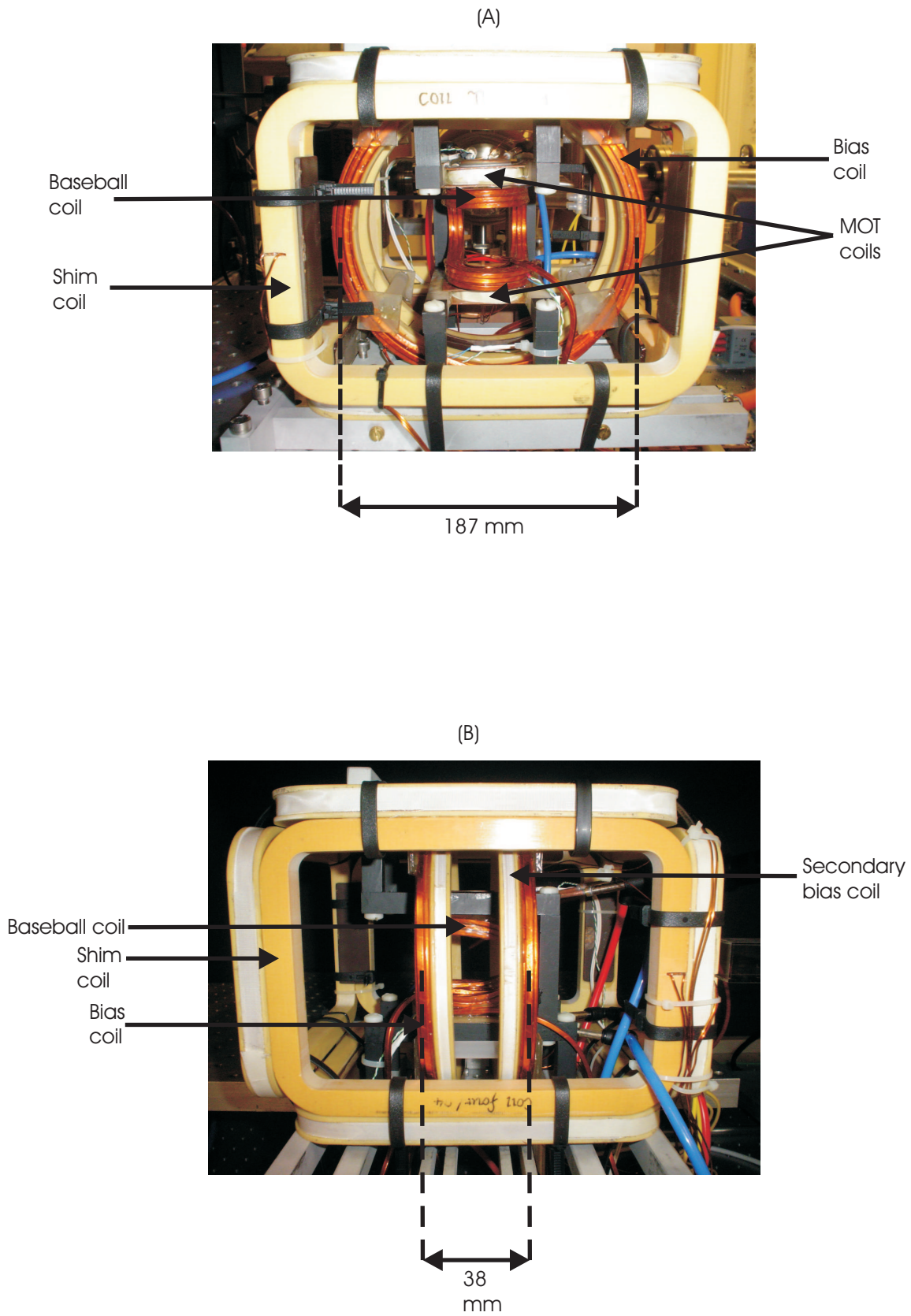


Figure 3.10: Pictures of the experimental MOT from the side.

Transistor-Transistor Logic (TTL) inputs. Figures 3.9 and 3.10 are pictures of our experimental MOT from various orientations.

Shim coils	No. of turns	Dimensions (mm)	Separation (mm)
E/W	67	196×138	226
N/S	68	196×138	192
U/D	68 (up); 67 (down)	196×196	167

Shim coils are required to null out any ambient magnetic fields, which is especially vital for the optical molasses stage. They also move the centre of the MOT for loading into the magnetic trap in the CMOT stage. The shim coils are six coils mounted in a cuboid arrangement wound with 1 mm diameter wire. They are labelled the U/D shims, E/W shims and N/S shims (specifications given in the table above). All the shim coils were wound by Tony Hickman in the Clarendon Laboratory. Since all the coils are rather bulky, the separation is defined by the distance between the centres of the coil units. Like the MOT coils, the current through the shim coils is controlled by a FET and the gate voltage for the FET is provided by the multiplexer circuit. For every pair of shim coils, a maximum of 5 Amperes can flow through the wire to give a maximum field of 10 Gauss at the centre of the geometry. In addition to nulling the magnetic field of the earth for the molasses stage, the E/W shim coils are also used to provide a field that defines the quantization axis for optical pumping and probing.

3.1.7 Magnetic trap

Construction

The baseball magnetic trap used in the experiment is a type of Ioffe-Pritchard trap and it needs to fulfill certain geometry requirements to give confinement in all three dimensions. The geometry of our baseball trap was modelled on that of the previous baseball trap used in caesium experiments now taken to Durham University by Simon Cornish. To calculate the fields in this trap, we simulated the magnetic trapping potential using MATHEMATICA and the Biot-Savart law. We wound the coils as close as possible to the vacuum chamber to provide the

tightest trapping frequencies possible with the space constraints of our system. In addition, a pair of Helmholtz coils (primary bias coils) were added to generate a nearly uniform magnetic field that opposes the field from the baseball coil at the centre. Given a certain magnetic field from the baseball trap alone, increasing the field strength generated by the primary bias coils allows modification of the trapping geometry. The entire setup was designed such that when this happens, the resulting trap confines more tightly in the radial direction while the axial confinement is unaffected. To fine-tune the overall bias field at the centre of the trap, we also have another set of coils (secondary bias coils) attached to the primary bias coils. Like the MOT coils and the shim coils, the current through the secondary bias coils is controlled by a FET and the gate voltage for the FET is provided by a multiplexer circuit. This FET is in a 5 Amps current source unit EW1284 designed and built by members of the Central Electronics Workshop, Physics Department, University of Oxford. We can run a maximum of 5 Amperes through the coil providing a cancellation field of up to about 30 Gauss. Pictures of our baseball trap, primary bias coils and secondary bias coils are shown in figures 3.9 and 3.10.

The baseball coil was constructed using copper tubing of a square cross-section with sides of 3.5 mm wound with Capton tape that encases the tubing for insulation. The bias coils are also constructed out of copper tubing of square cross-section but with sides of about 4 mm, also insulated with Capton tape. The baseball coil consists of 9 turns with four straight sections and four semi-circular sections, the straight sections being of 26 mm simulated length and the semi-circular sections being of 28 mm simulated radius. These are all approximate since by the time the coil is wound, it is rather bulky and the dimensions are more difficult to define. The primary bias coils have 5 turns and are designed to have a diameter of 187 mm with a separation of 38 mm between them. The secondary bias coils are wound with 1 mm diameter copper wire, consist of 44 turns, have an effective diameter of 190 mm and are separated by a distance of 57 mm. The secondary bias coils were wound by Tony Hickman of the Clarendon Laboratory, Physics Department, University of Oxford.

During the winding, all the voids between the layers of copper tubing were filled with epoxy to improve mechanical stability. While running the experiment, the current through the coils causes heating which can lead to expansion of the coils and hence cause the trap frequency and position to change. To minimise this the bias coils have a quartz spacer glued between them. Quartz has a low thermal expansion coefficient and so this preserves the bias coil spacing as much as possible. The quartz spacers were attached to the primary bias coils with a small section of quartz plate. Epoxy was used to glue the quartz to the coils.

Finally, the baseball coil and the primary bias coils have a hollow circular cross-section to allow for water-cooling of the coils. With the water turned on but no current through the coils, the coils reach an equilibrium temperature of about 19°C. With a current of 200 Amperes, the coils heat up to an equilibrium temperature of about 26°C in a few seconds. After turning off the current, the coil temperature falls back down to 19°C again after a few seconds.

High current control circuits

To load the atoms into the trap in a way that preserves the number and the phase space density of atoms transferred (mode matching), the magnetic trap is initially weak. After loading, the trap frequency is increased adiabatically to a high value suitable for evaporation to promote efficient rethermalisation. To achieve this, the baseball coil is switched on at 200 Amps initially and afterwards is ramped up to adiabatically tighten the radial confinement of the magnetic trap.

To have good cancellation of the baseball field at the trap centre using the bias field, we require excellent control of the magnitude of both of these fields. The two fields of over 100 Gauss each must cancel to within one Gauss, and the trap frequency is very sensitive to the level of the residual field. This means that small fluctuations in the current in the baseball or bias coils (primary or secondary) would lead to substantial heating. This heating is minimised by wiring the baseball and bias coils in series so that any fluctuations in the current are common to both sets of

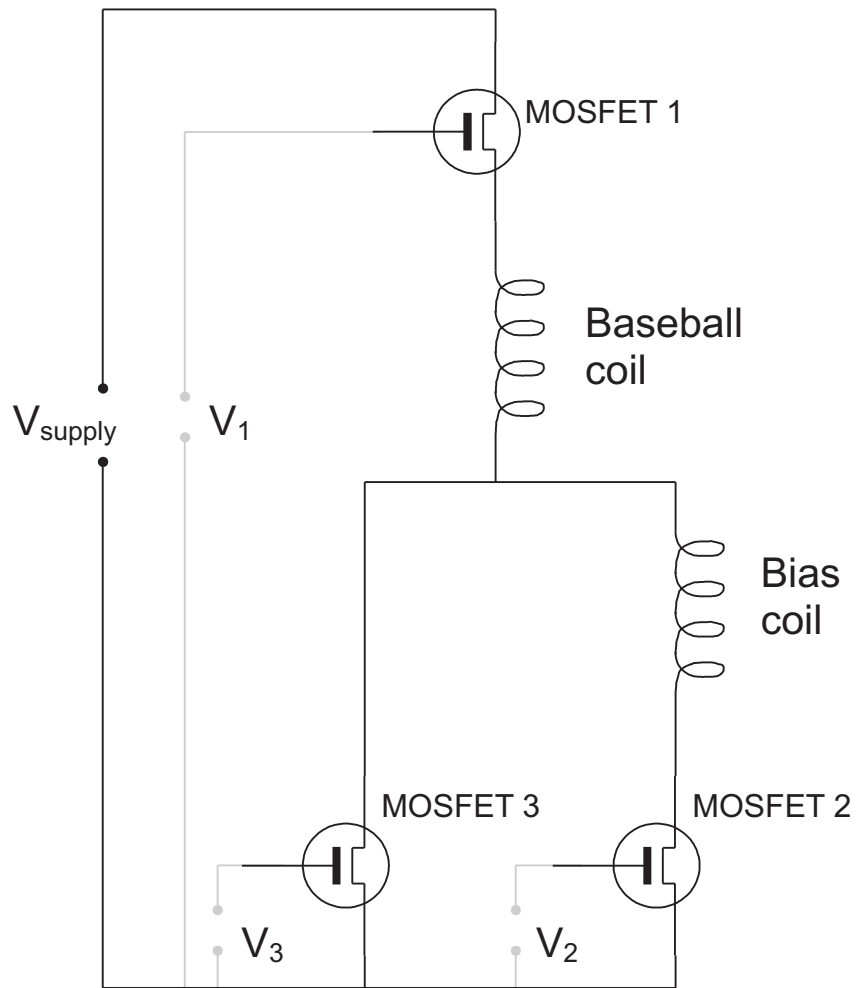


Figure 3.11: High current electrical connection.

coils. Figure 3.11 shows the electronics for control of the high current. The three Metal Oxide Semiconductor Field-Effect Transistor (MOSFET) banks are labelled MOSFET 1, MOSFET 2 and MOSFET 3. These MOSFETs work on the same principle as FETs but we decided to use them to control higher currents. MOSFET 1 controls the overall current running through the entire setup, MOSFET 2 controls the current through the path of the bias coil and MOSFET 3 controls the current running through the bypass path. At the beginning of the experiment, MOSFET 1 is completely closed allowing 200 A of current to run through the baseball coil. MOSFET 2 is either completely closed (when the experiment is run) or completely open (at the end of the experiment or when it is not running). We control the amount of current running through the bias coils by varying the gate voltage V_3 of MOSFET 3. For most of the experiment, V_1 and V_2 are constant. We change the trapping geometry by changing V_3 .

In practice each MOSFET bank has 5 MOSFETs (STMicroelectronics STE180NE10) connected in parallel and all linked to the same control voltage. Each MOSFET has a current rating of 180 A and having five of them in each bank means each bank is capable of taking in 900 A of current, well above what we need. The MOSFETs dissipate a considerable amount of heat and so are mounted on a copper tube which is water cooled.

Current control electronics

In the following section, all signal names in inverted commas refer to the corresponding input/output in Figure 3.12.

The magnetic trap current is controlled by two pairs of electronic circuits; a ‘Reference Voltage Board’ and ‘Main Feedback Board’ (see Figure 3.12). The ‘Reference Voltage Board’ controls the trap turn on/off (and fast input control etc) and generates the input voltage for the ‘Main Feedback Board’. The ‘Main Feedback Board’ provides the gate voltage for the FET’s and the integrator part of the circuit regulates the current through the baseball and bias coils. The ‘Trap on/off TTL’ is

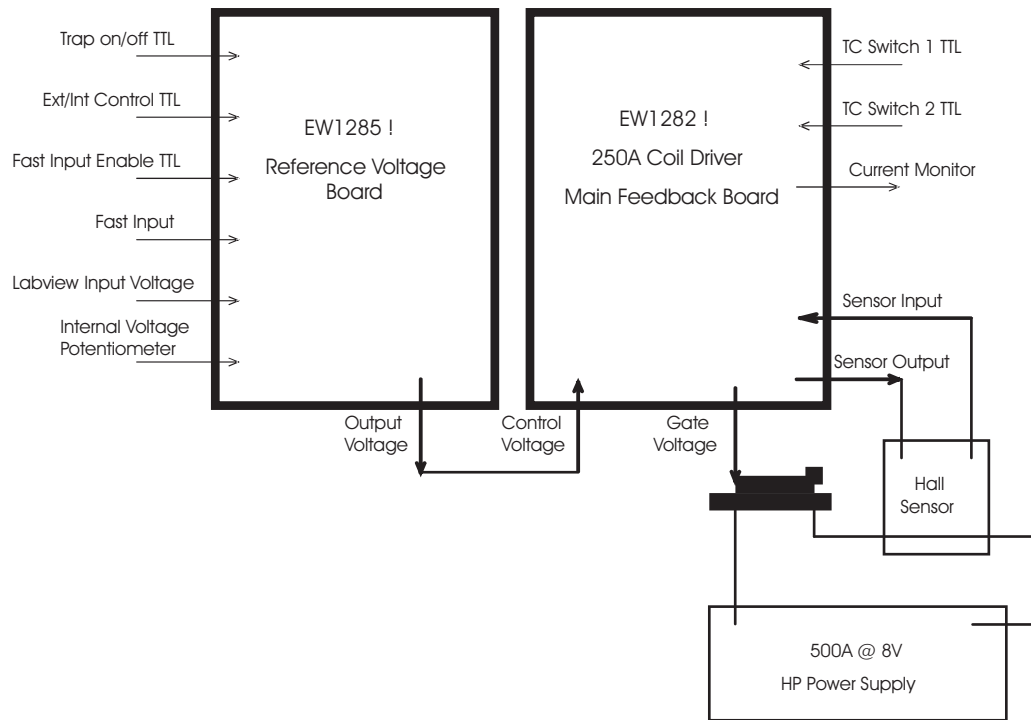


Figure 3.12: A schematic illustrating the setup of the magnetic trap current control electronics. To control the current in both the bypass and baseball coils two pairs of the above boards are required. There is a third pair for the bias although this is mainly used as a switch.

controlled by a TTL signal. When it is set to high, the trap turns on to a level set by the analogue ‘LabVIEW Input Voltage’. For a rapid turn on the trap is initially turned on without involving the feedback circuit in EW1282. The capacitors are then switched back into the circuit to improve DC stability. For fast current control the fast input facility can be used. The ‘Fast Input Enable TTL’ requires a TTL signal in order to switch an extra reference voltage into the circuit. The extra reference voltage is an analogue voltage applied to the ‘Fast Input’, and is then summed into the circuit. This facility is required as the analogue input from Labview is filtered (the ‘fast input’ is summed into the circuit after the filter) and therefore fast current changes cannot be implemented.

For current stabilization and monitoring the welding cable (50 mm² cross sectional area) is passed through two closed loop current sensors (Honeywell CSNJ481) for the baseball coil and the bypass welding cable. The current loop sensor consists of a coil of 2000 turns wound around a ferrite core which circles the welding cable. The Hall sensor maintains a condition of zero magnetic flux through the core by balancing the current in the 2000 turn coil to cancel that from the cable. This current is the output of the sensor and goes to the control electronics boards where it is converted to an input voltage via a shunt resistor. This input is part of a feedback mechanism in the ‘Main Feedback Board’ which generates and controls the current in the Hall sensor. The ‘Current Monitor’ outputs for the baseball coil and the bypass are plugged into a digital oscilloscope and this signal we monitor everyday when running the experiment so any unusual behaviour would show immediately. To check the stability of the high current, the ‘Current Monitor’ outputs are connected to a 6 d.p. precision DVM (Agilent 34401A - 6 1/2 Digit Multimeter) where field fluctuations as small as a few mG can be observed. We ran the experiment several times (the duration of each is about five minutes) and we found that the variation of the current is comparable to the documented measurement error of the DVM itself. From this we conclude that the current is sufficiently stable and that the boards are functioning well. In normal operating conditions, the baseball coil current is turned on to 200 A in about 1 ms and switches off even faster.

Safety features

Safety measures were installed in the experiment to prevent the coils getting too hot. K-type thermocouples were embedded in the baseball coil and one bias coil, and on the surface of one MOT coil. These allow the temperature of the coils to be read either directly with a thermocouple reader, or by interfacing to the computer. The LabVIEW program that controls the experiment was then programmed such that the experiment will not run if the temperature of any of the coils is higher than 30°C . In addition to that, alongside the thermocouples on these three coils, thermistors were also placed. These are linked to a temperature interlock box in which thermostat circuits (Cebek I-8) trip a relay when the temperature of the thermistors rises above a certain value. The trip temperature of the circuit is set around 55°C .

3.1.8 Evaporation

The radio-frequencies required for evaporation were generated by a synthesized function generator (Stanford DS345). The generator is capable of frequencies from DC to 30 MHz and an amplitude up to a maximum of $10 V_{pp}$ (or 24 dBm) and the signal generated is transmitted to the atoms via a two-turn coil. For impedance matching between the load and the source, an effective 50Ω resistor was placed in series with the coil and this effective 50Ω resistor was made by connecting three 150Ω resistors in parallel. Each of these resistors has a power rating of 2 Watts which means having three of these in parallel can take up to a maximum RF power of 6 Watts. The evaporation ramps were calculated in Labview and then transferred continuously to the frequency generator via the GPIB interface.

3.2 Dipole trap apparatus

This section describes the additional apparatus required for the experiments we plan to do with the BEC. Parts of this section are based on reports of undergraduate students Peter Baranowski and James Zacks who worked towards building some

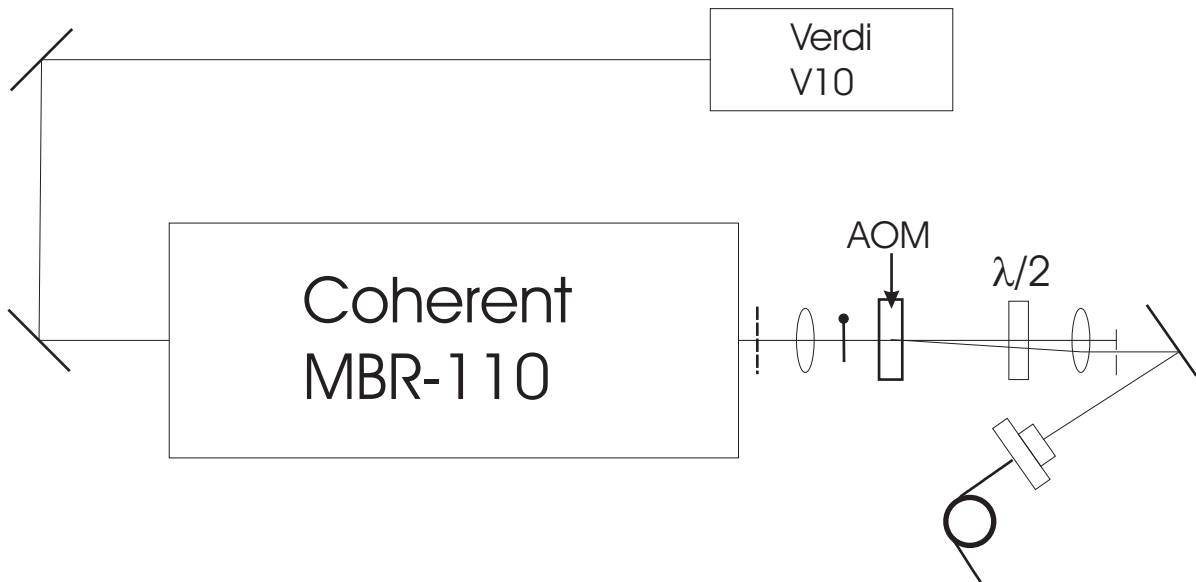


Figure 3.13: The laser system for dipole trapping.

components of the apparatus in our laboratory [64]. Where applicable, figures will be referenced.

3.2.1 Lasers

Figure 3.13 shows the arrangement of the apparatus that generates the dipole trapping beam. The Verdi V10 laser outputs a 532nm wavelength beam with a maximum possible power of 10 Watts. The Verdi laser pumps a Coherent MBR-110 Titanium-doped Sapphire laser that can be tuned between wavelengths 750 nm and 900 nm; we use a fixed wavelength of 830 nm at which a maximum output power of 900 mW is available for our dipole trapping experiments.

Immediately after the Ti:Sapphire laser, we have a green filter which removes most of the residue Verdi beam which comes through. After that, a lens of 10 cm focal length focuses the light into an AOM (Crystal Technology 3080-122) which controls the output beam power passing onto the rest of the system. Immediately after the AOM, we have a variable wave-plate in the form of a Babinet-Soleil Compensator tuned to be a half-wave plate for our beam wavelength and a 25 cm focal length lens to collimate the light. The beam then enters a polarisation-preserving

fibre (OZ optics LPC-02-830-5/125/P-2.4.11AS-40-1A-3-5+LPC-08-830-5/125-P-6.6-30AGR-40-1A-3-5) which acts as a good spatial filter. The pigtail collimator which the dipole trapping beam leaves through consists of a diffraction limited gradient index (grin) lens with a focal length of 30 mm. This gives a $1/e$ -diameter of the collimated beam of ≈ 3.9 mm.

3.2.2 Acousto-Optic Deflector

The AOD is an ISOMET LS110A-830XY Dual Axis AO Deflector with two single axis TeO₂ deflectors orthogonally mounted. The deflectors work by diffracting the light on acoustic waves generated in the crystal through the application of radio frequencies. The centre frequency for this AOD is 50 MHz and it has a bandwidth of 25 MHz, which gives a scan angle of 1.9° per axis. As shown in Figure 3.15 (A), the optical axis is defined as the diffracted beam at central frequency $\nu_{centre}=50$ MHz. Two telescopic stages shown in Figure 3.15 (B) are placed between the AOD and the four-lens objective to increase the beam diameter. This is so that we can achieve a tighter spot size after focussing which results in a tighter dipole trap. These telescopic stages achieve a magnification of $m = \frac{f_2 \cdot f_4}{f_1 \cdot f_3} = 3.75$. The scanning angle is therefore demagnified by the same factor.

The beam diameter needs to be increased and the beams have to be as collimated as possible after the last stage. This is done by choosing appropriate lens pairs and setting the distance between each two lenses that form a telescope to the sum of their focal lengths. Also, the deflector output aperture and the first focal plane of the focusing objective have to be conjugate points. This is achieved by setting the lenses up as shown in Figure 3.15 (B). Therefore the distance between the deflector and the 4-lens objective is fixed to 3.8 m. Finally, the aberrations introduced by the telescopes need to be small so we chose lenses with large focal lengths. Figure 3.16 shows the temporary configuration of the electronics we used to manipulate the dipole beam. In the near future we hope to replace this by a more robust system.

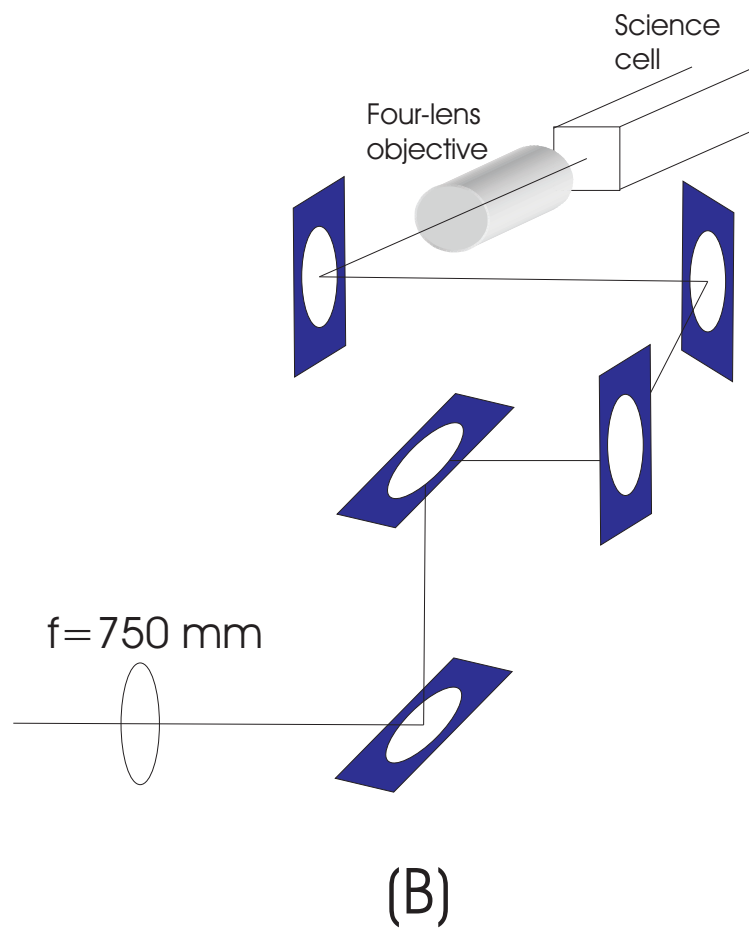
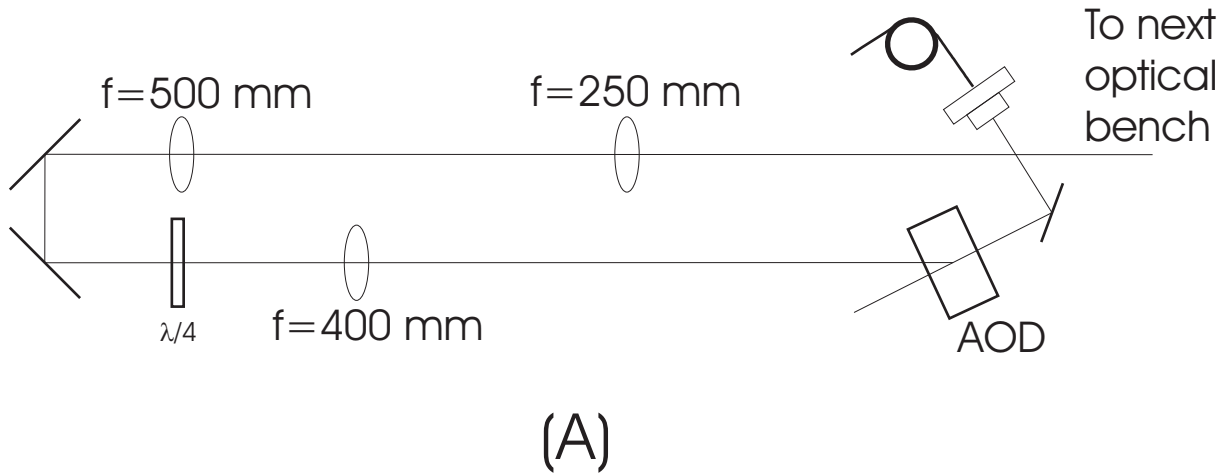


Figure 3.14: The optics around the Acousto-Optic Deflector (AOD). (A) shows the components on the same optical bench as the apparatus shown in Figure 3.1. (B) shows how the dipole trapping beam is elevated to the MOT using a periscope before reflecting from more mirrors to get to the vacuum cell. The $\lambda/4$ plate after the AOD is to convert circularly-polarised diffracted light off the AOD back to linearly polarised light.

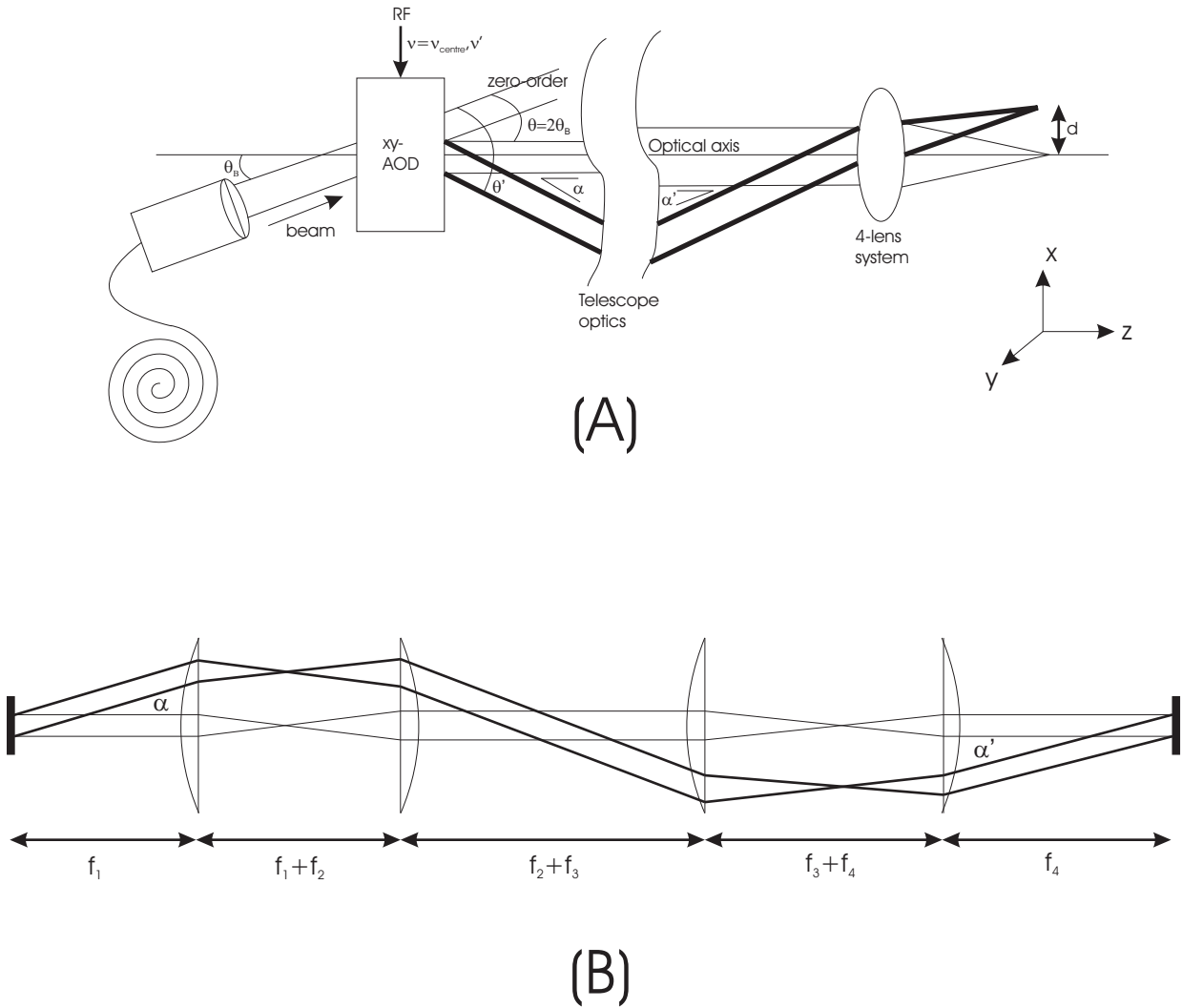


Figure 3.15: (A) Illustration of the principle of the lattice construction in one dimension for two radio frequencies: the centre frequency ν_{centre} and a second frequency ν' . The angle between the two first order beams is $\alpha = \theta' - \theta$. Through telescoping optics α is demagnified to α' before the beams are focused down to two small spots at distance d . (B) Telescope optics set up with 2-inch lenses between deflector (left) and 4-lens objective (right). $f_1 = 400\text{mm}$, $f_2 = 500\text{mm}$, $f_3 = 250\text{mm}$, $f_4 = 750\text{mm}$.

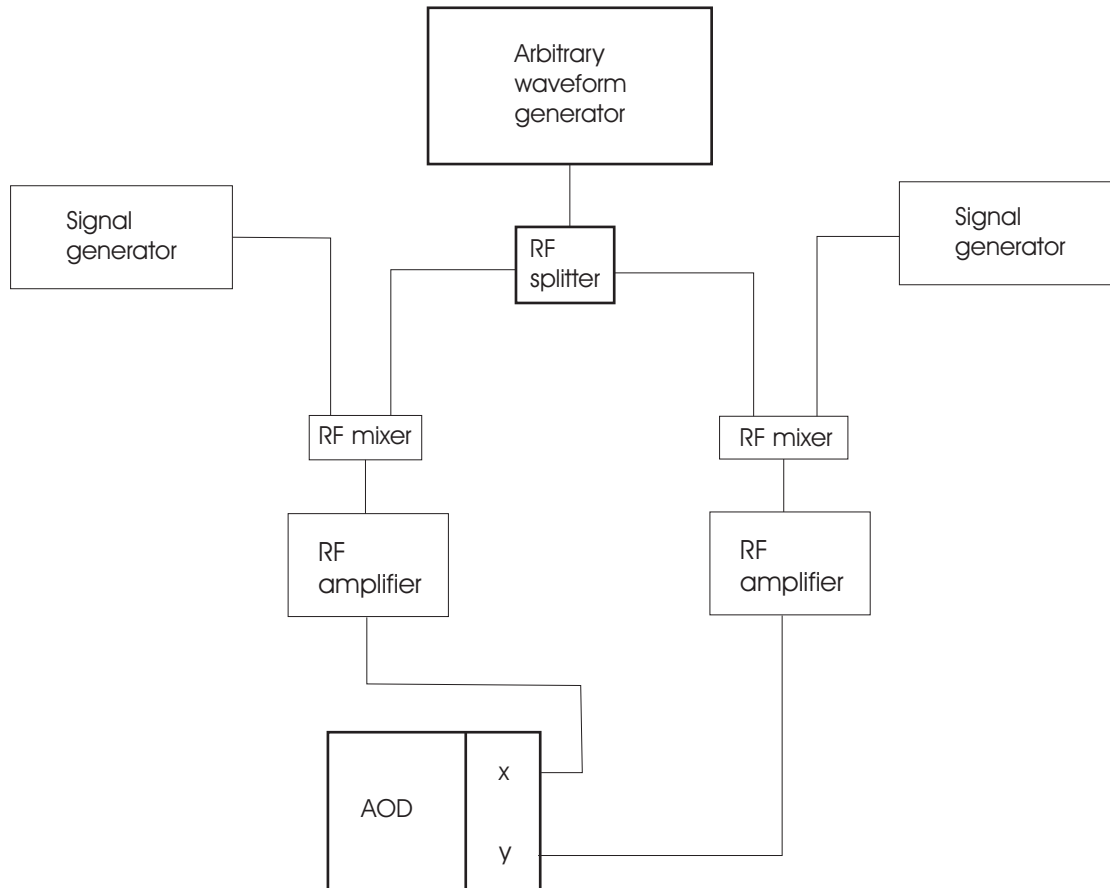


Figure 3.16: Temporary schematic for the electronics required for beam spot manipulation. The arbitrary waveform generator was a HP8770A AWG. The signal generators were Agilent 33220A and the RF splitters were MINICIRCUITS ZFSC-2-1W. The amplifiers were MINICIRCUITS ZHL-1-2W and the RF mixers were HP 10534A.

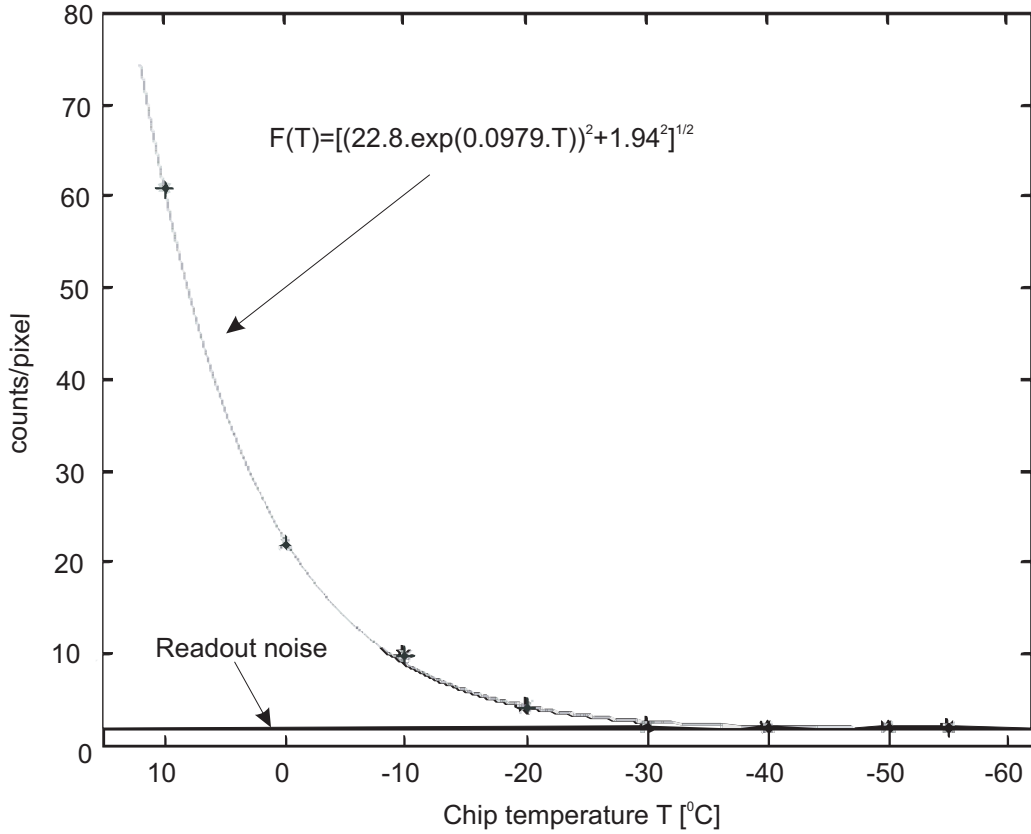


Figure 3.17: Measurement of rms-noise in absence of a signal (closed shutter) and fitting function $f^2(T) = (\text{darksignal}(t, T))^2 + (\text{readout})^2$. t is the exposure time and in this case $t = 10\text{s}$. Data taken by Peter Baranowski.

3.2.3 CCD Camera

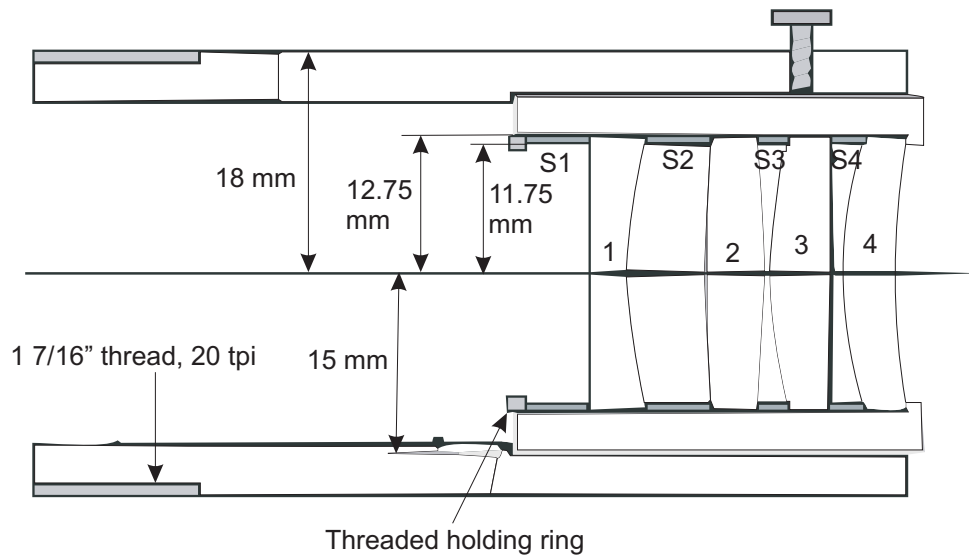
One of the aims of this experiment is to confirm the number-squeezed state of BEC by the direct counting of atoms. Since we will eventually be dealing with 100 atoms or less per dipole trap site, we will need a very sensitive detector to measure such weak signals.

To achieve the high sensitivity needed, a state-of-the-art frame transfer CCD camera with on-chip electron multiplying feature was acquired (Andor iXon DV887). The camera was tested mainly in the context of the examination of our 4-lens objective which will be discussed in the next section. The quantum efficiency (QE) for the $\lambda = 780\text{ nm}$ fluorescence light is ≈ 0.44 . The chip can be cooled to -90°C using a combination of thermoelectric and water cooling. Without using water (which

is the case for us currently) we can cool the chip to -55°C . For the comparatively short exposure times we use, shot noise caused by dark signal is not significant. If the chip is kept at 0°C the dark current is on average 2.1 counts/(pixel·s). At -55°C the average is reduced to 0.0066 counts/(pixel·s) which is sufficiently small compared to the readout noise (Figure 3.17). The readout noise, however, can be virtually eliminated because of the on-chip electron multiplication. Thus, the main contributions to the remaining noise are the shot noise from the signal and background light. To shield the camera from any light other than the fluorescence of the atoms, we use an array of two to three very narrow interference filters (Comar 780 IH 12). The filters are mounted in such a way that they can be directly attached to the aperture of the camera. In addition, they can be slightly tilted w.r.t. each other in order to prevent image artifacts caused by reflections between the filter surfaces. The transmittance was measured for both, light at the fluorescence wavelength and for light at the trapping beam wavelength as well as for tilts w.r.t. to the incident beam. The rms-transmittance for one filter at 780 nm is 81.8 % and 1.6×10^{-3} % for 830 nm. If we consider a scenario in which 0.1 % of 10 mW trapping light reaches the detector by accident, using two filters in an array would cut down the unwanted photon flux to 0.04 photons/(pixel·s) while the transmission for the fluorescence signal will still be at 67 %.

3.2.4 Four-lens objective

One of the most important components of this experiment is the four-lens objective which will be used for both collimating the fluorescence light emitted by the atoms at 780 nm wavelength and also for focussing the dipole trapping beam light at 830 nm wavelength. This work was inspired by the work done in [65] which have been used in [66]. While this work was done with 852 nm wavelength of light, we have used the same lens combination but changed the inter-lens separations with the help of ray tracing software OSLO LT and ZEMAX to suppress aberrations with 780 nm light. In this way, we hope to achieve maximum resolution when the time comes to use this objective for fluorescence imaging. Not only that, we also hope



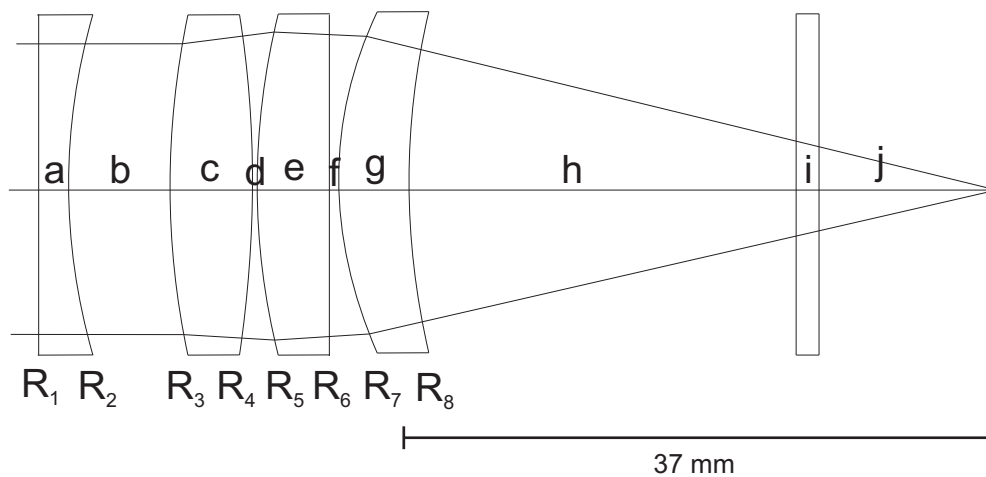
Lenses:

1: LPV25/-75
2: LPX25/100

Aluminium spacers:

S1: 6.0 mm S3: 2.77 mm
S2: 5.82 mm S4: 3.08 mm

(a)



(b)

Figure 3.18: Construction scheme. Designed, constructed and tested by Peter Baranowski and James Zacks. In (b), the lens surface curvatures are (in mm): R_1 flat, $R_2 = 39.08$, $R_3 = 103.29$, $R_4 = -103.29$, $R_5 = 39.08$, R_6 flat, $R_7 = 26.00$, $R_8 = 78.16$. The widths of the lenses and air gaps are (in mm): $a=3.08$, $b=7.24$, $c=4.97$, $d=0.40$, $e=5.12$, $f=0.40$, $g=5.07$, $h=21.00$, i (silica)=2.00, $j=12.73$. All lenses have a diameter of 25.4 mm.

to attain very small spot sizes for 830 nm wavelength dipole trapping light for a deep dipole trap. The lenses were arranged within a brass tube and separated by aluminium spacers. The tube was then mounted on a five-axis translation stage (X, Y, Z, pitch and yaw) for ease of alignment. The final dimensions of the objective are shown in Figure 3.18.

To simulate real conditions, the simulations done in [64] also take into account the vacuum glass cell window of 2 mm thickness since it will also introduce spherical aberrations and thus act as an effective lens. Results show that the diffraction limit of this system was $1.74 \mu\text{m}$ and that the simulated rms spot size given by this system provided that the entire aperture size was used was $< 0.5 \mu\text{m}$ (diffraction limited performance). Given this diffraction limited performance rather than aberration limited, we apply Rayleigh's criterion which gives the smallest resolvable distance Δl as

$$\Delta l = 1.22 \frac{f\lambda}{D} \quad (3.1)$$

where f is the effective focal length of the system, λ is the wavelength of the light used and D is the diameter of the aperture. In our case, $f=37$ mm, $D=23.5$ mm and $\lambda=780$ nm which gives $\Delta l=1.74 \mu\text{m}$. The effective numerical aperture of the system was $\text{NA}=0.27$.

3.3 Diagnostics

3.3.1 Recapture method

Fluorescence light from a MOT cloud is used to monitor the number of atoms for diagnostic purposes. A collection lens is placed as close as possible to the MOT behind which we have a photodiode placed at the point at which the collected light is focussed. The relevant calculations required to determine approximately the number of atoms in the cloud is given in later chapters but comparison of fluorescence signals is important so that we run the experiment each day under the same conditions.

In the experiment, we are able to preset a value of the fluorescence signal level which shall from now on be called the trigger level. When the experiment begins, the MOT cloud initially grows and so will the fluorescence signal. When the signal reaches the trigger level, LabVIEW is programmed to proceed with the next stage of the experiment. A useful diagnostic method is to run the experiment, perform the desired operations on the cloud of atoms before recapturing the cloud back in the MOT. The fluorescence level at this point is noted and a comparison between the initial and final signal immediately provides information on the percentage of atoms lost during the procedure. Recapture measurements were used in this experiment to maximise the efficiency of optical pumping between the molasses stage and the loading of the magnetic trap, to know the fraction of atoms lost after the molasses stage and to measure the lifetime of the magnetic trap.

3.3.2 Absorption imaging

Basic principles

Absorption imaging is the most commonly used method of diagnostics in atom optics experiments, because it not only yields information on number but also the cloud's spatial parameters. The cloud is illuminated with resonant light. Atoms scatter photons out of the beam, and the shadow cast by the atoms is focussed onto a charge coupled device (CCD) array. The amount of light absorbed gives the column optical density (OD) along a particular ray through cloud. Optical density is defined by Beers law and is given by

$$I = I_0 e^{-OD(x,z,\Delta)} \quad (3.2)$$

where I is the transmitted intensity and I_0 is the intensity of the incident beam. OD is dependent on the detuning of the probing beam, the column density of the cloud at the particular x and z coordinate and the absorption cross-section of the cloud. Important properties of the cloud such as temperature, density and atom number come from the analysis of images of optical density structures. The imaging optics are shown in Figure 3.19. We begin with a probing beam that has

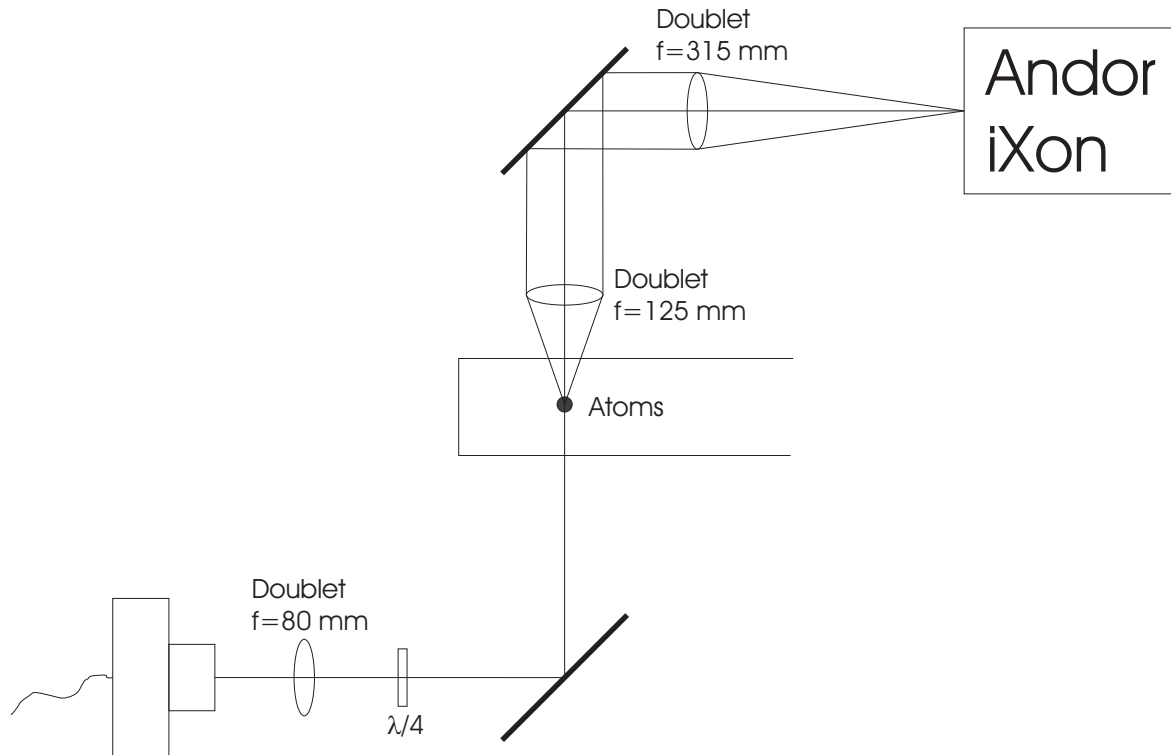


Figure 3.19: Schematic of the imaging setup for observation of condensate. For a magnification of unity, we use two $f=200$ mm singlet lenses.

already been spatially filtered using a single-mode polarisation-preserving optical fibre. The probe beam is then allowed to expand before being collimated by a doublet lens of focal length 80 mm. The collimated beam was measured to have a $1/e$ radius of 4.6 mm. There is a quarter-wave plate placed after the lens to make the probing beam circularly-polarised which is desirable because it drives the atoms on a cycling transition in the probing process and thus gives a good signal-to-noise ratio. For equation 3.2 to hold true, we want a low intensity for our probe beam. Therefore, we set the intensity of the beam to be one-tenth the saturation intensity of the probing transition. For the current beam size, this requires the total beam power to be $100 \mu\text{W}$ and we monitor this occasionally to achieve this intensity. For observation of condensates, we want a magnification of around 2.5 and this was done using two doublet lenses of focal lengths 125 mm and 315 mm. The distance between the cloud of atoms and the first lens after the science cell is 125 mm and the distance between the second doublet lens and the CCD chip is 315 mm.

To image the atoms, the current in the magnetic trap coils is turned off in less than $10 \mu\text{s}$ and the atoms are pumped into the $F = 2$ sublevel with a $200 \mu\text{s}$ pulse of light resonant with the $5S_{1/2}; F = 1 \rightarrow 5P_{3/2}; F' = 2$ transition (repumping transition). The cloud is then probed by applying a $200 \mu\text{s}$ pulse of circularly polarized light resonant with the $5S_{1/2}; F = 2 \rightarrow 5P_{3/2}; F' = 3$ transition. An AOM is used for fast shuttering of the probe light. The shadow of the atoms in the beam is then imaged onto a CCD array. Our CCD camera is a front-illuminated CCD array with pixels of dimensions $16 \times 16 \mu\text{m}$. The entire array was 512×512 pixels. The quantum efficiency at 780 nm peaks at 43% and the readout noise is 62 electrons per pixel in the fastest readout mode of 10 MHz. The camera feeds on an edge trigger and sometimes electrical noise around the laboratory cause the camera to take pictures unexpectedly. To minimise this, the trigger level sent to the camera is set to high first until moments before an image was taken at which point the TTL logic level is set to low for a typical length of 15 ms before it is set to high which triggers the camera to take an image.

The standard procedure in this, and other BEC experiments, is to take three images at the end of each run of the experiment. One is a shot of the transmitted probe beam past the atoms (the shadow) after a pre-determined time of flight (TOF), the second is just the probe beam and the third shot without light or atoms is the background signal. From these three shots, we obtain the optical depth per pixel by using the expression

$$OD = \ln\left(\frac{I_{probe} - I_{dark}}{I_{atoms} - I_{dark}}\right) \quad (3.3)$$

where I_{probe} is the number of counts resulting from the probing light alone, I_{atoms} is the number of counts from the probing light after illuminating the atoms and I_{dark} is background counts. The total optical depth is the sum of all the optical depths in the image and the total number of atoms is related to this sum.

Optimisation of absorption imaging system

Several things are necessary for good absorption imaging. The first is to focus the image so that we get an accurate value of cloud sizes which will eventually help determine temperature of the cloud and cloud peak density. The doublet lens immediately after the science cell shown in Figure 3.19 is mounted on a translation stage capable of micrometer precision adjustment. Varying the position of this doublet lens with this stage, we measure the mean and standard deviation of the cloud size over ten shots. We then take position of the lens where the radial cloud size is measured to be the lowest as the focus.

The second important consideration is magnification. Magnification must be carefully measured to ensure that cloud sizes are accurate (and hence the calculation of atom number). Magnification is determined by measuring the displacement of the cloud as it falls under gravity. From classical mechanics, the displacement s of the cloud under gravitational acceleration is given by $s = s_0 + \frac{1}{2}gt^2$. We use this expression as a fitting function to the results and extract the apparent acceleration due to gravity g' (in ms^{-2}). The magnification M is then simply $M = \frac{g'}{g}$. Graph

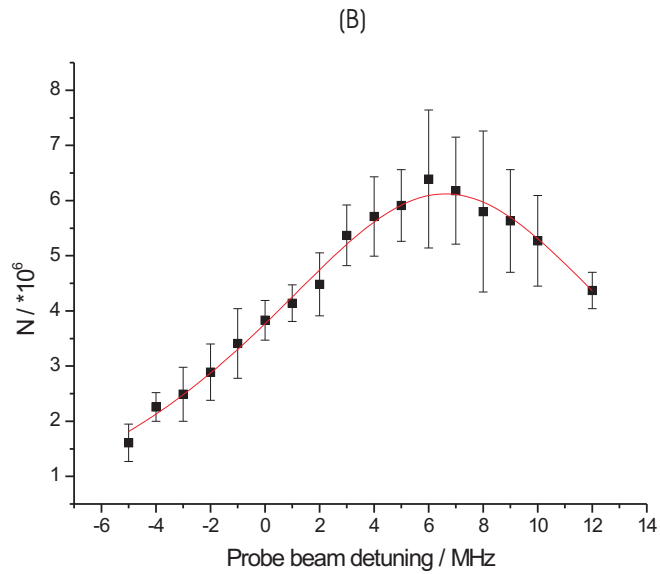
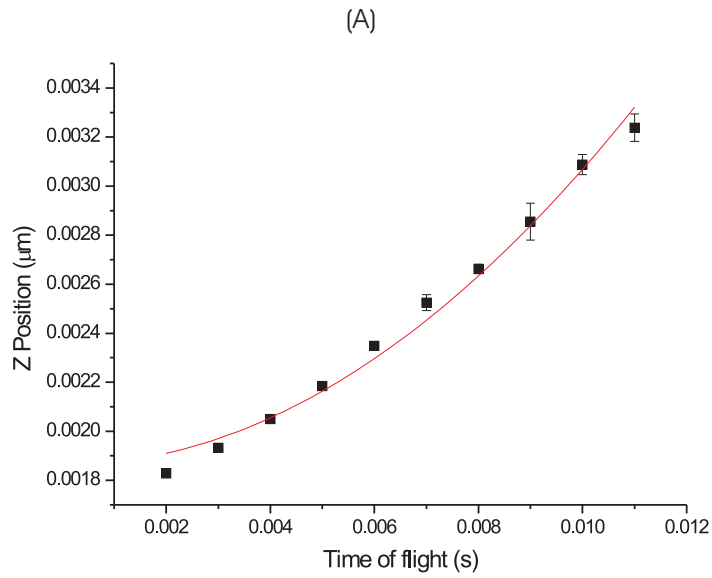


Figure 3.20: Characterisation of absorption imaging. (A) shows measurement of magnification where the cloud position has been converted from pixels to microns. (B) shows a scan of detuning to ensure that the probing beam frequency is on resonance with the $F = 2 \longrightarrow F' = 3$ transition.

(A) of Figure 3.20 shows the graph plotted. The magnification of our imaging system was found to be 2.46 ± 0.09 .

Absorption and refraction are closely related. In the region of strong absorptive resonance the refractive index has a dispersive line shape. Therefore for light with a frequency detuned from resonance, the refractive index of the cloud is no longer 1 and due to variations in the density across the cloud, the cloud acts like a lens. If the imaging system is well focussed, no change in the shape of the cloud is observed as the probe beam is detuned. However, if the cloud is out of focus then the cloud shape becomes very distorted. Therefore it is very important that the probe beam is on resonance with the desired transition. As mentioned earlier, an AOM is used for fast shuttering of the probing light. The same AOM is also used to vary the frequency output of the probing light. The AOM feeds on an amplified RF signal from a Voltage Controlled Oscillator (VCO). A DC signal is input into the VCO and the VCO outputs an RF signal. This frequency was measured with a frequency counter and was calibrated against voltage input. From here we deduce a relation between the VCO DC input and the frequency output of the VCO from which we estimate the setting at which we will have resonant probing beam. However, this relation may not be accurate and must be confirmed via experiment. We begin with a thermal cloud of atoms not optically pumped and therefore in the ($F = 2, m_F = -2$) state. When probing, to avoid complications with any possible presence of thermal cloud in the ($F = 1, m_F = -1$) state, we do not expose the cloud to the repumper beam. Then, keeping the intensity of the beam to be the same throughout, we vary the frequency output of the VCO and measure the apparent number of atoms for each frequency value. Graph shown in (B) of Figure 3.20. In this graph, 0 MHz on the x-axis is the value at which we expected resonance but we measured highest apparent number of atoms at calibrated frequency of 6.63 MHz. This means that our calibration of VCO DC input and the frequency output was slightly flawed and this must be taken into account.

Any probe beam light collected by the camera that can not be absorbed by the atoms will reduce the observed OD and will result in an underestimate of the atom number. This is called optical depth saturation. A symptom of optical depth saturation is when the cloud profile displays a flat top. This tends to happen during the later stages of evaporative cooling when the cloud becomes extremely dense. The way to get around this is simply to increase the time-of-flight until the peak optical depth observed is significantly less than the optical depth where saturation occurs. After these processes of optimisation, we typically get a shot-to-shot noise (standard deviation) on the atom number of 5% or less and almost never above 10%.

3.3.3 Image analysis

The purpose of the image analysis is to obtain reliable density distributions of the cloud of atoms, either in or after ballistic expansion. All properties of condensates and thermal clouds are inferred from these density distributions by comparing the measured distributions with models of the atomic gas as described in this section.

Firstly we discuss methods for determining various cloud parameters like size expansion after a certain time-of-flight, peak density and temperature. Secondly the calculation of atom numbers has been put in a separate section because this determination is different for absorption imaging and fluorescence imaging, the two different types of imaging that are going to be implemented. Furthermore, the experiment requires a different program especially to count low atom numbers later for sub-shot noise measurements and this will also be discussed.

Cloud parameters

Density distribution of a thermal cloud We consider the trapped gas to be in a harmonic potential of the form

$$U(r) = \frac{1}{2}m(\omega_x^2x^2 + \omega_y^2y^2 + \omega_z^2z^2) \quad (3.4)$$

In the ideal gas limit, the density distribution for the trapped gas is given as

$$n(r) = \frac{N}{\pi^{\frac{3}{2}}} \prod_{i=1}^3 \frac{1}{x_{i,0}} e^{-x_i^2/x_{i,0}^2} \quad (3.5)$$

where N is the number of atoms and $x_{i,0}$ is the $\frac{1}{e}$ half-width of the cloud of atoms. Fitting a Gaussian form to the cloud image gives values for $x_{i,0}$ from which the peak cloud density is found from

$$n_{pk} = \prod_{i=1}^3 \frac{N}{\pi^{\frac{3}{2}} x_{i,0}} \quad (3.6)$$

Also since the trapping frequencies are known we can find temperature T . This temperature together with n_{pk} are used to calculate phase space density.

Time-of-flight expansion In free expansion, the shape of the cloud remains Gaussian except for a phase factor. After a time t of expansion, the cloud size is simply rescaled as $x_{i,0}^2 = x_{i,HO}^2 + v_{i,HO}^2 t^2$ where $v_{i,HO} = \sqrt{\hbar\omega_i/m}$ is the rms velocity of the cloud. This expression can also be written as $x_{i,0}^2 = x_{i,HO}^2 \sqrt{1 + \omega_i^2 t^2}$. The thermal cloud expands isotropically once it becomes much larger than its original size.

Temperature From the equipartition theorem, for a trapped gas in a harmonic potential, the temperature and the size of the cloud ($\frac{1}{e}$ half-width) are related by the expression

$$k_B T = \frac{1}{2} m \omega_i^2 \frac{x_{i,0}^2}{\sqrt{1 + \omega_i^2 t^2}} \quad (3.7)$$

Atom number The total number of atoms N is calculated from the optical depth expression in equation 3.3 by summing over the absorption signal seen across the two-dimensional image of the cloud. Thus, in resonant absorption, one obtains

$$N = \frac{A}{\sigma_0} \sum_{pixels} OD(x, y) \quad (3.8)$$

where A is the effective pixel size after taking the magnification of the imaging system into account and σ_0 being the resonant absorption cross-section ($\sigma_0 = 2.91 \times 10^{-9} \text{cm}^2$). Take note that $A=MA'$ where M is magnification and A' is the actual pixel area ($A'=(16 \mu\text{m})^2$).

Producing BEC

4.1 Loading the magnetic trap

The first step towards Bose-Einstein Condensation (BEC) is to optimise the loading of atoms into the experimental MOT, i.e. load as many atoms as possible into the MOT quickly. To achieve this, there are various parameters associated with the pyramidal MOT and the experimental MOT that were adjusted. The general aim of the pyramidal MOT is to cool atoms from room temperature before these cooled atoms are transferred to the science MOT via a small aperture in the pyramidal setup. As a rule of thumb, being able to trap as many atoms as possible in the pyramidal MOT would be a good start. As for the experimental MOT, ideally, we would like to trap as many atoms as possible in a cold and dense cloud by having a large magnetic gradient, high laser beam detuning and lots of cooling beam power. However, our available laser beam power is limited and therefore we had to be content with a reasonable magnetic gradient (10 G/cm) and laser beam detuning in order to get a decent number of atoms. In addition to the parameters related to the experimental MOT, we also varied the detuning of the cooling beam entering the pyramidal MOT. This is because this detuning affects the density of our cloud in the pyramidal MOT which affects the rate of atoms transferred through the aperture.

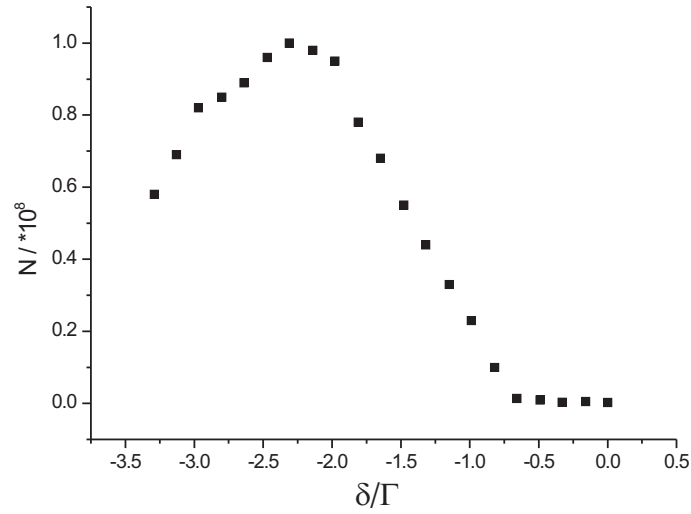


Figure 4.1: Optimization of the atom number in the pyramidal MOT. The dependence of the atom number on laser frequency detuning (the trap light detuning is given in units of δ/Γ where Γ is the natural decay rate of the excited level).

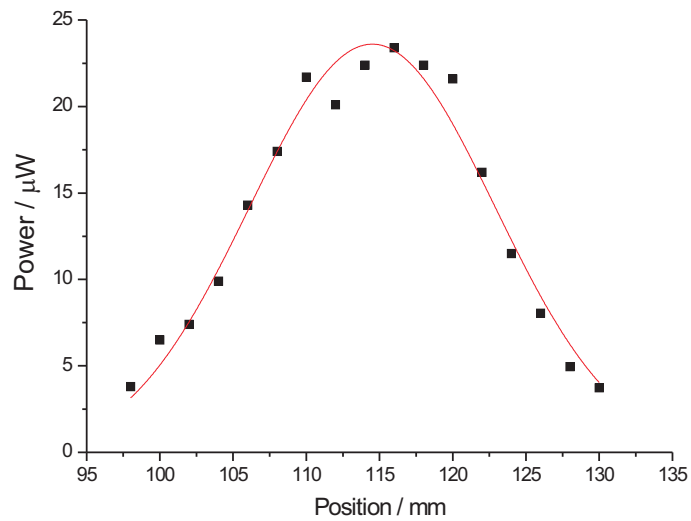


Figure 4.2: Measurement of the intensity profile of the laser beam going into the pyramidal MOT

4.1.1 Pyramidal MOT

The optimisation of capture rate of atoms in the pyramidal MOT leads to fast loading of the experimental MOT. The only variable which we varied to optimise this was the laser detuning with respect to the $F = 2 \longrightarrow F' = 3$ transition. The number of atoms is determined from fluorescence measurements. A collection lens of focal length 10 cm was placed at approximately 20.5 cm from the atoms collected in the pyramid and a photodiode was placed at about 16 cm from the lens. The collection lens has a clear aperture diameter of 6.2 cm when mounted. Figure 4.1 illustrates the dependence of the atoms captured in the pyramidal MOT on the laser detuning. There was 3.2 mW of repumper beam power and 41.6 mW cooling beam power at the time of measurement. The radius ($1/e$) of the cooling beam was measured to be 11.9 mm and this was measured by translating a partially closed iris across the beam and measuring the beam power transmitted through the small aperture (1 mm diameter) presented by the iris. Figure 4.2 shows the graph for this measurement. We ran 28 Amperes of current through the pyramidal quadrupole coil to give a magnetic gradient of 14 Gcm^{-1} .

4.1.2 Experimental MOT

This section describes the optimisation of the loading of the science MOT and gives some results for its loading curve and lifetime.

The number of atoms in our MOT can be estimated given various parameters like beam detuning, beam intensity and the amount of fluorescence light that the atoms emit. We begin with a simple setup where we have a $f=8$ cm lens with an effective aperture diameter of 2.3 cm placed about 16 cm away from the cloud of atoms. This lens is the collection lens and the collected fluorescent light is then focussed onto a photodiode. This photodiode has a responsivity of 63.1 V/mW . So given the photodiode signal which we observe with an oscilloscope, we know the power of the light that falls on the photodiode, the solid angle presented by the collection lens and therefore total light emitted by the cloud of atoms. From this

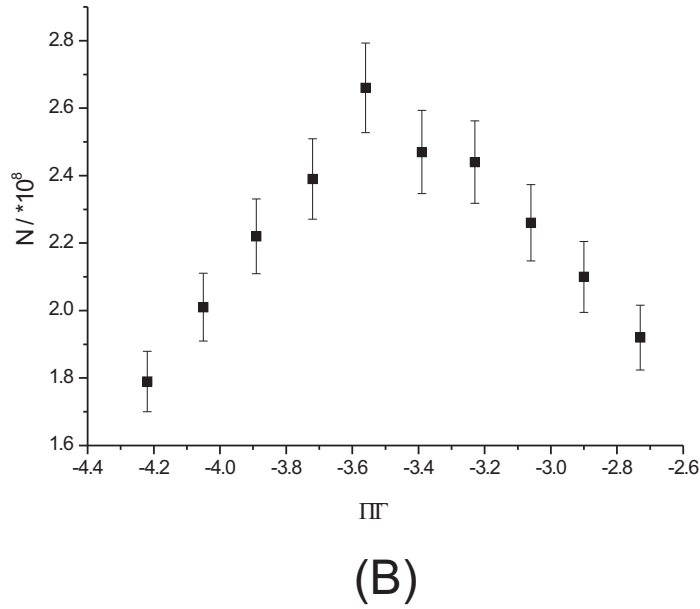
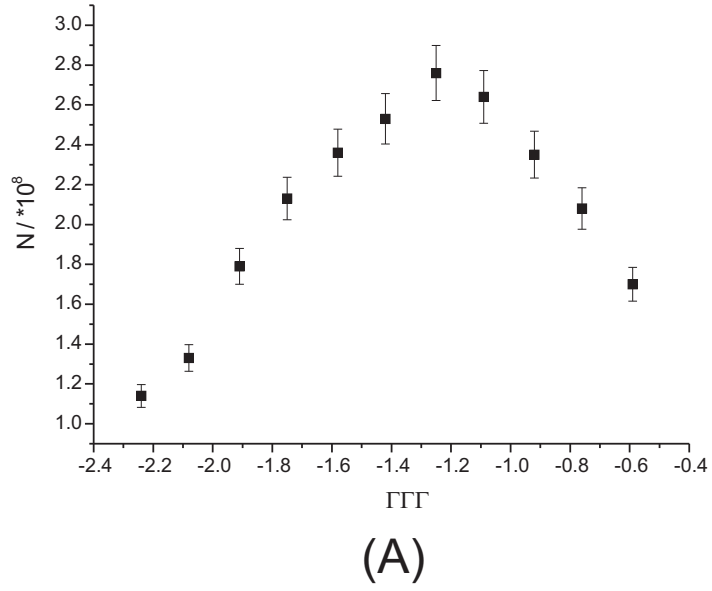
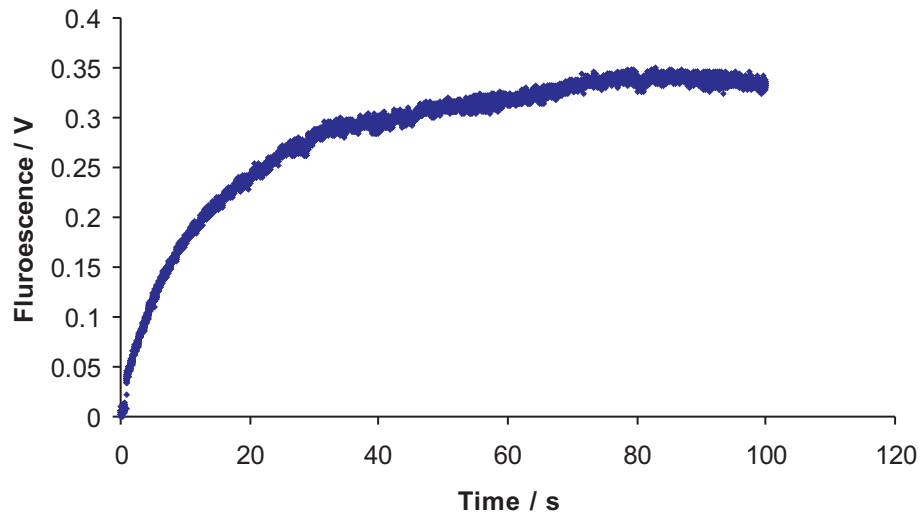
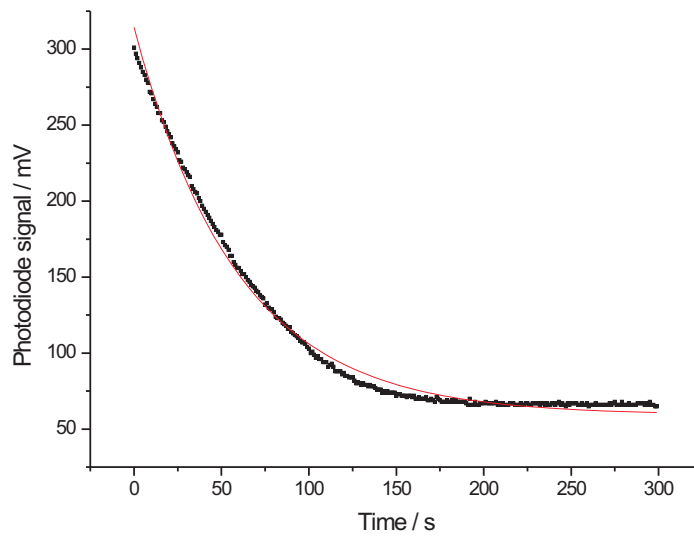


Figure 4.3: Optimization of the number of atoms in the experimental MOT depending on (A) cooling light detuning and (B) pyramidal MOT beam detuning . The dependence of the number on laser detuning (the trap light detuning is given in units of δ/Γ where Γ is the natural decay rate of the excited level). We had 38 mW of cooling light power, 6.6 mW of repumper beam power and a magnetic gradient of about 8 Gcm^{-1} . These beams were measured to be of $9.1 \text{ mm } \frac{1}{e}$ radius.



(A)



(B)

Figure 4.4: (A) Experimental MOT loading curve and (B) Experimental MOT decay lifetime.

information, we estimate the number of atoms in the cloud at the centre of our MOT. The first objective was to optimise the loading rate by varying the frequency detuning of the cooling beam and also of the pyramidal MOT beams. We then make a comparison based on the signal observed on the oscilloscope after loading for 10 seconds. It is assumed that the number of atoms attained in the MOT after 10 seconds is a good indicator of the eventual number of atoms. The results are shown in Figure 4.3.

Figure 4.4 shows two other features of our MOT. The first graph shows the loading curve. We attain approximately 2.8×10^8 atoms in the first 10 seconds and we reach equilibrium of about 6×10^8 atoms after about 100 seconds. This means we have an initial loading rate of about 2.8×10^7 atoms per second. As for the lifetime, we fitted a standard exponential decay to the second graph and this yielded a lifetime of 255 seconds which is slightly more than 4 minutes. These experiments are done under the same conditions as those performed in Figure 4.3 but this time round with a detuning of -10 MHz.

4.1.3 Compressed MOT and optical molasses

The MOT was optimised to load as many cold atoms as possible in the shortest amount of time. However, the conditions that are best for loading give a cloud of atoms that is too hot to transfer efficiently into a magnetic trap. Several more processes are required to further cool down the atoms and give a significantly higher density. They are the so-called Compressed MOT (CMOT) and the optical molasses stage.

The CMOT stage serves two purposes: to increase phase-space density of the cloud and also to match the centre of the MOT to the centre of the magnetic trap. The current running through the shim coils is varied to move the centre of the MOT so that it coincides with the centre of the magnetic trap. Initially, if the cloud is not exactly at the centre of the magnetic trap, the cloud of atoms undergoes an oscillation about the centre of the magnetic trap and this sloshing

leads to undesirable heating of the cloud. The amplitude of this oscillation depends on both the initial position of the cloud with respect to the magnetic trap and the initial velocity of the cloud of atoms. So to minimise the amplitude of this oscillation, one should match the centres and also ensure that the molasses stage is done correctly. For the molasses stage the quadrupole magnetic field was turned off at the end of the CMOT stage and the shim coil currents were set at the values which give a smooth, even and radial expansion of the cloud (i.e. the shims cancel any residual field). There were two infrared cameras observing the MOT from orthogonal directions, and therefore it was possible to observe the expansion of the cloud in all directions. The first iteration in the optimization of the shim coil settings was done by observing the cloud. The shim current settings during the molasses stage were varied until the cloud was seen to expand uniformly and radially. It should take at least one second before the cloud disappeared completely whereas for non-optimal settings the cloud shot off in one direction. These settings were noted. To observe the cloud oscillation (sloshing), the magnetic trap was turned on immediately after the molasses and optical pumping stage and then the hold time of the cloud in the magnetic trap was varied before taking an image each time. A profile of cloud position vs hold time in the magnetic trap showed a clear indication of oscillation about the centre of the trap.

We took images after twenty different hold times (at reasonable intervals of few tens of milliseconds) to observe the position of the cloud. The standard deviation of these measurements gave a measure of the amplitude of oscillation. This method worked well to minimise sloshing. We then varied the value of the shim coil current. Taking a set of positions each time, we noted the standard deviation values of cloud position for each set and compared them. This was done in all three directions. Not only did we vary the shim settings for the CMOT stage, we also varied the shim settings for the molasses stage to minimise sloshing. The settings for the two stages were varied iteratively until we find that the cloud hardly moved throughout the hold time in the trap. Once this was done, we optimised the CMOT and molasses stages for high atom number and phase space density by fine-tuning the shim

current settings for both of these stages.

The effectiveness of the CMOT stage depends on the magnetic gradient, laser frequency detuning and duration of the stage. The magnetic gradient is typically increased to help increase collision rate between the atoms. The accompanying detuned laser beams minimise multiple scattering between the atoms. This causes a momentary collapse of the atoms towards the centre of the trap which increases the density of the cloud. We discovered that increasing the magnetic gradient significantly resulted in shifting of the centre of the MOT and more current needed to be pumped through the shim coils to produce the magnetic field required to shift the MOT centre back to its original position. This caused undesired heating of our shim coils and therefore as will be seen, we did not increase our magnetic gradient by a great amount. Since a large laser beam detuning during the CMOT stage is most effective when accompanied by large magnetic gradients, now that we could not increase the latter by a great amount, understandable we have found that laser detuning did not affect this stage by very much if at all.

Figure 4.5 shows the data taken during the optimisation of the CMOT stage. We optimised for number of atoms and phase space density. We varied the duration of this stage and then measured number of atoms and phase space density with different magnetic gradients. The chosen values of length of the stage to 2 ms only with a final magnetic gradient of 12.5 Gcm^{-1} gave us an atom number of $N = 5.8 \times 10^7$ and phase space density of $\rho = 3.5 \times 10^{-8}$. Just for comparison, the phase space density of our MOT cloud will be of the order of 10^{-10} .

The effectiveness of the molasses stage depends on the laser frequency detuning again and length of this stage in milliseconds. We detune the laser beams by offsetting the laser current directly after unlocking the lasers at the right time. We vary the laser frequency detuning and length of stage to maximise phase space density and at the same time still have a reasonable number of atoms ($\approx 6 \times 10^7$) in the cloud. We found that there is hardly any more cooling after around 30 MHz red-detuned with a length of the stage of 10 ms. These procedures assume good

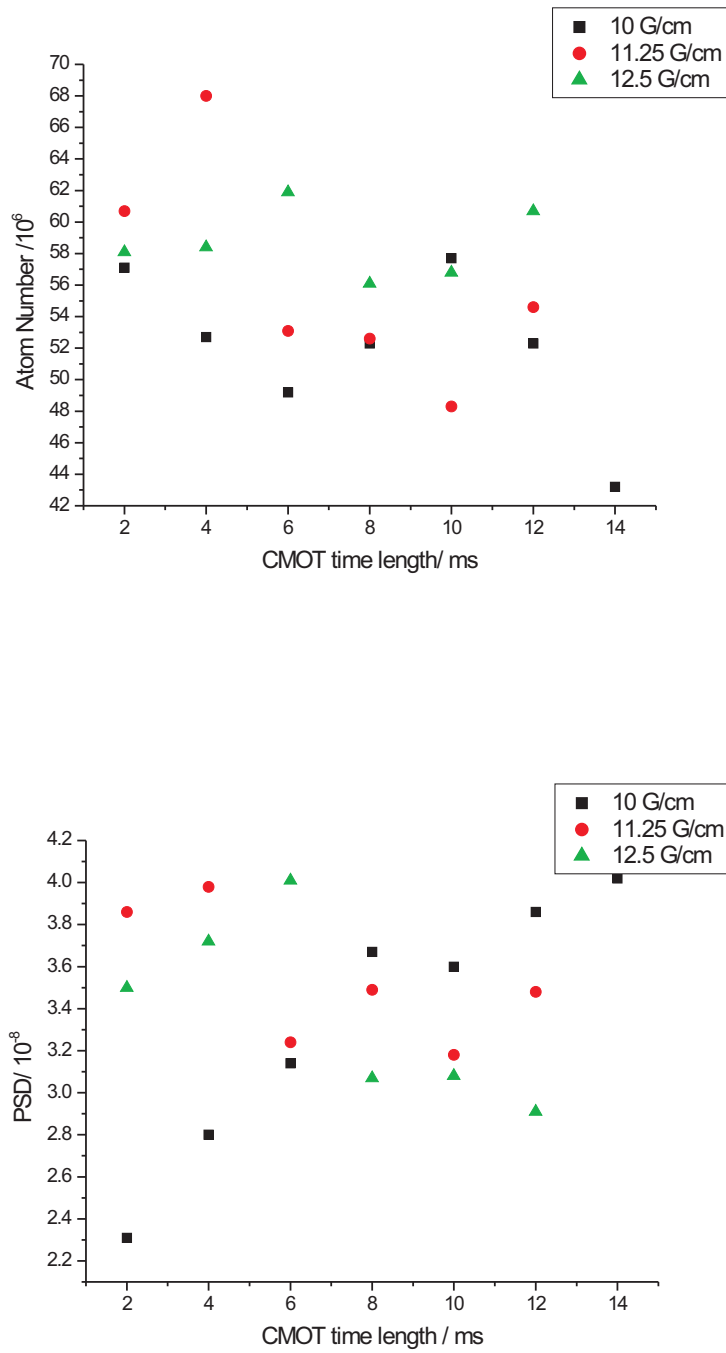


Figure 4.5: Optimisation of the Compressed MOT (CMOT) stage.

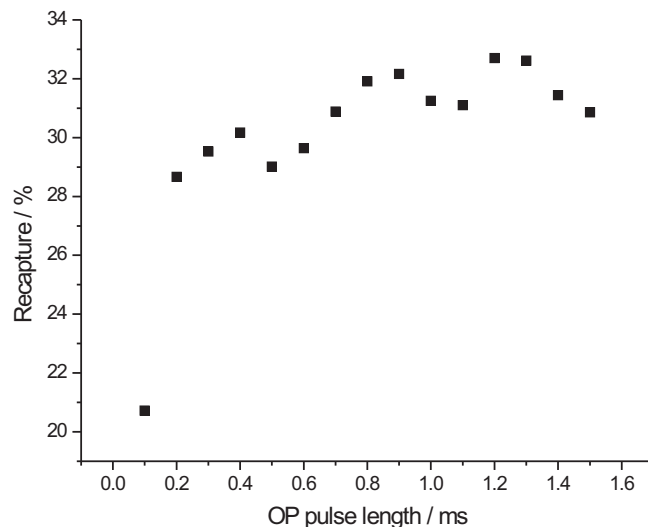


Figure 4.6: Percentage of atoms recaptured against pulse length after being held in the magnetic trap for five seconds.

alignment of the laser beams but occasionally the cloud of atoms is hot if any of the MOT beams has become misaligned. It is generally necessary to realign the beams once every three months or so to maintain the cold temperature of the cloud in the magnetic trap.

4.1.4 Optical pumping

The optical pumping of atoms into the $F = 1, m_F = -1$ state takes place immediately after the optical molasses stage. This is the only low-field seeking m_F state in the $F = 1$ level and trapping the atoms in this state minimises the problem of inelastic collisions of atoms due to spin exchange compared to the $F = 2$ hyperfine state.

The optical pumping is carried out by exposing the atoms to an optical pumping beam which is resonant with the $5S_{\frac{1}{2}} F = 2 \rightarrow 5P_{\frac{3}{2}} F' = 2$ transition. This beam needs to be σ^- polarised to populate the $F = 1, m_F = -1$ level and therefore requires a quantisation axis. This field is provided by one of the shim coil pairs turned on to have 2 Amperes of current running through it during the OP pulse.

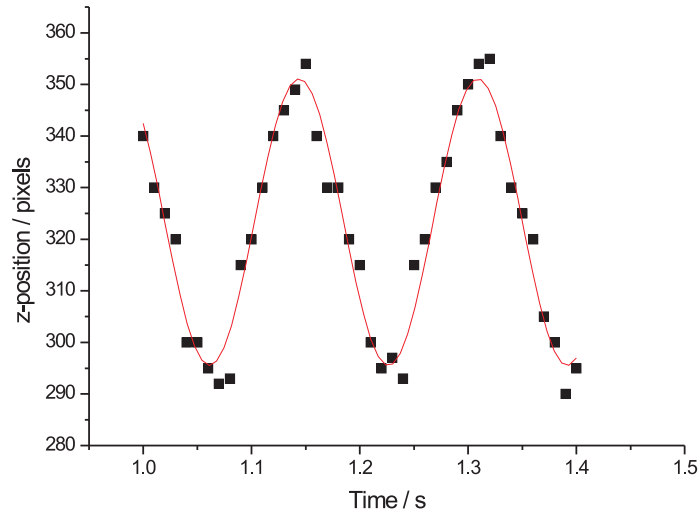
This field value was adjusted experimentally to optimise the recapture percentage. This means noting the fluorescence in the MOT, loading the magnetic trap and holding the atoms in the magnetic trap for five seconds, and then recapturing the atoms into the MOT in order to obtain the fluorescence measurement. The one last task for this stage is to determine the length of this pulse. The optical pumping beam has a power of 1.5 mW and since this beam comes out the same fibre as the probing beam, it will have the same $1/e$ half-width radius as the probe beam. Figure 4.6 shows the pulse length required to obtain maximum recapture percentage. We fixed the pulse length to 0.9 ms. Another way to ensure that the atoms are all in the $F = 1, m_F = -1$ state is to check that when the atoms are imaged during the absorption imaging stage without being exposed to the repumper beam, one sees nothing at all. To check for optical pumping efficiency, we measure recapture rate of atoms immediately after magnetic trap loading. We typically have 65% conversion into the $F = 1, m_F = -1$ state and a shot-to-shot noise of about 5% or even less.

4.2 Magnetic trapping

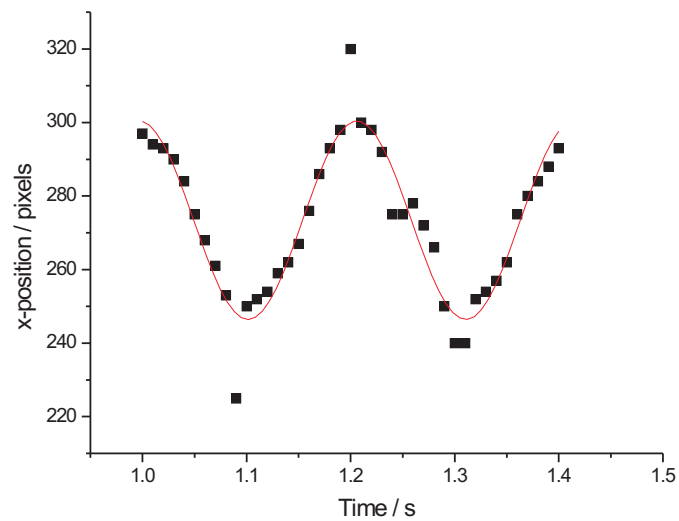
To accurately determine properties of the cloud such as temperature which is related to the phase space density, it is important to know the trapping frequencies of our magnetic trap. As mentioned in earlier chapters, at magnetic trap loading, the current through the coils is 200 Amperes through the overall path and 150 Amperes through the bypass path which leaves 50 Amperes through the bias coils.

4.2.1 Measurement of trapping frequencies

We calculated the magnetic fields and the trapping frequencies numerically when designing the trap. However, the imprecision in making the coils corresponds to about 10% uncertainty which makes it impossible to determine the trap frequencies extremely accurately. The most precise way of determining the oscillation frequency of atoms in the magnetic trap is by using the cloud of atoms. The trap frequencies are essentially the sloshing frequencies as mentioned previously. We in-



(A)



(B)

Figure 4.7: Measuring the frequencies of the magnetic trap. From these plots of position vs time we extract (A) radial and (B) axial trapping frequencies. Axial frequency is 4.78 ± 0.08 Hz while radial frequency is 6.06 ± 0.05 Hz. These clouds were measured after a time-of-flight of 3 ms.

duce sloshing upon loading the magnetic trap by modifying the trapping potential faster than the atoms can follow. This is typically done by suddenly changing the shim settings and then bringing them back again to their original values within a few milliseconds. We then note cloud position varied over hold time to obtain a set of data taken such as that in Figure 4.7.

We do not always wait for the MOT level to reach its equilibrium level before proceeding with the experiment. To save time, we load the MOT to approximately half its equilibrium level. Given this level, we typically have a cloud in the magnetic trap with parameters $N = 7 \times 10^7$, $T = 50 \mu K$ and phase space density $\rho = 3 \times 10^{-8}$. The shot-to-shot noise on our final atom number is typically 5%.

4.2.2 Adiabatic compression and the tight Ioffe trap

The last step in preparing the cloud of atoms for evaporative cooling is adiabatic compression of the magnetic trap. The efficiency of evaporative cooling is highly dependent on this parameter. Given that our trap falls under the class of Ioffe traps where the magnetic field profile around our region of interest has been discussed in previous chapters, the best way to tighten our trap would be to lower the overall bias field B_0 . This is done by increasing the current of our compensation (or bias) coils until B_0 is as low as possible (but non-zero).

When we use the maximum voltage that our power supply for the magnetic trap could give which was 8 V, we managed to draw a maximum of 262 Amperes. After a current ramping stage, we then also had 262 Amperes of current running through the bias coils. We monitor the overall bias field at the centre of the magnetic trap by performing a forced evaporation on the cloud of atoms using radio-frequency waves from our signal generator. We generate a radio-wave of amplitude 20 dBm and then we reduce the final rf frequency in an evaporation stage from 30 MHz and find the frequency at which the all the atoms are ejected from the cloud. For the $m_F = -1$ state of our atoms, the calibration between RF frequency and magnetic field is $m_F g_F \mu_B / h = 0.7$ MHz/Gauss. We find that the overall bias field

after ramping stage was 10 Gauss after noticing that there were no atoms left after 7 MHz.

This implied that even after utilising the compensation coils, the lowest overall bias field that we obtained at the centre of the magnetic trap was 10 Gauss. To reduce this further for a tightest possible magnetic trap, we had another pair of coils to perform the remaining compensation of the bias field. This set of coils is called the secondary bias coils. We kept increasing the current flowing through this secondary coil and we kept monitoring the overall bias field until we approximately had a field of 1 Gauss or slightly lower. We observed that running a current of 1.72 Amperes results in a cloud of atoms which disappeared at around 0.5 MHz, corresponding to 0.71 Gauss. From here we now know the final parameters of our ramping stage. What is left is to determine the ramping time. Due to the highly elliptical shape of our large cloud in the tight magnetic trap which was larger than our imaging area, it is very difficult to use our image analysis program to fit a Gaussian profile over the cloud and obtain an axial size of our cloud. Therefore very unfortunately we could not find useful parameters of the cloud of atoms such as density, temperature and most importantly collision rate immediately after the trap was ramped. In fact, any cloud temperature greater than $30 \mu\text{K}$ was difficult to measure. We optimised ramping time by firstly establishing an evaporation sequence for the first few stages and once we have successfully evaporated the cloud to a much colder cloud, we vary the ramping time to see if we can have a quick ramp without overheating the initial cloud. We found that we can ramp the current in one second and our evaporation sequence remains effective. Therefore, we fixed the ramping time to one second.

The next step is to further understand the tighter magnetic trap by measuring its trapping frequencies and lifetime. Measuring the trapping frequency of this trap requires some knowledge of the Ioffe trap. As mentioned previously, the cloud experiences an approximately harmonic potential only when its temperature T fulfills the condition given by $k_B T < \mu B_0$. Given the cloud in our $m_F=-1$ state,

this corresponds to about $33 \mu\text{K}/\text{Gauss}$. Since our overall bias field was calculated to be 0.71 Gauss , this means our cloud needs to be significantly lower than $23 \mu\text{K}$ before it is in the harmonic region. This therefore means that we have to initially establish a good evaporation routine which will take our cloud to temperatures lower than $23 \mu\text{K}$. The routine will be further discussed in the next section.

With an initial evaporation sequence, we managed to reduce the temperature of the cloud to about 300 nK , which is a sufficiently cold cloud we could use to measure trapping frequencies. As long as the amplitude of the oscillation is small enough, we can assure ourselves that the cloud remains in a harmonic region of the magnetic trap. Figure 4.8 shows the measurements leading to the extraction of the trapping frequencies.

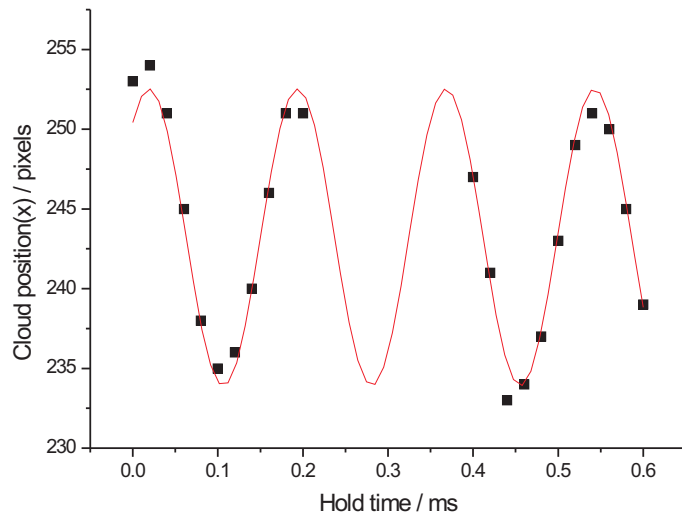
We then measured the lifetime of our cloud in the tight trap. This is a useful quantity to take note of because it gives us an idea of how much time we have to complete our evaporation sequence before our atom number fades significantly. Since at this point our cloud density is not great, our dominant loss mechanisms would be background collisions with other Rubidium atoms and the cloud being in an imperfect vacuum. The cloud lifetime was measured by measuring the recapture rate for various hold times as shown in Figure 4.9.

4.3 Evaporative cooling

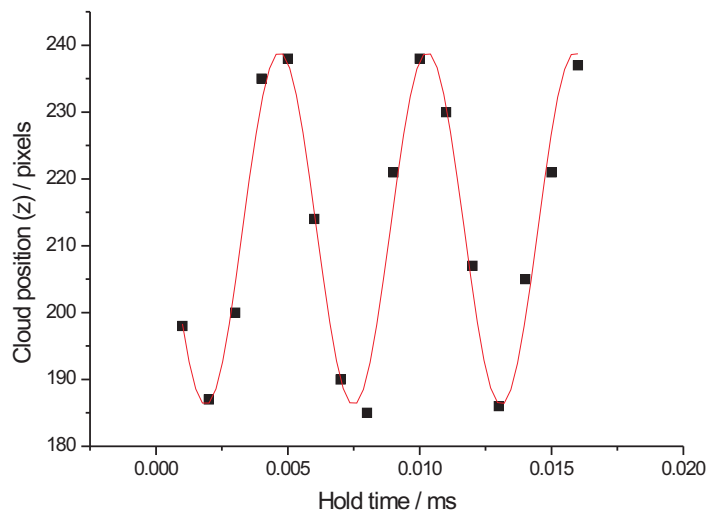
4.3.1 Evaporation stages

This section describes the final stage of the experimental sequence to BEC: evaporative cooling. Given that our signal generator (Stanford Research Systems DS345) could give a maximum frequency of 30 MHz , the first step was to check if there are atoms in the region of the magnetic trap where the resonance has that frequency. As it turned out, there was no convincing evidence that there were atoms so far from the centre of the magnetic trap.

We remove or evaporate the higher energy atoms based on the assumption that



(A)



(B)

Figure 4.8: Measuring the oscillation frequencies of atoms in the tight magnetic trap. From these plots we extract (A) axial and (B) radial trapping frequencies. Axial frequency is 5.73 ± 0.03 Hz while radial frequency is 178.6 ± 1.9 Hz.

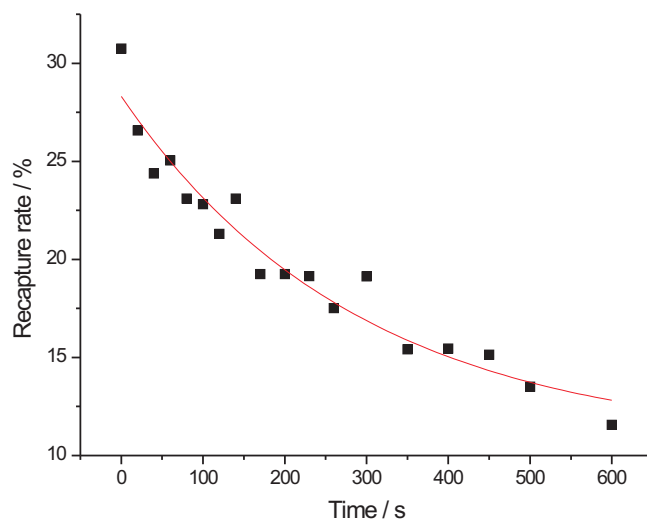


Figure 4.9: Measuring the lifetime of our magnetic trap. This was measured to be 290 ± 75 seconds.

higher energy atoms tend to travel on trajectories that stray farther from the centre of the magnetic trap into regimes of larger magnetic fields [67]. The trap is bathed in a spatially uniform, radio frequency magnetic field. There is then an ellipsoidal surface of constant dc magnetic field at which the spin flip frequency of an atom is resonant with the rf. Atoms whose trajectories pierce this surface are transferred from $|F = 1, m_F = -1\rangle$ trapped state to the $|F = 1, m_f = 0\rangle$ untrapped or the $|F = 1, m_f = 1\rangle$ state which is antitrapped and so are permanently removed from the magnetic trap. By ramping down the frequency, we shrink the ellipsoidal surface, forcing evaporative cooling to continue even as the temperature and the mean cloud radius decrease.

Assuming a constant elastic collision rate within the cloud, we want to remove the same fraction of energy from the cloud per unit time. This condition results in an exponentially decreasing frequency ramp. As the collision rate changes so will the optimum exponential time constant. The functional form we shall use for time-dependent rf frequency $\nu(t)$ is therefore

Final rf frequency / MHz	Length of ramp / seconds	RF amplitude / dBm
18	20	20
12	15	20
8	15	20
3	12	20
1.75	10	10
0.85	8	10
0.56	5	10

Figure 4.10: Evaporation sequence. Sequence starts at 30 MHz and the entire sequence takes 85 seconds.

$$\nu(t) = (\nu_{start} - \nu_0)e^{-t/\tau} + \nu_0 \quad (4.1)$$

For the purposes of programming in LabVIEW, the evaporation sequence was divided into several stages and for each stage, the form we use was

$$\nu(t) = (\nu_{start} - \nu_0) \left[\frac{(\nu_{end} - \nu_0)}{(\nu_{start} - \nu_0)} \right]^{t/t_{end}} + \nu_0 \quad (4.2)$$

where ν_{start} is start frequency, ν_{end} is the end frequency for that stage, ν_0 is the bottom of the magnetic trap in MHz and t_{end} is the time that stage will take. There was a total of seven stages in our sequence and each stage was optimised by trial and error, varying the rf power and also the duration of that stage.

4.3.2 Observation of Bose-Einstein Condensation

The evaporation sequence used in our first observation BEC is described in Figure 4.10. The entire sequence took 85 seconds. Figure 4.11 shows the formation of our BEC. At the frequency 0.6 MHz where we first observed the phase transition, $N = 6 \times 10^5$, $T = 320$ nK and elastic collision rate was 345 s^{-1} . Immediately before the visible thermal component disappeared, we measured a temperature of 120 nK

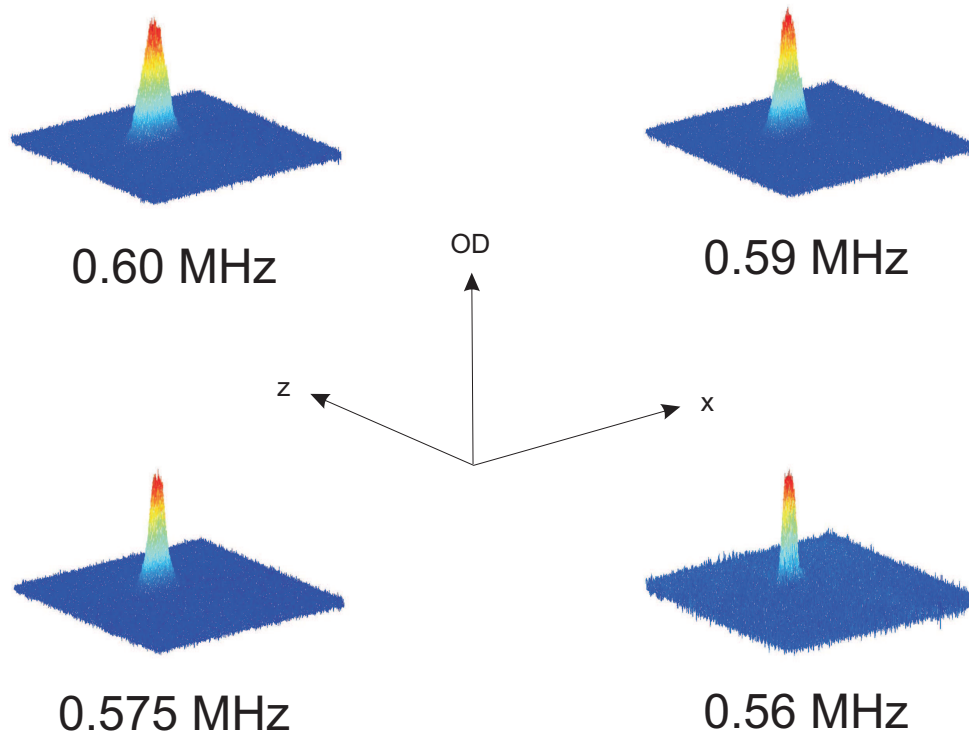


Figure 4.11: 3D plot in false colours of BEC formation during the later stages of the evaporation sequence. The frequency underneath each picture indicates the final point of the RF-sweep. All images taken after 18 ms time-of-flight in the x - z absorption imaging plane. For our imaging system, optical depth (OD) saturation occurred at about 1.7.

which was done by fitting a Gaussian profile onto the thermal wing of the cloud. When all visible thermal component have disappeared, we had $N = 1.5 \times 10^5$ in a pure BEC.

The formation of BEC provided the foundation for the next step which was dipole trapping of the atoms and potentially manipulation as well.

Dipole trapping and manipulation of ultra-cold atoms

In this chapter, we describe the procedures used to trap cold atoms in our dipole trap and to optimise the fluorescence imaging system. Finally, we describe some experiments that we have done with the atoms in the dipole trap.

5.1 Characterisation of the fluorescence imaging system

5.1.1 Initial dipole trapping

Throughout this chapter, we shall frequently refer to optical components as labeled in Figure 5.1. The dipole trapping beam is reflected via mirrors M1, M2 and dichroic mirror DM1. The dichroic mirror was designed to highly reflect 830 nm light and highly transmit 780 nm light. At a wavelength of 780 nm, the dichroic mirror reflects 92% of horizontally-polarised light and 89% of vertically-polarised light. Whereas at 830 nm, this mirror transmits 81% of horizontally-polarised light and 92% of vertically-polarised light.

The fluorescence light emitted by the atoms is transmitted through the dichroic mirror and reflected via mirrors FM1, FM2, FM3 and FM4 before finally being focused on our CCD camera. We monitor the position on which the focused dipole

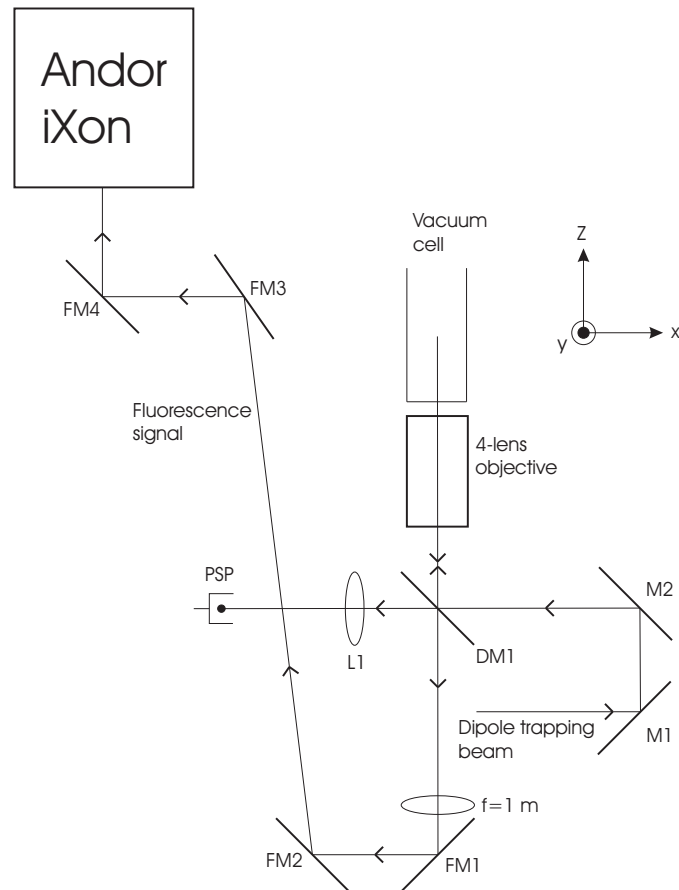


Figure 5.1: A segment of the magnetic trap section relevant to dipole trapping and fluorescence imaging. Diagram not to scale.

beam falls on the focal plane of the four-lens objective using a position-sensitive photodiode labeled PSP (Pacific Silicon Sensor DL100-7PCBA) which detects some partially-transmitted 830 nm light through DM1.

Our general plan is to begin by trying to trap some atoms in the dipole trap. Once we focus the dipole trapping beam at the centre of the magnetic trap, we can begin to optimise the positioning of the four-lens objective such that the cloud falls along the optical axis and on the focal plane of the objective.

We started the alignment procedure of the dipole trapping beam by getting an initial estimate of the position of the cloud in all dimensions. We already had a very good idea of the position of the cloud on the y-z plane because this plane was the absorption imaging plane used for all measurements thus far. The best estimate we had was the position of the cloud at the shortest time-of-flight the experiment was capable of (3 ms). The cloud position in the x-direction was not covered by the absorption imaging system and was therefore more difficult to estimate. However, a good starting position would be the x-position of the cloud in our MOT. We used a small MOT cloud and imaged it along the fluorescence imaging path to get an initial estimate of the cloud's position in the x-axis.

The next step was to focus the dipole trapping beam at this spot where we expected the centre of the magnetic trap to be. The vacuum cell together with the rest of the vacuum system was mounted on a platform with wheels on a rail. This enabled us to roll out the vacuum cell out of the way and we inserted a piece of paper with a bent tip at the edge angled at around 45° to the centre of the baseball coil geometry. We placed the centre of this bent region at the focus of the dipole trapping beam. The piece of white paper acted as a scattering surface so we could see the scattered light along both the absorption imaging path and the fluorescence imaging path. We noted the position of this focus in the x-y plane and in the y-z plane. We could move the beam around on this plane with mirrors M1 and M2 and translate the objective in and out to change focused beam position along the

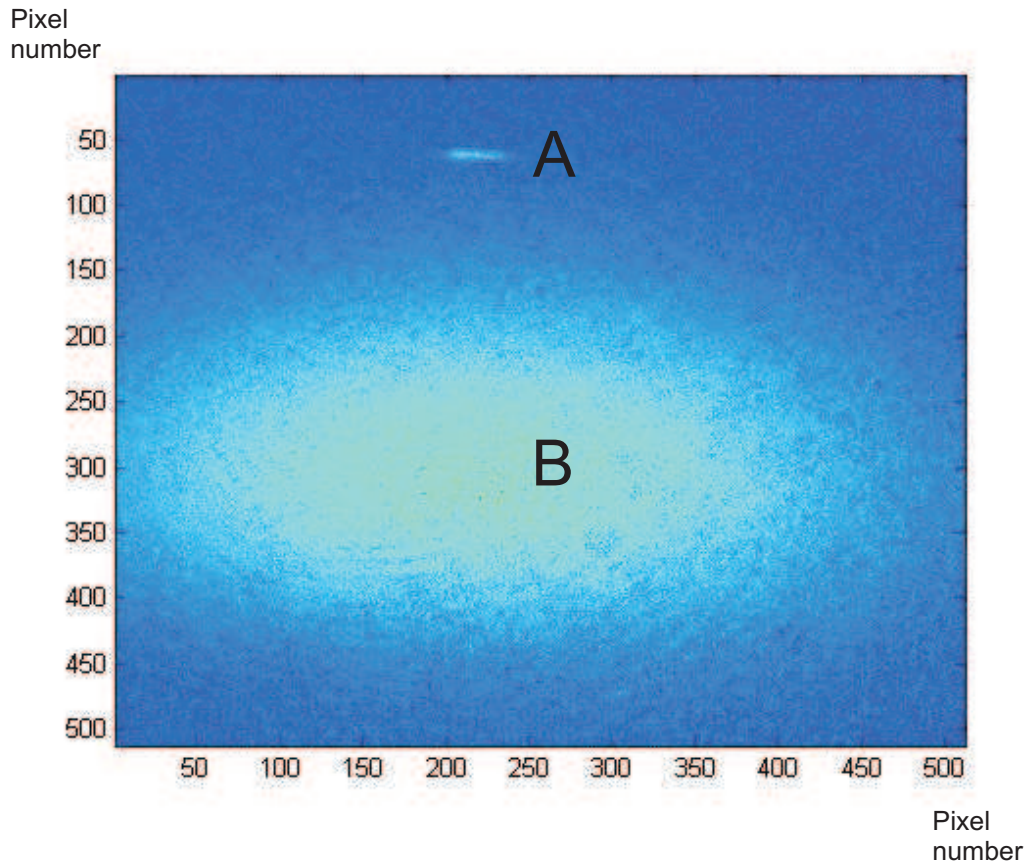


Figure 5.2: Initial demonstration of dipole trapping of cold atoms. A is the dipole trapped atoms and B shows the remaining cloud of atoms released from the magnetic trap with a time-of-flight of 18 ms. The cloud was only evaporated to final RF frequency of 1.75 MHz and had a temperature of about $10 \mu\text{K}$

z-direction. The reading given on the PSP gave the position on the x-y plane and we noted this as the first estimate of the cloud position in this plane.

The vacuum cell was then rolled back into place and we scanned the beam along the x-direction looking for any possible effects on the cloud. The beam was left on perpetually while we perform evaporative cooling on the cloud. The cloud will ‘feel’ heating effects generated by the presence of this dipole trap because at this moment the dipole trapping beam was still poor on pointing and intensity stability. We used this heating phenomenon to judge whether the dipole trap is in the vicinity of the cloud of cold atoms in the magnetic trap.

Figure 5.2 shows our first observation of dipole trapping of ultra-cold atoms. There

were 7000 atoms in the trap and the cloud density was 10^{13} cm^{-3} . The axial half-width ($1/e$) of the cloud was $100 \mu\text{m}$ and radial half-width was $20 \mu\text{m}$. One might notice that the size of this cloud is significantly larger than the size of the dipole trapping beam that we would expect (about a few μm). Given that the number of atoms loaded into the dipole trap was considerably large by dipole trap standards, illuminating it with our probing beam causes the atoms to absorb and re-emit while other atoms reabsorb and diffuse out in the process. This situation is similar to the density-limited regime in a Magneto-Optical Trap (MOT).

Once we were confident the focused beam was very close to the centre of the cloud, we no longer left the dipole trapping beam on during the experiment but waited until the end of the evaporation sequence after which the power of the beam focused on the atoms was ramped from 0 to 20 mW in 1 second. Immediately after this beam intensity ramp, the cloud of atoms was under the influence of a magnetic trap and a dipole trap simultaneously. So to separate the dipole trapped atoms from the magnetically trapped atoms, the magnetic trap was turned off and we waited for a further 18 ms of time to ensure that the cloud from the magnetic trap has fallen a significant distance. Afterwards, the cloud is imaged with absorption imaging while the atoms are still in the dipole trap.

The final step was to align the dipole beam to the centre of the cloud. This was done by reducing the final RF evaporation frequency gradually to get smaller clouds and seeing if atoms could still be loaded into the dipole trap. Once dipole trapping no longer occurred, the position of the focused dipole trapping beam was adjusted using mirror M1 (or M2) for movement in the x or y-direction and translating the objective in the z-direction for movement in the z-direction to observe dipole trapping again. This procedure was then repeated until we could still load atoms from a very small cloud. Then we were confident that our dipole trapping beam was focused at the centre of the magnetic trap.

5.1.2 Positioning the four-lens objective

After focussing the dipole trapping beam onto the centre of the magnetic trap, the next step was to optimise the positioning of the four-lens objective. Ideally, the cloud should be at the focal plane and along the optical axis of the four-lens objective. At the same time, the dipole trapping beam should also be entering the aperture of the objective along the axis of the objective.

The first step to this procedure was to roll out the vacuum cell again. We then inserted a USAF 1951 standard pattern R70 test image. The test image was glued on a stick which was glued on a mirror mount for fine and precise movement. The entire mirror mount was then fixed on a translation stage with the mount's movement parallel to the dipole trapping beam axis. The test image was illuminated from behind by the pyramidal MOT cooling beam and from the front by the dipole trapping beam. The test slide was manufactured from glass and mirror-coated on one side and could therefore act as a reflecting surface. In addition, the features on the test plate were transparent and would therefore transmit the pyramidal MOT light. The light transmitted through DM1 consisted of the reflected dipole trapping beam and the pyramidal MOT beam and it was focused onto the CCD camera using a lens of focal length 1 m. The test image could be translated in three dimensions to place the finest set of lines on the focused dipole beam. Temporarily, the location of the finest set of lines was the reference position of the magnetic trap.

The four-lens objective was mounted on a five-axis mount (X , Y , Z , pitch and yaw) and all five axes could be adjusted to ensure that the finest set of lines could be resolved. In fact, if we placed a white piece of paper between FM2 and FM3 and used an infra-red viewer to see the fluorescence light falling on the paper, we could also see the field-of-view of the four-lens objective. We then translated the objective to place the reference position of the magnetic trap at the centre of this field-of-view. Further adjustment of the five axes resolved the finest set of lines as shown in Figure 5.1.

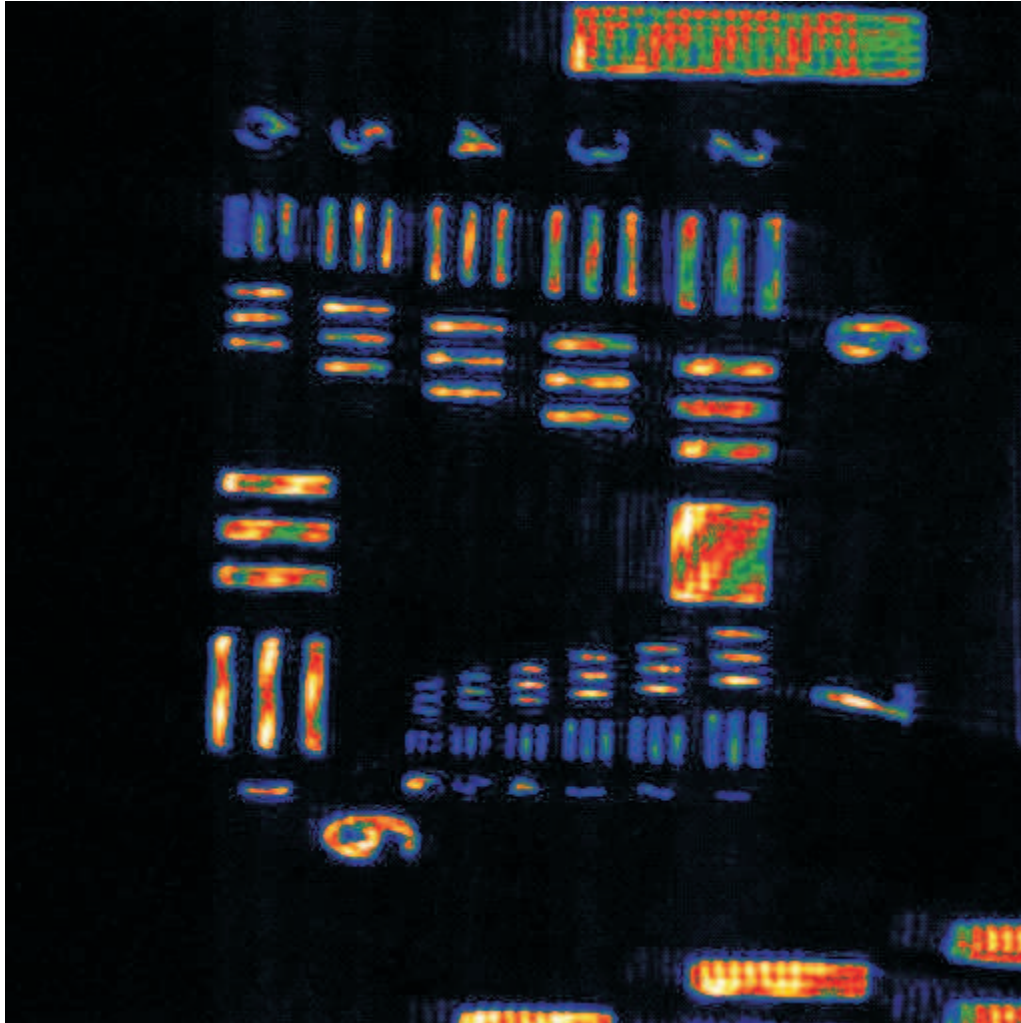


Figure 5.3: Our test image (USAF 1951 standard pattern R70) as seen via the fluorescence imaging path. What is visible here on the screen are elements 1-6 of group 6 and elements 1-6 of group 7. The finest set of lines would be element 6 of group 7 which are separated by a distance of $2.19 \mu\text{m}$.

5.1.3 Some estimates of fluorescence imaging parameters

Given the test image that we saw with our fluorescence imaging system, we can now estimate its magnification. The dimensions of the lines on the test image were fixed and they could be obtained from the datasheet that was provided with the product. The line lengths and widths were given as

$$Linewidth(mm) = \frac{2.5}{2^{Group+(Element-1)/6}} \quad (5.1)$$

$$Linewidth(mm) = \frac{1}{2^{Group+1+(Element-1)/6}} \quad (5.2)$$

From 5.2, the lines of the finest set were separated by a distance of $2.19 \mu\text{m}$. Being able to distinguish the lines meant that we could claim our fluorescence imaging system to have a resolution of $2 \mu\text{m}$ or better.

Using 5.1, we estimated the magnification of our imaging system by firstly counting the length of the features in numbers of pixels. From here we obtained the effective pixel size r_{eff} . We knew the real pixel size of our CCD camera $r_{pix}=16 \mu\text{m}$ and therefore we could calculate the magnification $M=r_{pix}/r_{eff}$. We estimated the effective pixel size for all elements in group 6 and calculated an average of $663 \pm 24 \text{ nm}$. This gave a magnification of 24.1 ± 0.8 .

5.1.4 Generation and manipulation of multiple spots

As mentioned in the previous section, the dipole trapping beam was focused on the test plate and was reflected back past the dichroic mirror DM1 and to the CCD camera. We varied the frequency input of the AOD and recorded the position of the focussed dipole beam spot as it was translated across the field-of-view. The graph of pixel position of the spot vs frequency input of the AOD as shown in Figure 5.4 has a slope of $22.5 \pm 0.1 \text{ pixels/MHz}$ and this corresponds to $14.9 \pm 0.5 \mu\text{m}/\text{MHz}$.

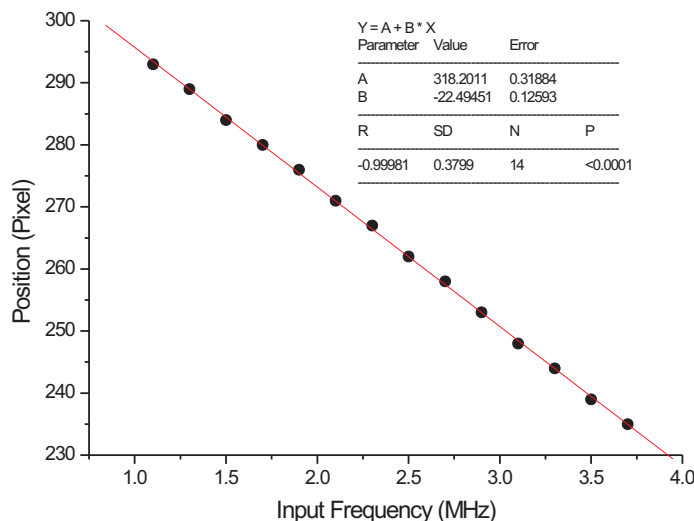


Figure 5.4: A calibration of spot position vs frequency input of the AOD.

With this calibration in hand, we gave a first demonstration of the capability to manipulate our dipole beam spots by varying the frequency input of the AOD. As we varied the frequency, we varied the spacing between the two spots as shown in Figure 5.5. We could distinguish the two spots when they are a minimum of $3 \mu\text{m}$ apart. One might notice that this resolution is different from the $1.74 \mu\text{m}$ resolution that the simulation of the four-lens objective yielded. Given that this simulation assumed the wavelength of light to be 780 nm , it should not be surprising for the resolution for 830 nm light as used in this experiment to be different.

5.2 Characterisation of the dipole traps

5.2.1 Beam waist measurement

Once we had established a method for trapping atoms in the dipole trap, we conducted several experiments to better understand the system. Firstly we measured the beam waist of our dipole trapping beam so we know the conditions that our atoms were going through.

We measure the beam waist by cutting across the beam with a razor blade and

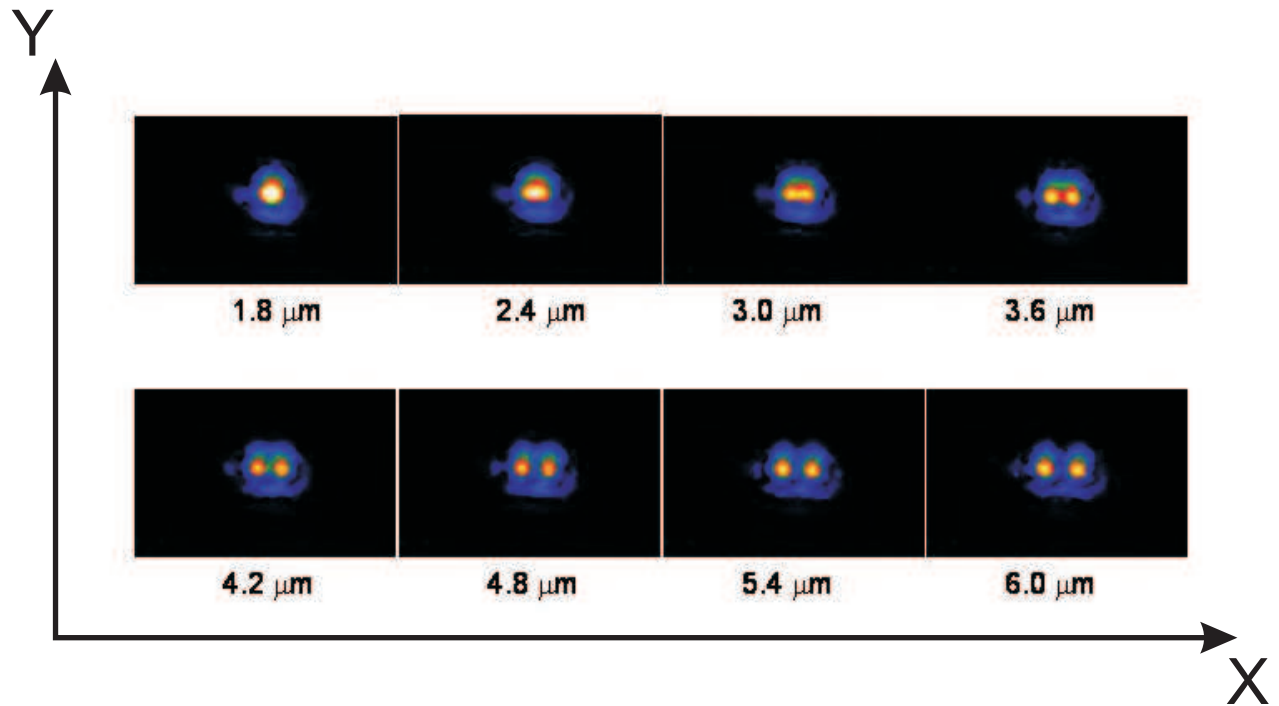
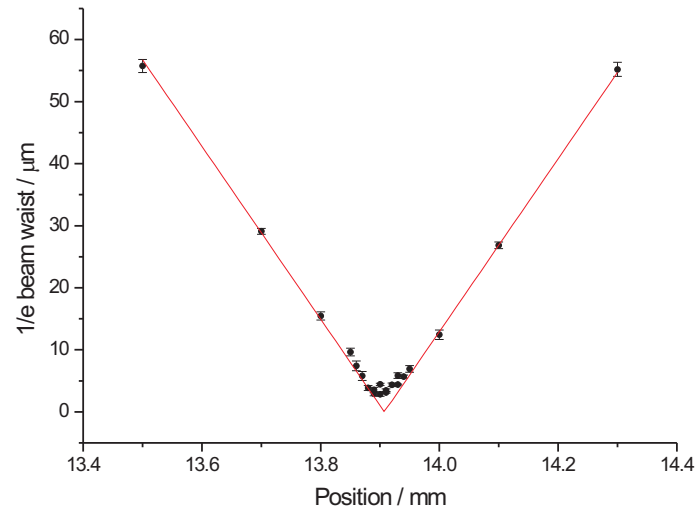
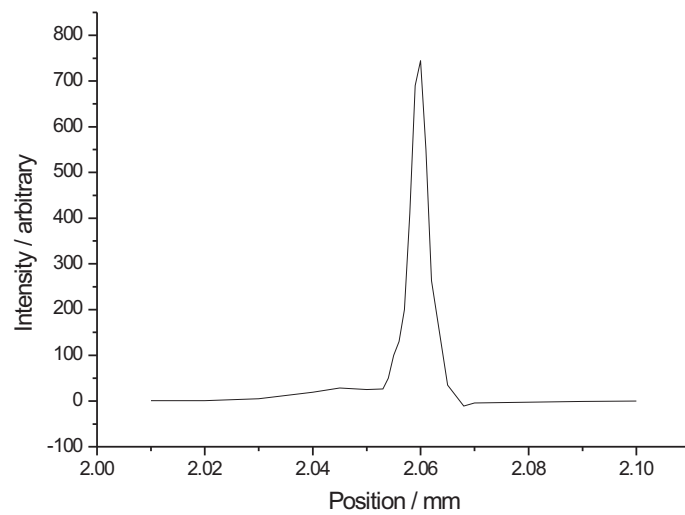


Figure 5.5: A first demonstration of spot manipulation as seen on the fluorescence imaging plane. Each image is accompanied by the separation between the two spots.



(A)



(B)

Figure 5.6: Beam waist measurements of our dipole trapping beam. (A) shows the beam waists attained w.r.t position of the blade. (B) shows a reconstruction of our dipole trapping beam.

measuring the beam power that passes the blade. The blade was mounted on a 3D translation stage with μm precision so that it can be translated across the beam and also along the optical axis. We measured the beam waists at different positions of the razor blade along the optical axis and the graph of waists is shown in Figure 5.6 (A). The lowest beam waist that we have measured was $2.85 \pm 0.35 \mu\text{m}$. As we attempted to measure smaller and smaller beam waists, pointing stability of the beam and the mechanical stability of the razor blade became more and more crucial and there were significant fluctuations in beam power in the process of measuring the beam radius. Nevertheless, we claimed a reasonable upper limit of our dipole trapping beam waist ($1/e$) to be $3 \mu\text{m}$. When we measured the beam power w.r.t the razor blade position, we have a power vs position graph and we could reconstruct the intensity profile of the dipole trapping beam by differentiating across various points in this graph. (B) in Figure 5.6 shows our reconstructed Gaussian beam.

From here we estimated some properties of our dipole trap. Given this beam waist and using equations 2.65 and 2.66, we calculated that for every 1 mW of beam power P that illuminated the atoms, we achieved a trap depth of $55 E_R$ in units of recoil energies ($E_R = k_B \times 361.96 \text{ nK}$). For the same amount of beam power, we have a radial trapping frequency of 3.2 kHz and an axial trapping frequency of about 150 Hz. The trapping frequencies scale with \sqrt{P} . Alternatively, each $18 \mu\text{W}$ of power gives a recoil energy worth of trap depth that we want to achieve. As for scattering rate, we estimate that for every recoil temperature worth of trap depth, our scattering rate is $\Gamma_{sc} = 2\pi \times 0.0121 \text{ s}^{-1} E_R^{-1}$ or approximately one scattering event every 80 seconds or so. Scattering rate scales proportionally with P .

5.2.2 Loss rate of atoms in the dipole trap

We then measured the loss rate of atoms in our dipole trap. After evaporative cooling of our atoms to a thermal cloud of temperature of about 320 nK, the beam intensity was ramped from zero intensity to the final trap depth in 500 ms. Then, the magnetic trap was turned off after which the remaining atoms in the dipole

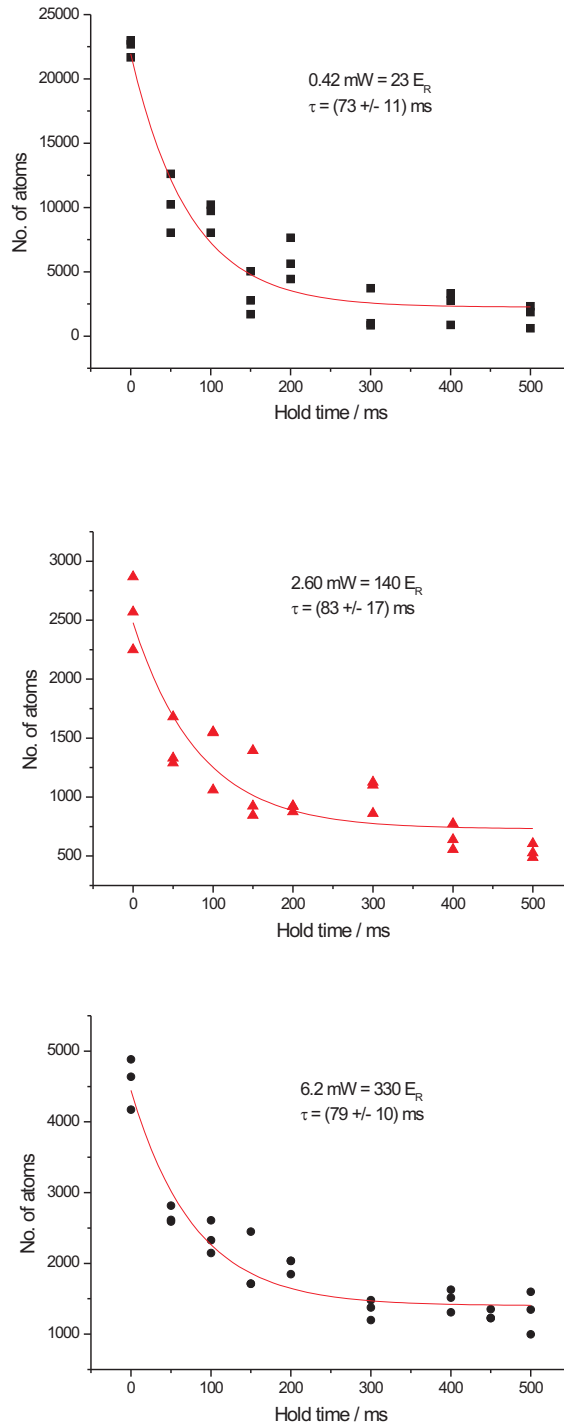


Figure 5.7: Measurement of the rate of loss of atoms in our dipole trap. Loss rates are shown as τ^{-1} .

trap were given a certain hold time before images were taken to measure how many atoms were left in the dipole trap. We varied the hold time for a certain trap depth to measure the loss rate and we measured this for three different trap depths. The graphs are shown in Figure 5.7.

Given that from results above the loss rate of the atoms in the dipole trap were independent of our trap depth, these seem to suggest that our loss rate does not correspond to the true lifetime of the atoms in our dipole trap. A possible reason is there are atoms with energies very close to the value required to escape the trap and this loss rate implies those atoms escaping first before stabilising to some other equilibrium value of atom number.

This loss rate could also be due to a combination of processes of background collisions, 2-body and 3-body inelastic collisions. Taking into account these loss mechanisms, the loss rate of atoms is given by

$$\frac{dN}{dt} = -\frac{N}{\tau_b} - K_2 \langle n \rangle N - K_3 \langle n^2 \rangle N \quad (5.3)$$

where τ_b is the loss rate for background collisions and K_2 and K_3 are loss rates for 2-body and 3-body inelastic collisions respectively. In addition, we must also consider losses from heating due to pointing and intensity stability of the dipole trapping beam. At this moment, our loss rate could be a mixture of the above processes and so does not reflect the true lifetime of our atoms in the dipole trap. Understanding this would require further investigation in the future.

5.2.3 Probing sequence

To resolve these narrowly separated dipole traps, we need to be able to observe the dipole trapped atoms via the fluorescence imaging system. Initially, to maximise observed signal, we changed the settings of our Andor iXon CCD camera to greatly increase its sensitivity. We increased the pre-amplifier gain to the maximum possible value of 5.1 and also increased the Electron Multiplying Charged-Couple Device

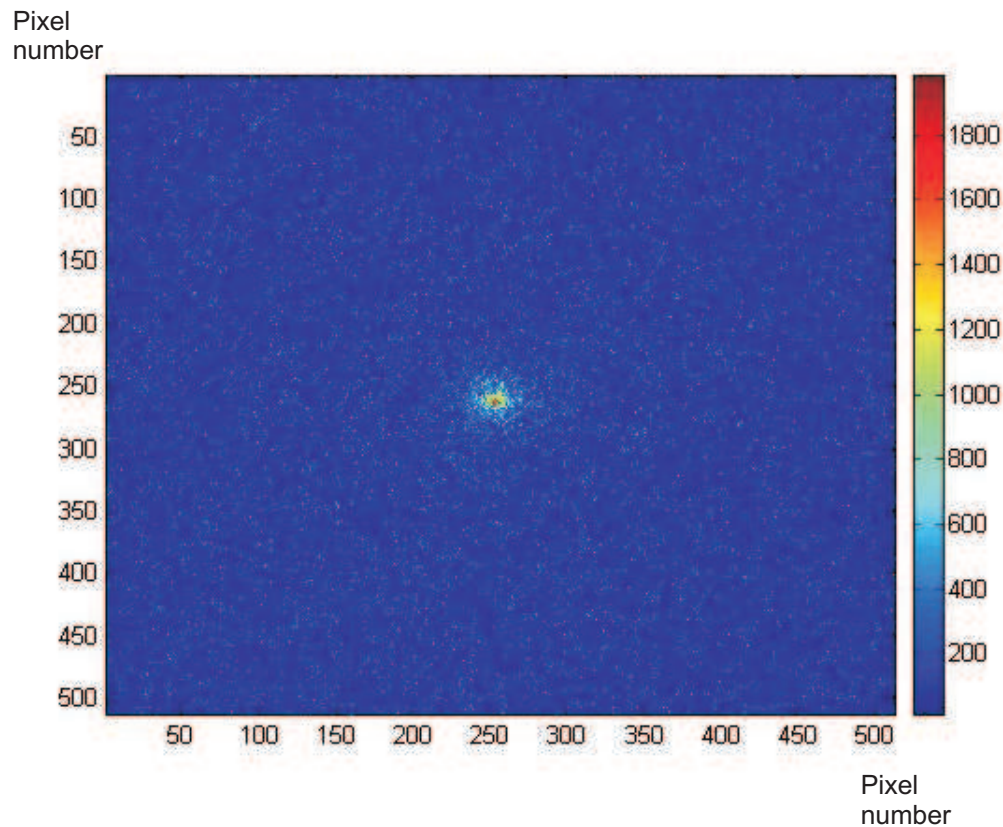


Figure 5.8: A typical fluorescence image of our atoms in the dipole trap. For this particular image, there were 3800 atoms in the dipole trap and the image registers a maximum signal of 2700 counts at the centre of the cloud.

(EMCCD) gain to the maximum value of 255. To make the atoms fluoresce, at the end of the sequence where we loaded atoms into the dipole trap, we illuminated the atoms with the MOT cooling beams for 10 ms.

After some signal was observed, the mirrors along the fluorescence imaging path can be adjusted to move the image to the centre of the CCD chip. Then we can establish a probing sequence such that we could obtain a healthy amount of signal from the atoms while the cloud of atoms roughly maintains its shape and was minimally heated by exposure to the cooling beams. We established that a good exposure time of the atoms to the MOT cooling beams was $200 \mu\text{s}$. The total MOT beam power was 26 mW and given our beam waist, this corresponded to an intensity of 10 mWcm^{-2} or almost $6 I_s$ in units of saturation intensities. The

laser detuning of our MOT beams was $\delta = -9$ MHz. Figure 5.8 shows a typical image of our atoms in the dipole trap. The typical cloud radial width ($1/e$) that we obtained was $20 \mu\text{m}$.

With this probing sequence, we calculated how the number of counts we obtained via fluorescence imaging would correspond to the true number of atoms by calibration against absorption imaging. Assuming that a cloud of atoms in our dipole trap could be attained reproducibly, there should be an equal number of atoms regardless of our imaging method.

For an arbitrary dipole trapping sequence, when we ran the experiment ten times using absorption imaging, we had $(4.11 \pm 0.60) \times 10^3$ atoms. We then switched immediately to fluorescence imaging; running the same experiment ten times, we registered $(1.27 \pm 0.11) \times 10^6$ counts on the CCD camera. Therefore, for a number of atoms N_{atoms} and number of counts N_{counts} that we have just measured, calibration was obtained by including an imaging factor α such that $N_{atoms} = \alpha N_{counts}$. This imaging factor was then included permanently in the image processing program to calculate our number of atoms in the dipole trap. Given that the signal-to-noise ratio is good only for low atom numbers for fluorescence imaging (see Appendix D), this calibration was only useful for measurement of low atom numbers. Now that we have the above expression, we measured $\alpha = (3.24 \pm 0.55) \times 10^{-3}$ or 300 counts/atom with a 17% error. Conveniently, this imaging factor took into consideration absolutely all factors such as pre-amplifier gain, EMCCD gain, solid angle presented by the four-lens objective, MOT beam intensity, exposure time and signal losses via all optical components.

5.2.4 Low atom number detection

With this calibration, we tried to detect as low an atom number as possible so as to gauge the capability of our imaging system. When an image is taken, it is essentially a 512×512 matrix where elements record the number of counts detected on each pixel. We conclude that the imaging system is capable of detecting a

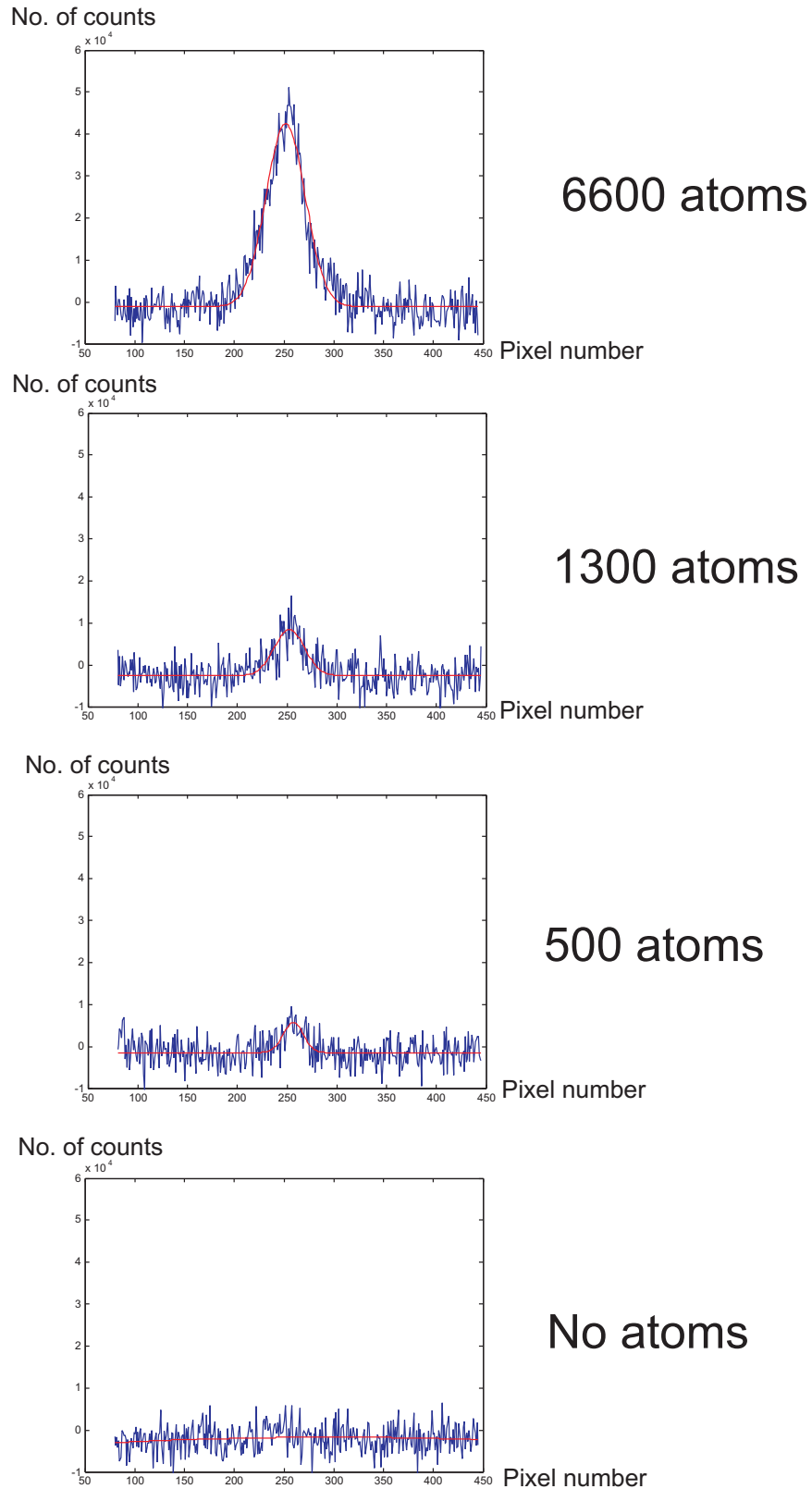


Figure 5.9: Low atom number detection by the fluorescence imaging system. All atom numbers shown have a 17 % error.

certain number of atoms by summing this matrix in one direction and if we see this profile of integrated counts by eye, one should clearly see the presence of signal emitted from the atoms. Graphs of integrated counts for different atom numbers are shown in Figure 5.9. These graphs were compared with a typical graph where no atoms were observed and it was clear that as it stood, our fluorescence imaging system was capable of detecting about 500 atoms at the lowest. In the near future, we hope to improve this system to be able to detect single atoms.

5.2.5 Generation and manipulation of multiple dipole traps

An integral part of this experiment was the ability to manipulate the dipole traps. Our Arbitrary Waveform Generator (AWG) provided a carrier frequency ν_0 of 50 MHz and this carrier signal was mixed with an additional signal $\delta\nu$ generated by a 20 MHz signal generator. As a result, we have two different signals of frequency $\nu_0 \pm \delta\nu$ and this results in the generation of multiple dipole trapping beams which focussed via the four-lens objective to form multiple dipole traps. By varying $\delta\nu$, we could vary the separation between the two spots. A demonstration of this is shown in Figure 5.10 where we loaded the atoms from a partially-evaporated thermal cloud into multiple dipole traps. With this demonstration, we have made significant significant progress towards achieving addressability of individual lattice sites.

This experiment could be expanded to try varying the array configuration of the multiple dipole traps. As shown in the setup in Figure 3.16, our AOD could deflect light in the X and the Y axes because the carrier frequency that we started with could also be mixed in both axes to generate multiple deflection of light in the X and Y axis. We have successfully loaded atoms into a single spot, 1×2 array, 1×3 array and 2×2 array of optical dipole traps. Loading of atoms into these traps was demonstrated and images are shown in Figure 5.11. This was again one very big step forward in achieving a 2-dimensional array optical lattice where the lattice sites were completely manipulable.

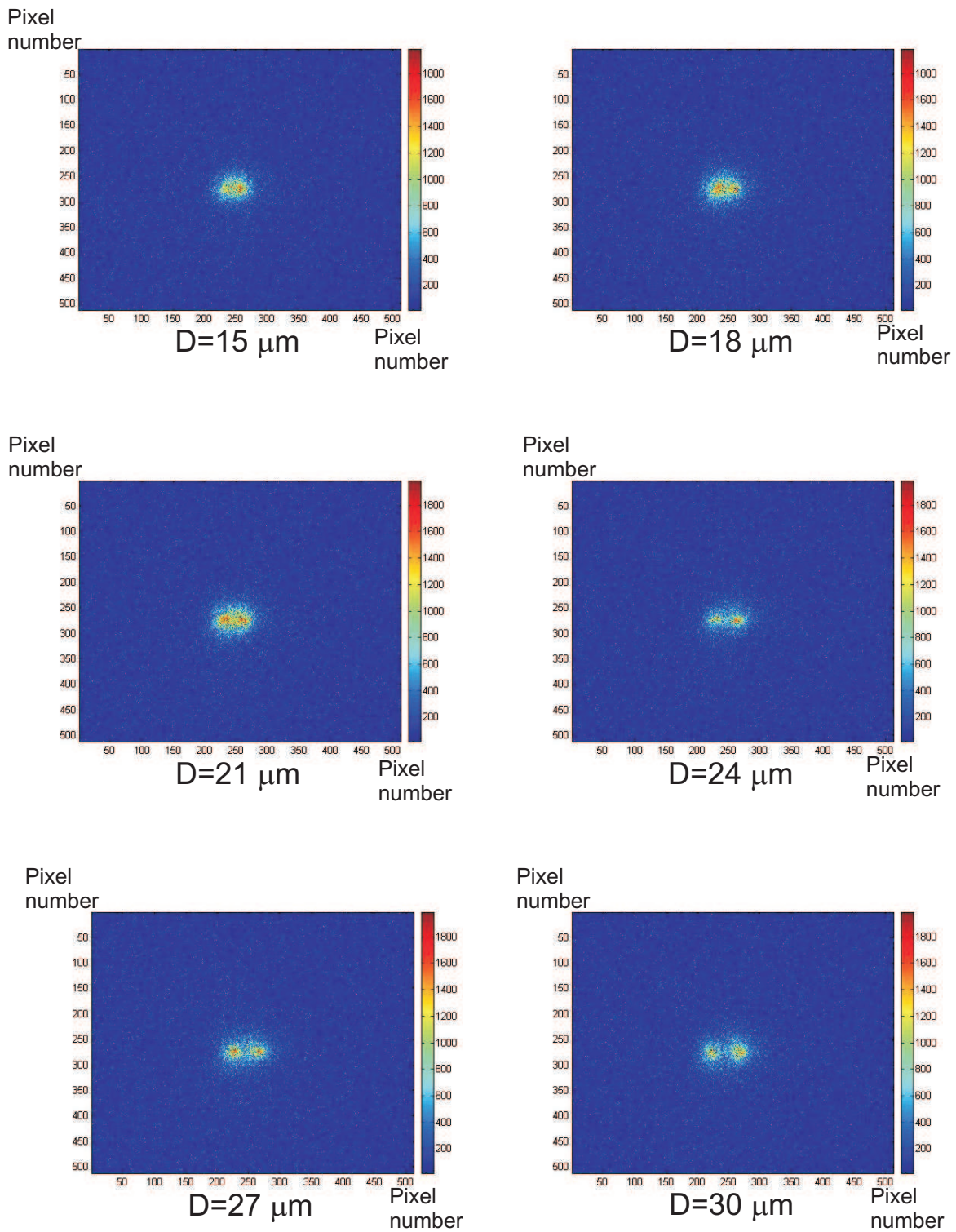


Figure 5.10: Varying the separation between two clouds of atoms in dipole traps. D is the value of the separation. There were approximately 6000 atoms in each lattice site.

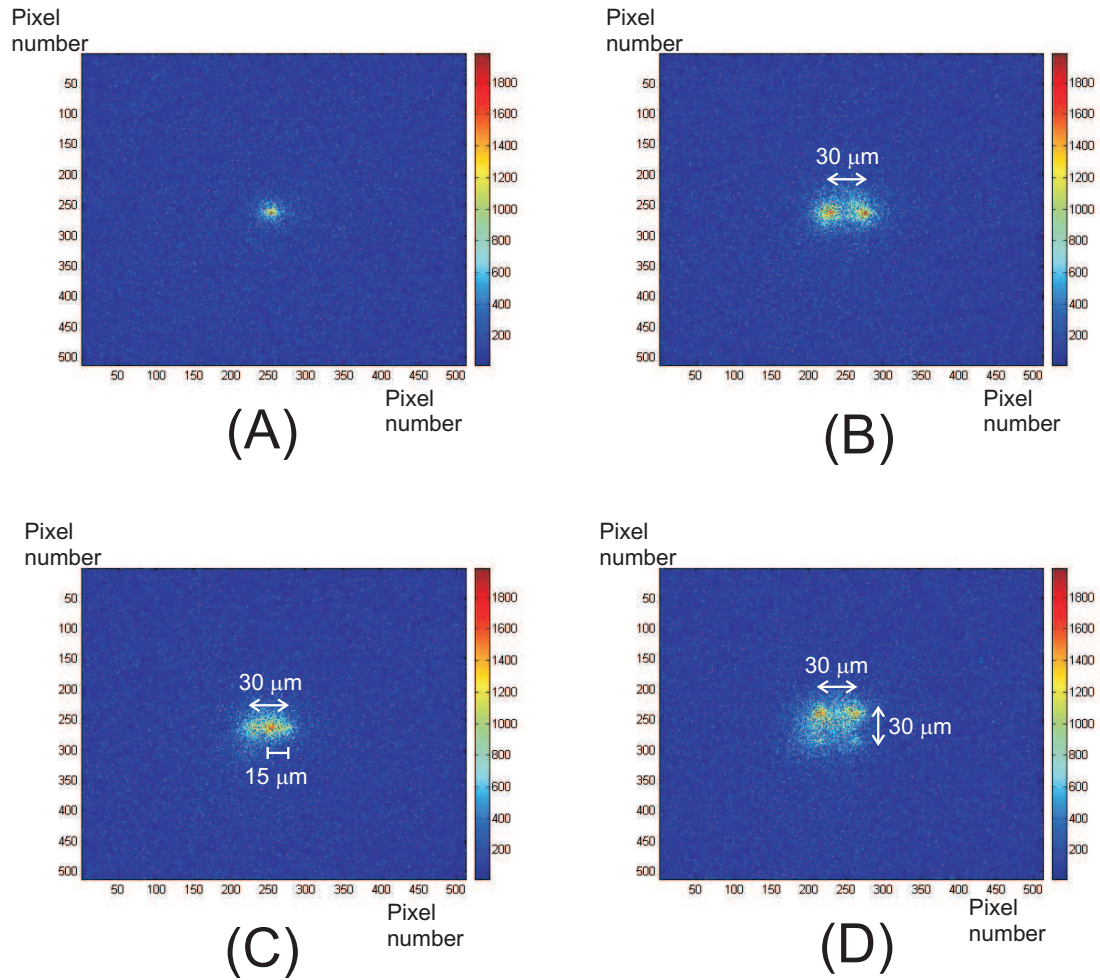


Figure 5.11: A first demonstration of achieving different configurations of dipole trapping. (A) Single spot. (B) 1×2 array of dipole traps. (C) 1×3 array of dipole traps. (D) 2×2 array of dipole traps.

Finally, we try to understand what the various limitations of this method of dipole trap splitting might be. Firstly, given that our AOD has a total bandwidth of 25 MHz and given our calibration, we estimate that a single trap can be moved by a total distance of more than $370 \mu\text{m}$ from one side to the other. Now that we also know our resolution of distinguishing multiple spots to be $3 \mu\text{m}$, this implies that we can have a maximum of 123 lattice sites per axis. With our current method of operation, we know too that lattice sites in our setup can only be moved in rows and/or columns. Moreover, our setup is only capable of generating a 2-dimensional optical lattice. While generating a 3-dimensional lattice is not impossible using our setup, at this moment there is enough interesting physics to study with just a 2-D lattice. As with all other traps, our dipole trap needs to fulfill certain stability requirements to avoid heating of the cloud or decoherence of the condensate. A formal treatment of these requirements with respect to pointing and intensity stabilities can be found in [68].

Nevertheless, this method of operation has its advantages over other methods. For example, this setup will have much more precise control of lattice sites compared to dipole traps created by holographic methods (eg. spatial light modulator). Our dipole trap manipulation is also not restricted like that in traps generated by microlens arrays. Our apparatus offers greater flexibility and addressability than optical lattices where the lattice separation is typically of the order of hundreds of nanometres and our trapping mechanism is not dependent on spin states like that in atom chips.

Conclusion and future work

6.1 Achievements so far

While there is still much to do, a lot has already been achieved since the experiment started its construction phase in October 2003. Our first milestone was the successful building of the experiment which produced BEC. As mentioned, we had about 10^5 atoms in our pure BEC which was much more than what we will ever need for our Mott Insulator (MI) experiments.

Our next two milestones were demonstrating that we could load cold atoms into the dipole trap and seeing those atoms by fluorescence imaging. This process has been reproducible so far and this is very important. With the magnification that we currently have, we hope to be able to observe processes such as trap splitting and displacement. Given our probing sequence, we have also detected low atom numbers although admittedly, our current probing sequence still has room for improvement.

Finally, we have demonstrated dipole trap manipulation and also successfully created a small 2×2 optical lattice. While we aim to be more ambitious with the optical lattice, this demonstration was a very big step forward and laid the foundation for the work ahead.

6.2 Future work

Before we begin qubit manipulation experiments, there are several things that need to be done.

6.2.1 Adiabatic loading of BEC

While we have successfully loaded cold atoms into the dipole trap, there is a need to determine whether this process is adiabatic. The best way to do this is to check that a condensate loaded into a dipole trap remains a condensate. This could be done by loading some atoms into a dipole trap after which the magnetic trap could be switched off to remove atoms still trapped in the magnetic trap. The dipole trap could then be split into two separate traps located close to each other and then be turned off abruptly. The two condensates will fall and expand. If the two clouds are still condensates after loading into the dipole trap, they will interfere when they overlap and interference patterns will be observed.

There are two things to consider in order to achieve this. One would be intensity stability and how the intensity is ramped. As for the former, we have set up a prototype intensity servo device into our experiment which helped keep our intensity stable reduce beam power fluctuations when the beam intensity is ramped from one value to another. As for the latter, the time taken and the functional form of the ramp can be varied to achieve adiabaticity.

When we have demonstrated that atoms have been adiabatically loaded into the trap, we can then ensure that the atoms are at the lowest energy state of the dipole trap. This corresponds to the atoms being in the harmonic region and then we can also measure the trapping frequencies of the dipole trap given the beam intensity. Knowing the trapping frequencies will allow us to more accurately calculate the temperature of our cloud and will give us more information regarding the true waist of our dipole trapping beam.

6.2.2 Imaging and single atom detection

Having the atoms in our dipole trap in a condensate form means our cloud of atoms is in the densest possible state and thus the ideal test object to check if our imaging system is focussed. We can then measure the magnification of the imaging system by measuring the apparent acceleration due to gravity of a falling cloud of atoms released from the dipole trap. This method was also used to measure the magnification of our absorption imaging system.

Having a focused imaging system results in the highest possible signal concentration and this greatly improves our capability of detecting very low atom numbers. While the experiment has shown to be able to detect about 500 atoms, ideally we would like to detect single atoms. Another thing that can be tried is changing the probing sequence to maximise signal and minimise noise at the same time.

6.2.3 2D optical lattice and the Mott Insulator state

In this experiment, we have demonstrated several possible configurations of 2D optical lattice. These are the single dipole trap, the 1×2 array, the 1×3 array and the 2×2 array. So far, we did this using a setup of a main signal generator to provide the carrier frequency, an additional signal generator and an RF mixer to provide the multiple frequency signal input into the AOD. The schematic of this setup is shown in Figure 3.16. We hope to improve the current setup by using a custom-built circuit board incorporating ten Direct Digital Synthesis (DDS) chips with a common 20 MHz clock to potentially provide ten sinusoidal signals with independent, dynamically variable frequencies. We wish for two of these boards to be made, one for the X axis and the other for the Y axis. This means that we will soon be capable of a 10×10 array of dipole traps, similar to a 2D optical lattice.

Once this board is set to work reproducibly, the next step is to use the board to successfully produce the multiple frequency inputs to the AOD to generate multiple dipole traps with atoms loaded into them. Not only that, it must be demonstrated that these traps can split adiabatically. Again, the best way to check this is to make

sure that the condensate that is loaded into these traps remain in condensate form. When the dipole traps are released and the expanded clouds overlap, interference patterns should be observed.

Finally, before we can claim to be ready for qubit manipulation and possibly other experiments, we need to reproduce the Mott Insulator state as it is vital for quantum information processing that the atom number is distributed evenly amongst the lattice sites. We hope to do this by repeating the method as mentioned in [8] where quantum tunneling between lattice sites is suppressed by increasing the potential barrier between the sites. This is done by increasing the dipole trapping beam intensity and therefore the trap depth of each lattice site. As tunneling rates are suppressed, the interference pattern we expect to see when the atoms are in the superfluid state will start to lose its definition. Alternatively, we can verify the MI state by direct atom number counting [61] and verifying that the fluctuation of the measured atom number is lower than the Standard Quantum Limit (SQL).

Rubidium-87 data

Relevant physical properties for Rb-87 atoms are given below. For the cases where these depend on the specific atomic transition, they are given for the D_2 line of Rb-87.

Quantity	Symbol	Value
Atomic number	Z	37
Nuclear spin	I	$3/2$
Mass	m	1.443×10^{-25} kg
Wavelength (vacuum)	λ	780.241 nm
Wave number (vacuum)	$k/2\pi$	12816.5 cm $^{-1}$
Natural linewidth (FWHM) Decay rate	Γ	$2\pi \cdot 6.065$ MHz 38.11×10^6 s $^{-1}$
Saturation intensity π -pol ($F = 2 \rightarrow F' = 3$) Resonant cross section π -pol	I_{sat} σ_0	2.503 mW cm $^{-2}$ 1.938×10^{-9} cm 2
Saturation intensity σ -pol ($ F = 2, m_F = \pm 2\rangle \rightarrow F' = 3, m_{F'} = \pm 3\rangle$) Resonant cross section σ -pol	I_{sat} σ_0	1.67 mW cm $^{-2}$ 2.907×10^{-9} cm 2
Recoil velocity	$v_r = \hbar k/m$	5.88 mm s $^{-1}$
Recoil temperature	$T_r = mv_r^2/k_B$	362 nK
Zeeman shift of $5S_{1/2}$ $F = 2$	$1/2 \mu_B \times m_F$	700 kHz G $^{-1} \times m_F$
Zeeman shift of $5P_{3/2}$ $F = 3$	$2/3 \mu_B \times m_F$	933 kHz G $^{-1} \times m_F$
Scattering length at $B = 0$ $ F = 1, m_F = 1\rangle$	a	5.31 nm

Beam waist measurement

The setup for measurement of a beam waist consists of a razor blade mounted on a translation stage. The blade is translated finely to cut into the beam. The beam power past the blade is then measured and the beam power vs position profile will provide us information regarding the size of the beam. This section derives the functional form used to fit to such a profile.

The first assumption is that the beam in question is of a Gaussian profile which stretches from $+\infty$ to $-\infty$, is centred at $x=0$ and has a $(1/e)$ width σ . With the razor blade partially into the beam at some position x_0 , the power measured past the blade would be the integral of the intensity profile from ∞ to x_0 :

$$\begin{aligned}
 P &= I_0 \int_{x_0}^{\infty} e^{-x^2/\sigma^2} dx \\
 &= I_0 \left\{ \int_{x_0}^0 e^{-x^2/\sigma^2} dx + \int_0^{\infty} e^{-x^2/\sigma^2} dx \right\} \quad (\text{B.1})
 \end{aligned}$$

The substitution $t^2 = x^2/\sigma^2$ and therefore $dx=\sigma dt$ can be used. The special integral $\int_{-\infty}^{\infty} e^{-t^2} dt = \sqrt{\pi}$ should also be substituted to transform equation B.1 to

$$P = I_0 \sigma \left\{ \int_{x_0/\sigma}^0 e^{-t^2} dt + \frac{\sqrt{\pi}}{2} \right\}$$

$$\begin{aligned} &= \frac{I_0\sigma\sqrt{\pi}}{2} \left\{ 1 - \frac{2}{\sqrt{\pi}} \int_0^{x_0/\sigma} e^{-t^2} dt \right\} \\ &= A \left\{ 1 - \text{erf}(x_0/\sigma) \right\} \end{aligned} \tag{B.2}$$

and this is the form of the fitting expression used to extract the beam waist ($1/e$).

Calculating atom number from a Magneto-Optical trap

The number of atoms in a MOT can be estimated using fluorescence measurements [40]. A summary of the expressions required are shown below. The power radiated by an atom in a MOT is given by

$$P_{at} = \frac{\hbar\omega_L\Gamma}{2} \frac{C_1^2 I/I_s}{1 + C_2^2 I/I_s + 4\delta^2/\Gamma^2} \quad (\text{C.1})$$

where C_1^2 and C_2^2 can be determined experimentally [40] and are of the order of unity, ω_L is the laser frequency, I and I_s are the beam intensity and saturation intensity of the atomic transition respectively, δ is the laser detuning and Γ being the spontaneous decay rate of the excited state. The power P of light incident on the photodiode is

$$P = NP_{at} \frac{\Omega}{4\pi} \quad (\text{C.2})$$

where N is the number of atoms and Ω is the solid angle subtended by the collection lens given as

$$\Omega = \frac{\pi d^2}{4x^2} \quad (\text{C.3})$$

where d is the diameter of the collection lens and x is the distance from the atoms to the collection lens. The light incident on the photodiode from the atoms gives rise to a photodiode signal S given by

$$S(V) = PR(\lambda)R_{load} \quad (\text{C.4})$$

where $R(\lambda)$ is the responsivity of the photodiode and R_{load} is the load resistance. If we use C.4 and C.3, our number of atoms N is then given as

$$N = \frac{S(V)}{R(\lambda)R_{load}} \frac{16x^2}{d^2} \frac{1}{P_{at}} \quad (\text{C.5})$$

Signal to noise ratio between absorption and fluorescence imaging

The following derivation is a comparison of fluorescence and absorption imaging signals as a function of atom number. Figure D.1 shows a scheme of the setup referred to to calculate the difference between signal-to-noise ratios between the two imaging methods.

Absorption imaging is discussed first. Consider the photons arriving at a single CCD pixel which has an effective area A' where $A' = A/M$ given that A is the true pixel size and M is the magnification factor of the imaging system. Now if we have a small number of atoms N localised within a section of area A' of the probing light with intensity I , the reference signal (in counts) obtained (just the probing light without illuminating the atoms) is given as $S_1 = \eta I A'$ where $\eta = Q/\hbar\omega$ and Q is the quantum efficiency of the detector. The absorption signal is then given as $S_2 = \eta I A' e^{-n\sigma l} = \eta I A' e^{-N\sigma/A'}$ where σ is the scattering cross-section of the atom. From here, we obtain our useful signal to be $S_1 - S_2 = S_1(1 - e^{-N\sigma/A'})$. The noise on absorption is just $\sqrt{S_1}$ and therefore our signal to noise ratio for absorption imaging is $\sqrt{S_1}(1 - e^{-N\sigma/A'})$.

For fluorescence imaging, the fluorescence emitted by the atoms is simply related to the amount of light that was absorbed by the atoms during absorption imaging

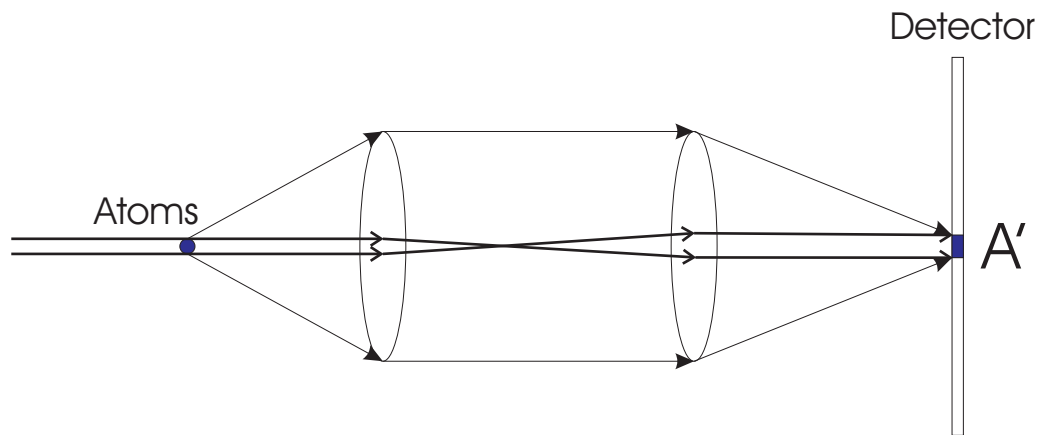


Figure D.1: Scheme of absorption and fluorescence imaging for the study of signal-to-noise ratio.

i.e. $S_F = f(S_1 - S_2)$ where f is the fraction of fluorescence light collected by the collection optics. The noise of this signal is $\sqrt{S_F}$. Therefore, the signal to noise ratio for fluorescence imaging is $\sqrt{f(S_1 - S_2)}$. We have assumed that the magnification and quantum efficiency of the detector is the same in our example for both imaging methods.

With the above expressions, the ratio of signal to noise ratio between fluorescence imaging and absorption imaging is $\frac{(S/N)_F}{(S/N)_{abs}} = \sqrt{\frac{f}{1 - e^{-N\sigma/A}}}$. If this ratio is calculated with typical experimental parameters where $N\sigma/A \ll 1$, then it can be approximated as $\sqrt{\frac{fA}{N\sigma}}$. In reality, when imaging a small number of atoms, fluorescence imaging is always the more suitable imaging method.

This is because of the role of other sources of imperfections in the absorption imaging signal other than shot noise. For example, imperfections in the CCD and optics may cause the laser beam (with no atoms present) to record a slightly different intensity on each pixel. There will also be fringing effects due to the interference of back reflections off optical components. These imperfections make the absorption background IQ uncertain by a small fraction (a few percent). If only a small number of atoms are imaged by each pixel, the absorption signal will be relatively small (also around a few percent) and this uncertainty in the background will overwhelm the absorption signal. However, for fluorescent imaging

these imperfections will show up only as a small percentage of the total fluorescent signal, and so will have far less negative influence on the measurement.

Control

We use two computers to run our experiment; one computer controls all of the timing, digital, analog, and GPIB commands (control computer) while the other is dedicated to running the camera (camera computer). To initiate an image acquisition, the control computer externally triggers the camera and with the computer software running, the software takes the images and stores the data in the hard disk. The control computer subsequently communicates with the camera computer via serial cable to call the files containing the final image which is then analysed by a MATLAB program specifically written to calculate various cloud parameters including temperature and density. Allocating control and acquisition tasks to different computers means that the camera computer can analyze the data from the previous shot while the control computer moves on to the experimental sequence for the next shot.

A Bose-Einstein condensation experiment requires precise control of a variety of components. Most functions require timing resolution on the millisecond scale, but for certain key tasks like imaging, we need timing with microsecond precision. There are several basic types of outputs and inputs our control system needs to handle, namely digital input/output, analog input/output, serial, and GPIB outputs. For a schematic of how all these components come together, refer to Figure E.1. The digital/analog input/output channels are all provided by three National

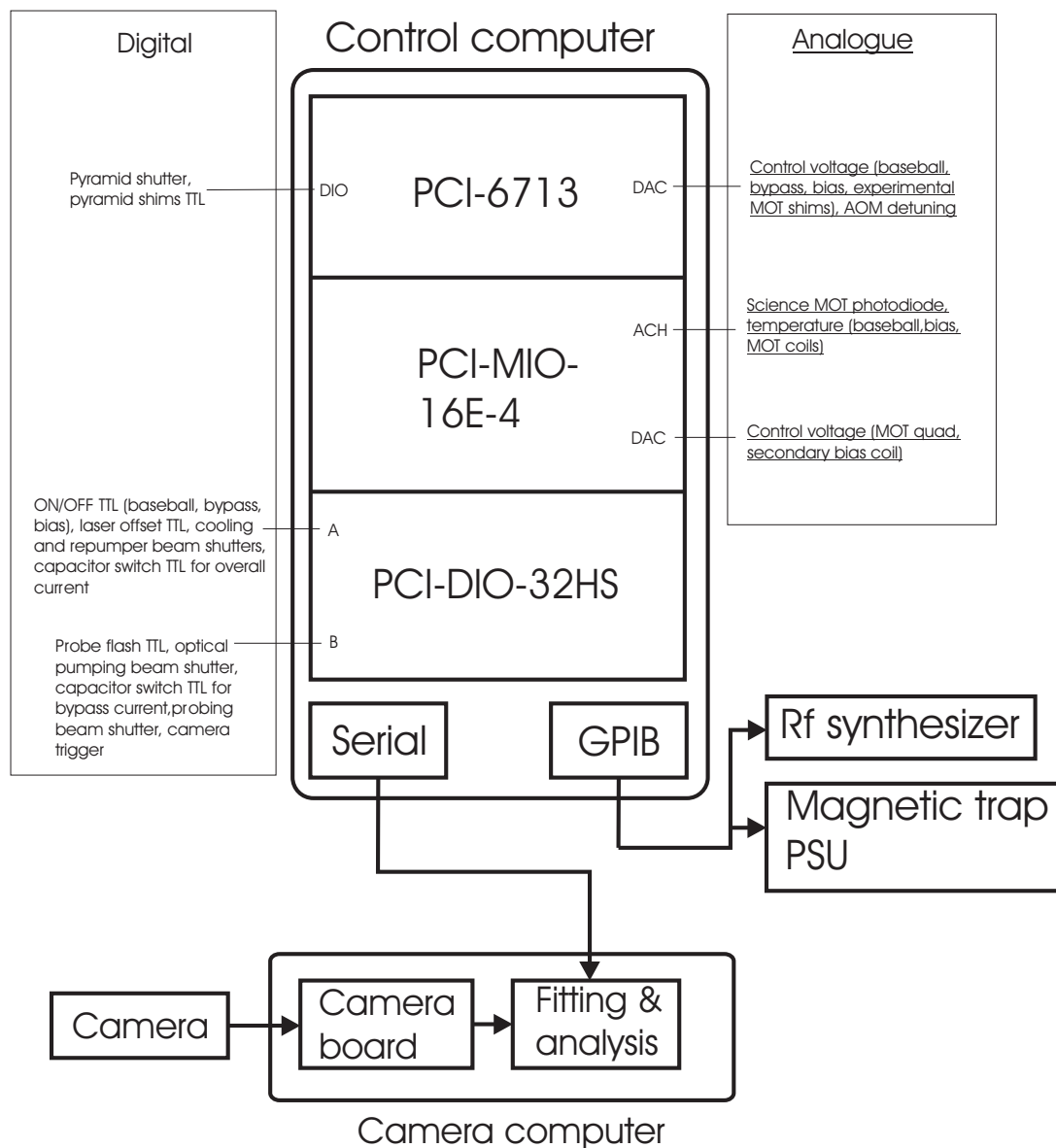


Figure E.1: Computer control diagram showing the different computer boards and what they control. DIO=digital input/output, DAC=analogue outputs, ACH=analogue inputs. For PCI-DIO-32HS, Port A and Port B have 8 digital input/output channels each.

Channel	Ground	PCI-6713	PCI-MIO-16E-4
ACH (ac)	AIGRD		channel 12: 2nd MOT photodiode channel 13: MOT Temperature channel 14: Baseball Coil Temperature channel 15: Bias Coil Temperature
DIO (di)	DGRD	channel 0: channel 1: channel 2: Shutter 5: Pyramid channel 3: Pyramid shims TTL channel 4: channel 5: channel 6: channel 7:	channel 0: channel 1: channel 2: channel 3: channel 4: channel 5: channel 6: channel 7:
PFI (pf)	DGRD	channel 0...	channel 0...
GPCTR_OUTPUT (gp)	DGRD	GPCTR 0: GPCTR 1:	GPCTR 0: GPCTR 1:
DAC OUT (da)	AOGRD	channel 0: Control voltage, overall current control channel 1: Control voltage, primary bias MOSFETs channel 2: Control voltage, bypass current channel 3: Auxiliary Voltage channel 4: AOM 1 Detuning channel 5: Science Shims N/S channel 6: Science Shims E/W channel 7: Science Shims U/D	channel 0: MOT Quad Current channel 1: Secondary bias coil control voltage
Total		32	44

PCI-DIO-32HS

Port A	Port B
channel 0: Bias/bypass on/off channel 1: CMOT offset TTL 2 channel 2: CMOT offset TTL 1 channel 3: AOM 3 TTL channel 4: Cap. Switch: overall current channel 5: Magnetic trap on/off channel 6: Shutter 3: Science MOT repumper channel 7: Shutter 1: Science MOT cooling	channel 0: AOM 1 TTL channel 1: Shutter 2: Probe/OP on/off channel 2: CMOT lock box gate channel 3: Bypass fast input channel 4: Shutter 4 Probe beam On/Off channel 5: Cap.switch: bypass current channel 6: channel 7: Camera trigger

Figure E.2: A complete allocation of the channels available on our computer NI boards.

Instruments boards (PCI-6713, PCI-MIO-16E-4 and PCI-DIO-32HS). Figure E.2 shows all the channels available on the three cards and what they are used for (not all channels are used). Most of the experiment is controlled by digital outputs, which control items such as shutters, rf switches, AOMs and the magnetic trap itself. Our coils (MOT, magnetic trap, shims) require analogue voltage set points. We also have several instruments including rf and magnetic trap power supply that use GPIB as the main mode of communication. Our input ports are used to monitor the fluorescence level from our MOT and to monitor temperature of our coils via K-type thermocouples.

Bibliography

- [1] M.H. Anderson, J.R. Ensher, M.R. Matthews, C.E. Wieman and E.A. Cornell, *Observation of Bose-Einstein Condensation in a Dilute Atomic Vapor*, Science, **269**, 198 (1995).
- [2] L. Pitaevskii and S. Stringari, *Bose-Einstein Condensation*, Oxford University Press, 2003.
- [3] J. I. Cirac and P. Zoller, *Quantum Computations with Cold Trapped Ions*, Phys. Rev. Lett., **74**, 4091 (1995).
- [4] C. Monroe, D. M. Meekhof, B. E. King, W. M. Itano and D. J. Wineland, *Demonstration of a Fundamental Quantum Logic Gate*, Phys. Rev. Lett., **75**, 4714 (1995).
- [5] D. Leibfried, B. DeMarco, V. Meyer, D. Lucas, M. Barrett, J. Britton, W. M. Itano and B. Jelenkovi, *Perturbing a persistent current with an external potential*, Nature, **422**, 412 (2003).
- [6] D. Jaksch, C. Bruder, J.I. Cirac, C.W. Gardiner and P. Zoller, *Cold Bosonic Atoms in Optical Lattices*, Phys. Rev. Lett., **81**, 3108 (1998).
- [7] D. Jaksch, H. J. Briegel, J.I. Cirac, C.W. Gardiner and P. Zoller, *Entanglement of Atoms via Cold Controlled Collisions*, Phys. Rev.Lett., **82**, 1975 (1999).
- [8] M. Greiner, O. Mandel, T. Esslinger, T. W. Hänsch and Immanuel Bloch, *Quantum phase transition from a superfluid to a Mott insulator in a gas of ultracold atoms*, Nature, **415**, 39 (2002).

-
- [9] I. L. Chuang, L. M. K. Vandersypen, X. Zhou, D. W. Leung and Seth Lloyd, *Experimental realization of a quantum algorithm*, Nature, **393**, 143 (1998).
- [10] T. Yamamoto, Yu. A. Pashkin, O. Astafiev, Y. Nakamura and J. S. Tsai, *Demonstration of conditional gate operation using superconducting charge qubits*, Nature, **425**, 941 (2003).
- [11] S. Kuhr, W. Alt, D. Schrader, M. Mller, V. Gomer and D. Meschede, *Deterministic delivery of a single atom*, Science, **293**, 278 (2001).
- [12] J. J. Garcia-Ripoll, P. Zoller and J. I. Cirac, *Quantum information processing with cold atoms and trapped ions*, J. Phys. B, **38**, 567 (2005).
- [13] G. K. Brennen, C. M. Caves, P. S. Jessen, I. H. Deutsch, *Quantum Logic Gates in Optical Lattices*, Phys. Rev. Lett, **82**, 1060 (1998).
- [14] J. Mompart, K. Eckert, W. Ertmer, G. Birkl and M. Lewenstein, *Quantum Computing with Spatially Delocalized Qubits*, Phys. Rev. Lett., **90**, 147901 (2003).
- [15] H. Metcalf., *Laser Cooling and Trapping*, Springer-Verlag New York Inc., 1999.
- [16] E. Arimondo, M. Inguscio, and P. Violino, *Experimental determinations of the hyperfine structure in the alkali atoms*, Review of Modern Physics, **49**, 31 (1977).
- [17] V. Bagnato, D. E. Pritchard, and D. Kleppner., *Bose-Einstein condensation in an external potential.*, Phys. Rev. A, **35**, 4354 (1987).
- [18] K. Huang., *Statistical Mechanics*, Jhon Wiley, 1963.
- [19] O.J. Luiten, M.W. Reynolds and J. T. M. Walraven, *Kinetic theory of the evaporative cooling of a trapped gas*, Phys. Rev. A, **53**, 381 (1996).
- [20] P. W. H. Pinkse, A. Mosk, M. Weidemüller, M.W. Reynolds, T.W. Hijmans and J. T. M. Walraven, *Adiabatically Changing the Phase-Space Density of a Trapped Bose Gas*, Phys. Rev. Lett., **78**, 990 (1997).

-
- [21] P. W. H. Pinkse, A. Mosk, M. Weidemüller, M.W. Reynolds, T.W. Hijmans and J. T. M. Walraven, *One-dimensional evaporative cooling of magnetically trapped atomic hydrogen*, Phys. Rev. A, **57**, 4747 (1998).
- [22] J.L. Roberts, N.R. Claussen, Burke, Jr., James P., Chris H. Greene, E.A. Cornell and C.E. Wieman, *Resonant Magnetic Field Control of Elastic Scattering of Cold ^{85}Rb* , Phys. Rev. Lett., **81**, 5109 (1998).
- [23] H. M. J. M Boesten, C.C. Tsai, J.R. Gardner, D.J. Heinzen and B.J. Verhaar, *Observation of a shape resonance in the collision of two cold ^{87}Rb atoms*, Phys. Rev. A, **55**, 636 (1997).
- [24] Burke, Jr., James P., John L. Bohn, B.D. Esry and Chris H. Greene, *Prospects for Mixed-Isotope Bose-Einstein Condensates in Rubidium*, Phys. Rev. Lett., **80**, 2097 (1998).
- [25] N. Bogolubov, *On the theory of superfluidity*, J. Phys., **11**, 23 (1947).
- [26] W. Ketterle, D.S. Durfee and D.M. Stamper-Kurn. Making, probing and understanding Bose-Einstein condensates. In S. Stringari M. Inguscio and C.E. Wieman, editors, *Proceedings of the International School of Physics - Enrico Fermi*, page 67. IOS Press, 1999.
- [27] T. W. Hansch and A. L. Schawlow, *Cooling of gases by laser radiation*, Opt. Commun, **13**, 68 (1975).
- [28] Steven Chu, L. Hollberg, J.E. Bjorkholm, Alex Cable and A. Ashkin, *Three-Dimensional Viscous Confinement and Cooling of Atoms by Resonance Radiation Pressure*, Phys. Rev. Lett., **55**, 48 (1985).
- [29] J. Prodan and W. Phillips, *Chirping the light fantastic - recent NBS atom cooling experiments*, Prog. Quant. Elect., **8**, 231 (1984).
- [30] W. Ertmer, R. Blatt, J. L. Hall, and M. Zhu, *Laser manipulation of atomic beam velocities: Demonstration of stopped atoms and velocity reversal*, Phys. Rev. Lett., **54**, 996 (1985).

-
- [31] R. Watts and C. Wieman, *Manipulating atomic velocities using diode lasers*, Opt. Lett., **11**, 291 (1986).
- [32] V. S. Bagnato, G. P. Lafyatis, A. G. Martin, E. L. Raab, R. N. Ahmad-Bitar, and D. E. Pritchard, *Continuous stopping and trapping of neutral atoms*, Phys. Rev. Lett., **58**, 2194 (1987).
- [33] W. Phillips and H. Metcalf, *Laser deceleration of an atomic beam*, Phys. Rev. Lett., **48**, 596 (1982).
- [34] P. Lett, W. Phillips, S. Rolston, C. Tanner, R. Watts, and C. Westbrook, *Optical molasses*, J. Opt. Soc. Am. B, **6**, 2084 (1989).
- [35] J. Dalibard and C. Cohen-Tannoudji, *Laser cooling below the Doppler limit by polarization gradients: simple theoretical-models*, J. Opt. Soc. Am. B, **6**, 2023 (1989).
- [36] A. Aspect, E. Arimondo, R. Kaiser, N. Vansteenkiste, and C. Cohen-Tannoudji, *Laser Cooling below the One-Photon Recoil Energy by Velocity-Selective Coherent Population Trapping*, Phys. Rev. Lett, **61**, 826 (1988).
- [37] Nir Davidson, Heun Jin Lee, Mark Kasevich, and Steven Chu, *Raman cooling of atoms in two and three dimensions*, Phys. Rev. Lett., **72**, 3158 (1994).
- [38] E.L. Raab, M. Prentiss, Alex Cable, Steven Chu and D.E. Pritchard, *Trapping of Neutral Sodium Atoms with Radiation Pressure*, Phys. Rev. Lett., **59**, 2631 (1987).
- [39] K. Lindquist, M. Stephens and C. Wieman, *Experimental and theoretical study of the vapor-cell Zeeman optical trap*, Phys. Rev. A, **46**, 4082 (1992).
- [40] C.G. Townsend, N.H. Edwards, C.J. Cooper, K.P. Zetie, C.J. Foot, A.M. Steane, P. Szriftgiser, H. Perrin and J. Dalibard, *Phase-space density in the magneto-optical trap*, Phys. Rev. A, **52**, 1423 (1995).

-
- [41] C.G. Townsend, N.H. Edwards, K.P. Zetie, C.J. Cooper, J. Rink and C.J. Foot, *High-density trapping of cesium atoms in a dark magneto-optical trap*, Phys. Rev. A, **53**, 1702 (1996).
- [42] C. Monroe, W. Swann, H. Robinson and C. Wieman, *Very Cold Trapped Atoms in a Vapor Cell*, Phys. Rev. Lett., **65**, 1571 (1990).
- [43] F. Shimizu, K. Shimizu, and H. Takuma, *Four-beam laser trap of neutral atoms*, Opt. Lett., **16**, 339 (1991).
- [44] K. Lee, J. Kim, H. Noh, and W. Jhe, *Single-beam atom trap in a pyramidal and conical hollow mirror*, Opt. Lett., **21**, 1177 (1996).
- [45] J. Reichel, W. Hansel, and T. Hansch, *Atomic micromanipulation with magnetic surface traps*, Phys. Rev. Lett., **83**, 3398 (1999).
- [46] J. Arlt, O. Marago, S. Webster, S. Hopkins, and C. Foot, *A pyramidal magneto-optical trap as a source of slow atoms*, Opt. Comm., **157**, 303 (1998).
- [47] Alan L. Migdall, John V. Prodan, William D. Phillips, Thomas H. Bergeman and Harold J. Metcalf, *First Observation of Magnetically Trapped Neutral Atoms*, Phys. Rev. Lett., **54**, 2596 (1985).
- [48] V.S. Bagnato, G.P. Lafyatis, A.G. Martin, E.L. Raab, R.N. Ahmad-Bitar and D.E. Pritchard, *Continuous Stopping and Trapping of Neutral Atoms*, Phys. Rev. Lett., **58**, 2194 (1987).
- [49] H. F. Hess, G. P. Kochanski, J. M. Doyle, N. Masuhara, D. Kleppner and Thomas J. Greytak, *Magnetic Trapping of Spin Polarized Atomic Hydrogen*, Phys. Rev. Lett., **59**, 672 (1987).
- [50] R. van Roijen, J.J. Berkhout, S. Jaakkola, and J.T.M. Walraven, *Experiments with Atomic Hydrogen in a Magnetic Trapping Field*, Phys. Rev. Lett, **61**, 931 (1988).

-
- [51] W. Ketterle and D.E. Pritchard, *Trapping and focusing ground state atoms with static fields*, Appl. Phys. B, **54**, 403 (1992).
- [52] E. Majorana, Nuovo Cimento, **9**, 43 (1932).
- [53] G. Breit and I. I. Rabi, *Measurement of nuclear spin*, Phys. Rev, **38**, 2832 (1931).
- [54] Norman F. Ramsey, *Molecular Beams*, Clarendon Press, 1956.
- [55] W. Ketterle and N.J. van Druten, *Evaporative Cooling of Trapped Atoms*, Adv. At. Mol. Opt. Phys., **37**, 181 (1996).
- [56] Walraven. In E. Riis G. L. Oppo, S. M. Barnett and M. Wilkinson, editors, *Quantum Dynamics of Simple Systems*, Vol. 44. IOP Bristol, 1996.
- [57] G. Rudolf, W. Matthias and Ovchinnikov Yurii B., *Optical dipole traps for neutral atoms*, Advances in Atomic, Molecular and Optical Physics, **42**, (2000).
- [58] L. Allen, *Optical resonance and two-level atoms*, Wiley, New York, 1975.
- [59] D.M. Stamper-Kurn, M.R. Andrews, A.P. Chikkatur, S. Inouye, H.-J. Miesner, J. Stenger and W. Ketterle, *Optical Confinement of a Bose-Einstein Condensate*, Phys. Rev. Lett., **80**, 2030 (1998).
- [60] M. P. A. Fisher, P. B. Weichman, G. Grinstein and D. S. Fisher, *Boson localization and the superfluid-insulator transition*, , **40**, 546 (1989).
- [61] C. S. Chuu, F. Shreck, T. P. Meyrath, J. L. Hansen, G. N. Price and M. G. Raizen, *Direct observation of sub-Poissonian number statistics in a degenerate Bose gas*, Phys. Rev. Lett, **95**, 260403 (2005).
- [62] K. Lee, J. Kim, H. Noh, and W. Jhe, *Single-beam atom trap in a pyramidal and conical hollow mirror*, Opt. Lett., **21**, 1177 (1996).

-
- [63] J. Arlt, P. Bance, S. Hopkins, J. Martin, S. Webster, A. Wilson, K. Zetie and C.J. Foot, *Suppression of collisional loss from a magnetic trap*, J. Phys. B, **31**, L321 (1998).
- [64] Peter Baranowski, *Towards number correlated states of a Bose-Einstein condensed gas*, Undergraduate project report, 2005.
- [65] W. Alt, *An objective lens for efficient fluorescence detection of single atoms*, Optik., **113**, 142 (2002).
- [66] W. Alt, D. Schrader, S. Kuhr, M. Muller, V. Gomer and D. Meschede, *Single atoms in a standing-wave dipole trap*, Phys.Rev.A, **67**, 1033403 (2003).
- [67] David E. Pritchard, Proceedings of the 11th International Conference on Atomic Physics, 619, (1989).
- [68] M. E. Gehm, K. M. OHara, T. A. Savard, and J. E. Thomas, *Dynamics of noise-induced heating in atom traps*, , **58**, 3914 (1998).